Elastic Stiffness Characterization of Anisotropic Materials by Line-focus Ultrasound Transducer

by

Qiuyan Li

B.S., North China University of Water Resources and Electric Power, 2011

M.S., University of Pittsburgh, 2015

Submitted to the Graduate Faculty of

Swanson School of Engineering in partial fulfillment

of the requirements for the degree of

Doctor of Philosophy

University of Pittsburgh

2019

UNIVERSITY OF PITTSBURGH

SWANSON SCHOOL OF ENGINEERING

This dissertation was presented

by

Qiuyan Li

It was defended on

July 19, 2019

and approved by

Minking Chyu, Ph.D., Professor
Department of Mechanical Engineering and Materials Science

William S. Slaughter, Ph.D., Associate Professor
Department of Mechanical Engineering and Materials Science

Kevin P. Chen, Ph.D., Professor
Department of Electrical and Computer Engineering

Dissertation Director: Qing-Ming Wang, PhD, Professor
Department of Mechanical Engineering and Materials Science

Elastic Stiffness Characterization of Anisotropic Materials by Line-focus Ultrasound Transducer

Qiuyan Li, PhD

University of Pittsburgh, 2019

Elastic stiffness constants are critical parameters to evaluate mechanical property of solid materials, and it is of great importance to develop convenient and accurate methods that can characterize material stiffness constants in industrial applications. Line-focus ultrasound transducer has been used as one of the methods to generate surface wave in isotropic and anisotropic materials because of its accurate control on transducer-sample alignment. However, little work has been found to employ this transducer to systematically characterize stiffness constants of anisotropic solids due to the absence of the mathematic model that describes the relationship between stiffness constants and surface wave velocity. The purpose of this dissertation is to develop a new approach that enables a lens-less line focus ultrasound transducer to characterize stiffness constants of anisotropic materials through simultaneously measurement of both Rayleigh surface wave and longitudinal bulk wave. Firstly, a lens-less line focus PVDF (Polyvinylidene fluoride) ultrasound transducer and corresponding testing system have been established. This inhouse developed testing system is then experimentally calibrated using metal alloys made by both conventional and additive manufacturing methods. The comparison results demonstrate reasonably good accuracy to characterize elastic constants of isotropic materials. Secondly, mechanistic models for the relationship of wave propagation with stiffness constants are developed for more complicated Cubic and Trigonal anisotropic materials. Again, the model validation is conducted by comparing model prediction and experimental measurement using

single crystal silicon and quartz as examples. Additionally, a generalized form of model development process is summarized in the end, and this form can be used as a guideline to develop numerical model for surface wave propagating along any direction on any types of crystallographic structures. As an example, the generalized model development process is utilized to develop the mechanistic model for orthorhombic materials. Based on the theoretical and experimental studies in this dissertation, a novel elastic stiffness constant characterization method is developed and characterized, which largely simplified the measurement procedure and minimized the sample used for fully characterization of stiffness constants of different types anisotropic solids.

Table of Contents

List of Tables

List of Figures

Preface

I would like to express my sincere appreciation to my advisor Professor Qing-Ming Wang for his support and guidance through the course of my graduate studies. I would like to thank the members of my doctoral committee, Professors Minking Chyu, William Slaughter and Kevin P. Chen, for their support, comments and suggestions as committee members.

I am very grateful to my collaborators Dr. Yizhong Wang, Dr. Hongfei Zu, Dr. Huiyan Wu, Dr. Mohammad Gudarzi, Dr. Zhimin Sun, Rongjie Liang, Min Zheng, Shijing Luo, Xuande Zhang, Yuxiang Wang, Pei-Yuan Hsiao, Xueqi Li, Zihao Zhong, Weibo Gao, Saleh Alghamdi, and Menghan Jiang for their help in my research work.

I would like to thank my parents, my parents in law, and my husband Hanfei for their love, support and encouragement.

1.0 Introduction

This chapter presents an overview of mechanical property characterization methods, their limitations and the literature background of the development and application of line-focus ultrasound transducer. Based on the literature review, the motivation and the research objectives which emphasize the significance of this dissertation are addressed.

1.1 Background and Motivation

Elastic stiffness constants are the primary parameters to evaluate the mechanical property of solid materials [1]. Characterization of the elastic constants with accuracy and convenience plays an important role in the engineering application of the materials.

The characterization of stiffness constants of anisotropic solids can be achieved by experimental approaches such as resonant method and ultrasound method[2-4]. Resonant method is based on the measurement of frequency spectrum of the vibration of sample generated on specific direction. By identifying the resonate frequency which is only dependent on material property, the stiffness constants can be characterized. Resonant method is widely used on anisotropic materials with complicated asymmetric character such as cubic, trigonal etc. [4]. The sample must be fabricated in the geometry that follows standards, such as ISO[5], ASTM[6], and other theoretical protocols[7] to eliminate the interference from vibration in unwanted directions. However, the identification of the resonate frequency is still challenging because of the complicity of vibration in solid in nature, thus it requires strong theoretical background in vibration and

experience in experiment skill, which restrict the application of resonant method to industrial field. The stiffness constants can also be characterized by measuring the propagation velocity of acoustic waves generated in solid with ultrasound transducer[8]. Bulk acoustic waves are often generated on the thickness direction of testing sample with longitudinal transducer for longitudinal wave, whose particle polarize on the same direction with propagation, and transverse transducer for transverse wave, whose particle polarize on the orthogonal direction with propagation[1] [9]. The wave mode is decided from the type of transducer used for wave generation and based on the time delay between the pulse and echo, the wave velocity can be determined. The ultrasound method simplifies the measurement requirement with less requirement on sample geometry and easier data analysis by restrict wave mode through the types of transducer used making it more practical in wider application. However, as asymmetric character grows more complex in the anisotropic material, the wave propagation becomes complicated. For example, there are two transverse bulk waves propagating on [110] direction of single crystal silicon, one of which polarize on $[\bar{1}10]$ direction with velocity 4673m/s and the other polarize on [001] direction with velocity 5874m/s [1]. This wave mode complicity introduce uncertainty on the utilization of transverse wave for stiffness constant characterization. In the meantime, the velocity measurement accuracy highly relies on the alignment accuracy between transducer and testing sample, since most of the bulk wave transducers are contact type which requires manual alignment. Therefore, measurement errors can be easily introduced due to possible misalignment without accuracy control. Thus, there is a need for a transducer system which provides consistent position alignment with predictable wave propagation character in anisotropic material with complex asymmetry.

Line-focus ultrasound transducer, which generates waves in solid material by immerging both transducer and sample in water couplant, has been used to measure the surface wave velocities

in isotropic [10, 11] and anisotropic solids since 1980s[12-16]. Because the transducer does not directly contact with the sample material during testing, the measurement direction could be easily changed by connecting the transducer or the water container to motorized stages. Elastic constants of isotropic solids have been characterized using Rayleigh surface wave measured by line-focus ultrasound, and bulk wave velocity measured by a separate bulk wave transducer[13] [17]. However, characterization of stiffness constants of anisotropic materials using surface wave measurement remains challenging and few studies provides convincing and practical approach to calculate anisotropic stiffness constants based on measured surface wave velocities. This is due to the lack of velocity equations that provide the direct relationship between surface wave generated on specific direction and the stiffness constants. The only analytical velocity equation is on the surface wave propagating the crystallographic axis in cubic material[1]. That explains the fact that the only a few attempts made on anisotropic solid from literature are limited to the evaluation on the special case of surface wave on crystallographic planes in cubic solid structure [11, 14, 16, 18-21]. However, as the number of independent stiffness constants increases for anisotropic material, single Rayleigh wave equation with one longitudinal wave equation is insufficient to analytically solve all the stiffness constants.

On the other hand, there are a lot of scientists in physics have been studying the surface wave propagation character since early 1900s. Since Rayleigh reported the Rayleigh surface wave propagating character on semi-infinite isotropic solid in 1885 [22], and Lamb reported surface wave propagating on isotropic plates 1900 [23], the surface wave propagation has been analytical studied [24] and solved by numerical approach [18, 25, 26]. Nowadays, the propagation theory can be found from most books in physical acoustics [27] or wave propagation in solids [1]. However, when consider the application of the wave propagation theory to characterize elastic

constants of anisotropic solid, the analytical wave equations are either to general and abstract that hard to be applied on specific material, or the specific equation is given for special directions that could not cover the directions needed to fully characterize all elastic constants. Not enough sources for equations that are accessible for direct use to characterize the elastic constants of anisotropic solid. The line-focus ultrasound system cannot be used for stiffness constant characterization unless analytical equations are derived.

In summary, when applied for testing anisotropic materials particularly for industrial fields, current material characterization methods have practical challenges due to either the complexity in distinguishing the resonant frequency out of many vibration modes or measurement uncertainty introduced during transducer alignment on test samples. Although the line focus ultrasound method can trigger surface wave and bulk wave in solid test sample simultaneously and have relative accurate control on transducer alignment, so far it is only limited to measure surface wave velocity and use their directional variation as indirect evidence of material anisotropy. This limitation is due to the absence of the mathematic model that describes relationship between stiffness constant and Rayleigh surface wave velocity. For such reason, little work from literature has been found to employ this method to systematically characterize stiffness constants of anisotropic solids.

1.2 Research Objectives

The major objective of this research is to develop a new approach that enables the line-focus ultrasound transducer to characterize stiffness constants of anisotropic materials via simultaneous measurement of both Rayleigh surface wave and longitudinal bulk wave.

1.2.1 Fabrication and calibration of Line-focus transducer using Isotropic Materials

The objective of this section is to fabricate and calibrate a line-focus ultrasound transducer which can be used to characterized elastic stiffness constants through the measurement of Rayleigh surface wave and longitudinal bulk wave velocity. Therefore, a lens-less line focus ultrasound transducer is fabricated using PVDF (Polyvinylidene fluoride) piezoelectric thin film as the active element. The experimental measurement accuracy of the line-focus transducer is achieved using different types of commercial metal alloys, which are typical examples for isotropic material.

Isotropic materials, which exhibit same mechanical property regardless of measurement direction, have the least number of independent stiffness constants (i.e. 2 independent constants) and have well developed mathematical model that describes the relationship between stiffness constants and velocities of different mode such as longitudinal and transverse bulk wave and Rayleigh surface wave. Utilizing the line-focus ultrasound transducer and the time-resolved defocusing method for data analysis, the longitudinal bulk wave velocity and Rayleigh surface wave velocity are obtained. The elastic constants such as Young's modulus and Poison's Ratio are calculated and compared with the ones from the official datasheet which is obtained through the conventional tensile testing method.

The transducer is then applied for the measurement on alloys made by additive manufacture technology, which possibly have some anisotropy character due to the fabrication process. The Rayleigh wave velocity is used to indicate the anisotropy, and if the anisotropy is minimum, these metal alloys will also be taken as isotropic materials and the elastic constants would be characterized.

1.2.2 Mechanistic Model development and validation for Cubic Materials

Line-focus ultrasound transducer has been limited to measure surface wave velocity of anisotropic materials due to the lack of mathematic model. The only available analytical equation for anisotropic materials is on the Rayleigh surface wave propagating on the crystallographic axis on the mirror plane in cubic materials. Therefore, we use cubic materials as the starting point for the development of mechanistic model of anisotropic solids. Cubic materials refer to the materials that has cubic crystal structure. Cubic materials have three independent stiffness constants and require three velocities measured to characterize stiffness constants.

The mechanistic model of Rayleigh wave propagating on three kinds of directions are developed: crystallographic axis on a crystallographic mirror plane (for example [100] direction on (100) plane), axis on a non-crystallographic plane (for example [110] direction from (110) plane), and regular direction on a non-crystallographic plane (taking [111] direction from (110) plane as an example). The model for these three directions covers all the possible Rayleigh surface wave propagation directions on a cubic material. The model is validated experimentally using single crystal Silicon as an example. Based on the validation result, a novel approach to characterize stiffness constants of cubic material by combinations of longitudinal bulk waves and Rayleigh surface waves is proposed to minimize the calculation and measurement complexity. The novel approach is applied to characterize elastic stiffness constants, which is compared with reference value from literature.

1.2.3 Mechanistic Model development and validation for Trigonal Materials

The research is taken a step deeper on development of mechanistic model for Trigonal materials which do not have a mirror plane in the crystal structure and have 6 independent stiffness constants, this requires more velocities to be measured to characterize all the stiffness constants. Based on the theoretical study on cubic materials, using some longitudinal bulk waves together with Rayleigh surface wave can simplify the calculation process comparing using Rayleigh surface wave alone. Therefore, it is not necessary to develop the model for Rayleigh surface wave propagating along any common directions. In this study, the mechanistic model for Rayleigh surface wave propagating on crystallographic XZ-plane and XY-plane is developed, based on which the model for wave propagating on the crystallographic axes X, Y, and Z are developed. The model for Rayleigh wave propagating along X, Y and Z directions is validated through experimentally measurement on Quartz crystal. The model of Rayleigh surface wave together with the velocity equations for longitudinal bulk wave on X, Y and Z directions are used to fully characterize the stiffness constants.

1.2.4 Mechanistic Model development for Orthorhombic Materials

Based on the theoretical study of Rayleigh surface wave propagating on different directions of anisotropic materials such as Cubic and Trigonal materials, a generalized mechanistic model development process can be summarized. This approach can be used to develop the mathematical relationship between Rayleigh surface wave propagating on any generalized directions on solid materials with any given types of crystallographic structure.

This approach is applied to develop the mechanistic model for orthorhombic materials which has 9 independent stiffness constants, and therefore, requires the measurement of 9 wave velocities to characterize all the stiffness constants. The wave velocity equations of longitudinal bulk wave propagating on X, Y and Z directions is developed based on the Christoffel equation. The mechanistic model for Rayleigh wave propagating on the three crystallographic planes (i.e. XY, YZ and XZ planes) are developed, based on which the secular equations of the special cases when the Rayleigh wave propagates on the three crystallographic axes (i.e. X, Y, and Z axis) are obtained. Based on the model developed, the 9 independent stiffness constants of orthorhombic material can be easily characterized using three longitudinal bulk wave velocities and six Rayleigh surface wave velocities which can be measured by one line-focus transducer using single sample.

2.0 Theoretical Foundation

This chapter presents and reviews some fundamental concepts such as stiffness constants, acoustic wave propagation character in isotropic solid, and reflection and refraction principle at fluid-solid interface of isotropic solid, which are the critical foundation for the theoretical and experimental study in this dissertation.

2.1 Stiffness Constants

A solid is elastic if it can return to its initial state when the external force that is responsible for deformation is removed. This is the work of internal stress of the material.

For homogenous elastic solid, there is a one to one relationship between the stress and strain, which is described by Hooke's law. Assuming small deformation, the linearized Hooke's law is given as:

$$T_{ij} = c_{ijkl} S_{kl} \tag{2-1}$$

The coefficients c_{ijkl} are components of the stiffness tensor (4 rank, 6×6 matrix) which expresses the general possible linear relation between the second rank tensors T_{ij} (stress tensor) and S_{kl} (strain tensor). The law was first stated by Hooke in 17th century from elastic spring. As T_{ij} and S_{kl} are symmetric, there is $c_{ijkl} = c_{jikl} = c_{ijlk} = c_{jilk}$. This reduces the number of independent stiffness constants from 81 (3^4) to 36. The independent elastic stiffness constants can thus be

represented in terms of indices α and β with values 1 to 6, such that $c_{\alpha\beta} = c_{ijkl}$ where α is related to (ij) and β relates to (kl) in accordance with:

$$\begin{aligned} (11) &\leftrightarrow 1 \quad (23) = (32) \leftrightarrow 4 \\ (22) &\leftrightarrow 2 \quad (13) = (31) \leftrightarrow 5 \\ (33) &\leftrightarrow 3 \quad (12) = (21) \leftrightarrow 6 \end{aligned} \tag{2-2}$$

Based on Maxwell's relation [1], $c_{\alpha\beta} = c_{\beta\alpha}$ so that the 6×6 matrix is symmetric about its main diagonal. This property reduces the number of independent components to 21. Triclinic crystals, which has a center of symmetry with no restrictions, have 21 independent elastic constants [1]. Fortunately, other crystals systems have a symmetry that reduce the number of independent constants.

For example, for **isotropic** solid, the mechanical property is independent of the choice of the coordinate axes, consequently the property are specified by two independent constants with stiffness matrix given as [28]:

$$\left(c_{\alpha\beta}\right) = \begin{vmatrix} c_{11} & c_{12} & c_{12} & 0 & 0 & 0 \\ c_{12} & c_{11} & c_{12} & 0 & 0 & 0 \\ c_{12} & c_{12} & c_{11} & 0 & 0 & 0 \\ 0 & 0 & 0 & c_{66} & 0 & 0 \\ 0 & 0 & 0 & 0 & c_{66} & 0 \\ 0 & 0 & 0 & 0 & 0 & c_{66} \end{vmatrix} \quad \text{with} \quad c_{66} = \left(c_{11} - c_{12}\right)/2$$

Elastic constants such as Young's modulus (E) and Poisson's ratio (ν) are defined to characterize the mechanical property of isotropic materials in industrial applications given:

$$\begin{aligned} E &= c_{11} - 2\frac{c_{12}^2}{c_{11} + c_{12}} \\ \nu &= \frac{c_{12}}{c_{11} + c_{12}} \end{aligned} \tag{2-3}$$

The general invariance condition for stiffness tensor in orthonormal coordinate (X,Y,Z) is given as:

$$c_{ijkl} = \alpha_i^p \alpha_j^q \alpha_k^r \alpha_l^s c_{pqrs} \quad \textbf{(2-4)}$$

Therefore, the symmetry of crystals reduces the number of independent components in the tensor with α is the matrix for the axis change.

Crystals in the **orthorhombic** system are characterized by having three orthogonal dyad axes, which are taken as coordinate axes (X,Y,Z), resulting in the remaining components are those having indices repeating an even number of times giving 9 independent constants.

$$\left(c_{\alpha\beta}\right) = \begin{vmatrix} c_{11} & c_{12} & c_{13} & 0 & 0 & 0 \\ c_{12} & c_{22} & c_{23} & 0 & 0 & 0 \\ c_{13} & c_{23} & c_{33} & 0 & 0 & 0 \\ 0 & 0 & 0 & c_{44} & 0 & 0 \\ 0 & 0 & 0 & 0 & c_{55} & 0 \\ 0 & 0 & 0 & 0 & 0 & c_{66} \end{vmatrix} \text{ orthorhombic (9).}$$

For **cubic** crystals, there are at least 4 triad axes and three direct dyad axes, and the latter is taken as coordinate axes, the non-zero components are the same with orthorhombic, but the triad axes reduces the number of independent constants to 3, which is given as

$$\left(c_{\alpha\beta}\right) = \begin{vmatrix} c_{11} & c_{12} & c_{12} & 0 & 0 & 0 \\ c_{12} & c_{11} & c_{12} & 0 & 0 & 0 \\ c_{12} & c_{12} & c_{11} & 0 & 0 & 0 \\ 0 & 0 & 0 & c_{66} & 0 & 0 \\ 0 & 0 & 0 & 0 & c_{66} & 0 \\ 0 & 0 & 0 & 0 & 0 & c_{66} \end{vmatrix} \text{ cubic (3).}$$

Crystals in the **trigonal** system have single axis in the order greater than two have a more complicated non-diagonal rotation axes resulting a more complicated matrix [1] with 6 independent stiffness constants.

$$\left(c_{\alpha\beta}\right)=\begin{vmatrix} c_{11} & c_{12} & c_{13} & c_{14} & 0 & 0 \\ c_{12} & c_{11} & c_{13} & -c_{14} & 0 & 0 \\ c_{13} & c_{13} & c_{33} & 0 & 0 & 0 \\ c_{14} & -c_{14} & 0 & c_{44} & 0 & 0 \\ 0 & 0 & 0 & 0 & c_{44} & c_{14} \\ 0 & 0 & 0 & 0 & c_{14} & c_{66} \end{vmatrix} \text{ trigonal (6), } c_{66}=\left(c_{11}-c_{12}\right)/2$$

2.2 Propagation Principle of Acoustic Wave in Solid

When an elastic wave propagation through a continuous solid, the solid is locally in motion. The displacement u_i of an arbitrary point in the solid with coordinate x_k follows Newton's law:

$$\rho\frac{\partial^2 u_i}{\partial t^2}=\frac{\partial T_{ij}}{\partial x_j} \tag{2-5}$$

Consider the first order linear behavior of an elastic solid which ignore the piezoelectricity, stress tensor T_{ij} in terms of generalized stiffness tensor c'_{ijkl} and displacement have the relationship though the linearized Hooke's law:

$$T_{ij}=c'_{ijkl}\frac{\partial u_l}{\partial x_k} \tag{2-6}$$

The generalized stiffness tensor c'_{ijkl} is with the coordinate x_k is obtained by rotating stiffness tensor c_{ijkl} (using $c'_{ijkl}=\alpha_i^p\alpha_j^q\alpha_k^r\alpha_l^s c_{pqrs}$). The stiffness tensor c_{ijkl} is defined in the crystallographic axes XYZ. When the propagation direction is along the crystallographic axes, c'_{ijkl} is the same with c_{ijkl}.

The wave equation is then given by:

$$\rho \frac{\partial^2 u_i}{\partial t^2} = c'_{ijkl} \frac{\partial^2 u_l}{\partial x_j \partial x_k} \quad \textbf{(2-7)}$$

2.2.1 Bulk Wave

Consider the propagation of a plane wave in solid, the wave equation will be first converted to Christoffel's equation, that the problem solving the second order partial differential equations is converted to eigenvalue/eigenvector problem.

Consider common case that the propagation is along crystal axes (i.e. $c'_{ijkl} = c_{ijkl}$), the plane wave propagating in the direction of unit vector $\mathbf{n} = (n_1, n_2, n_3)$ and the direction unit vector is perpendicular to the wave fronts $\mathbf{n} \cdot \mathbf{x} =$ constant, we consider solution $u_k = {}^{\circ}u_k F((ik)(Vt - n_j x_j)$, where ${}^{\circ}u_k$ is wave polarization which is independent of x_j and t, V is the phase velocity. Substitute the solution into the wave equation.

$$\frac{\partial^2 u_i}{\partial t^2} = {}^{\circ}u_i \left(ikV\right)^2 F'' \quad \textbf{(2-8)}$$

$$\frac{\partial^2 u_l}{\partial x_j \partial x_k} = {}^{\circ}u_l \left(ik\right)^2 n_j n_k F'' \quad \textbf{(2-9)}$$

The wave equation becomes:

$$\rho \left(ik\right)^2 V^2 F''{}^{\circ}u_i = c_{ijkl} \left(ik\right)^2 n_j n_k F''{}^{\circ}u_l \quad \textbf{(2-10)}$$

Which leads to Christoffel's Equation:

$$\rho V^2 {}^{\circ}u_i = c_{ijkl} n_j n_k {}^{\circ}u_l \quad \textbf{(2-11)}$$

Introducing the Christoffel Tensor:

$$\Gamma_{il} = c_{ijkl} n_j n_k \tag{2-12}$$

For a given wave propagation direction, there are three phase velocities in general, which are solutions of secular equation:

$$\left| \Gamma_{il} - \rho V^2 \delta_{il} \right| = 0 \tag{2-13}$$

Equation (2-9) is the general velocity equation for bulk waves. From this equation, it could be proved that three plane waves with orthogonal polarization directions can propagate in the same direction with different velocities [28]. The displacement vector $\mathbf{u}$ may not always perpendicular or parallel to the propagation direction $\mathbf{n}$. The wave whose polarization closest to $\mathbf{n}$ is quasi-longitudinal, and the others are quasi-transverse. Longitudinal waves usually travel faster than transvers waves. The special cases when $\mathbf{u} \parallel \mathbf{n}$ and $\mathbf{u} \perp \mathbf{n}$ are pure longitudinal and transverse waves [29], which holds true for isotropic materials as shown in Fig. 2-1 and Fig. 2-2.

Using equation (2-9), the bulk wave velocity equations can be obtained, and the equations for isotropic are:

$$\rho V_L^2 = c_{11} \tag{2-14}$$

$$\rho V_T^2 = c_{66} = \left(c_{11} - c_{12} \right) / 2 \tag{2-15}$$

Since c_{12} should always positive, $V_L > \sqrt{2} V_T$ holds true for all isotropic materials.

Similar equations for cubic, trigonal and orthorhombic materials will be summarized in the following corresponding chapters.

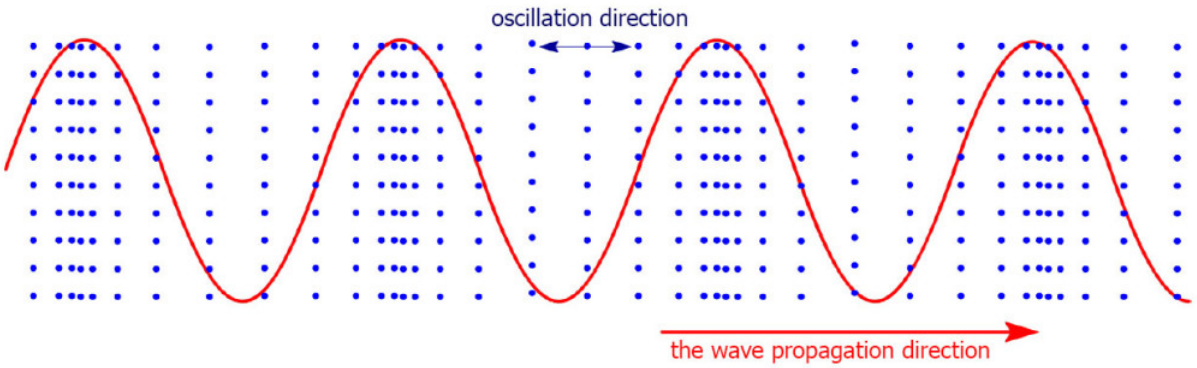

Figure 2-1 Diagram of Propagation of Longitudinal bulk waves [30]

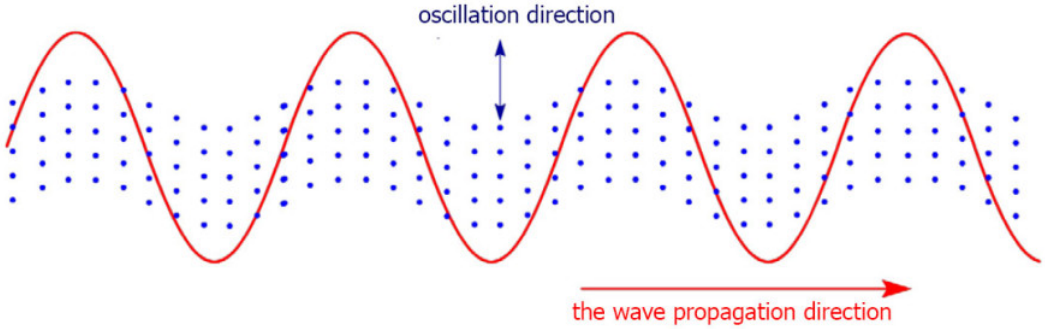

Figure 2-2 Diagram of Propagation of Transverse bulk waves [30]

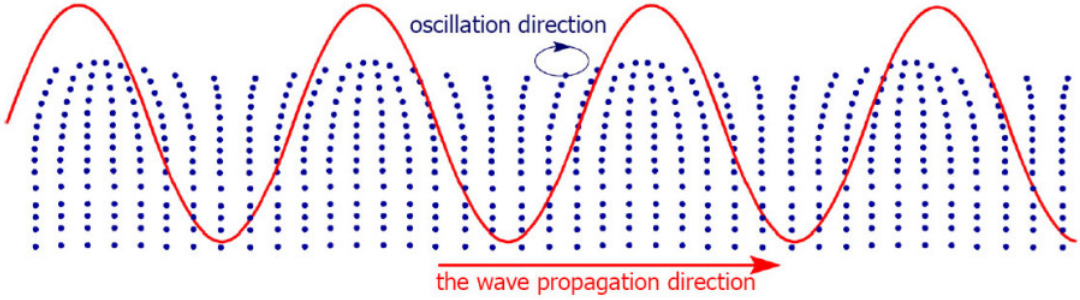

Figure 2-3 Diagram of Propagation of Surface waves [30]

2.2.2 **Rayleigh Surface Wave**

The analysis of propagation of bulk wave assumes that the dimension of 'point' is small comparing with dimension of solid, in other words, the solid is infinite and the wave propagation does not encounter any boundaries. When the solid is not infinite, the boundary imposes conditions on the wave propagation. Influenced by the boundary, wave may reflect, change propagation direction and may also change wave type. Based on the reflection and refraction theory of a given incident wave, guided wave would be generated.

In 1885, Lord Rayleigh developed analytical mathematical description on waves guided by the free surface of an isotropic semi-infinite solid [31]. This wave has two displacement components with a phase difference of $\pi/2$ resulting an elliptical polarization at surface where the vertical axes is about 1.5 times of horizontal axes [31]. In the Fig. 2-4, a semi-infinite crystal with Rayleigh wave propagation along x_1. The sagittal plane (x_1, x_2) contains the propagation surface normal x_2 and the propagation direction x_2. In Fig. 2-4, s is the free surface, n is the propagation direction, Fig. 2-4(a) shows the decrease of displace component with depth, and Fig. 2-4(b) shows the displacement of the surface.

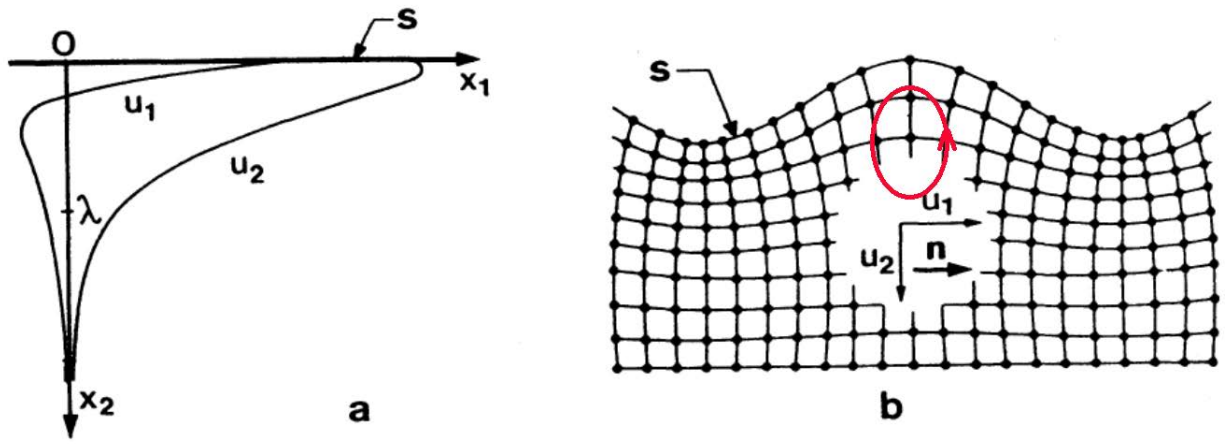

Figure 2-4 Rayleigh Wave in isotropic semi-infinite solid [28]

In 1904, Lamb published his study on the propagation character of Rayleigh wave excited by vertical pulse force[32]. In his study, the disturbance of Rayleigh wave in time domain have the character in Fig. 2-5. The combined wave form has the character that gradually increasing negative displacement after which decreasing back to the balance position then increase positive displacement. This character is then verified by the Green function simulation [33], and the experiment results from this study.

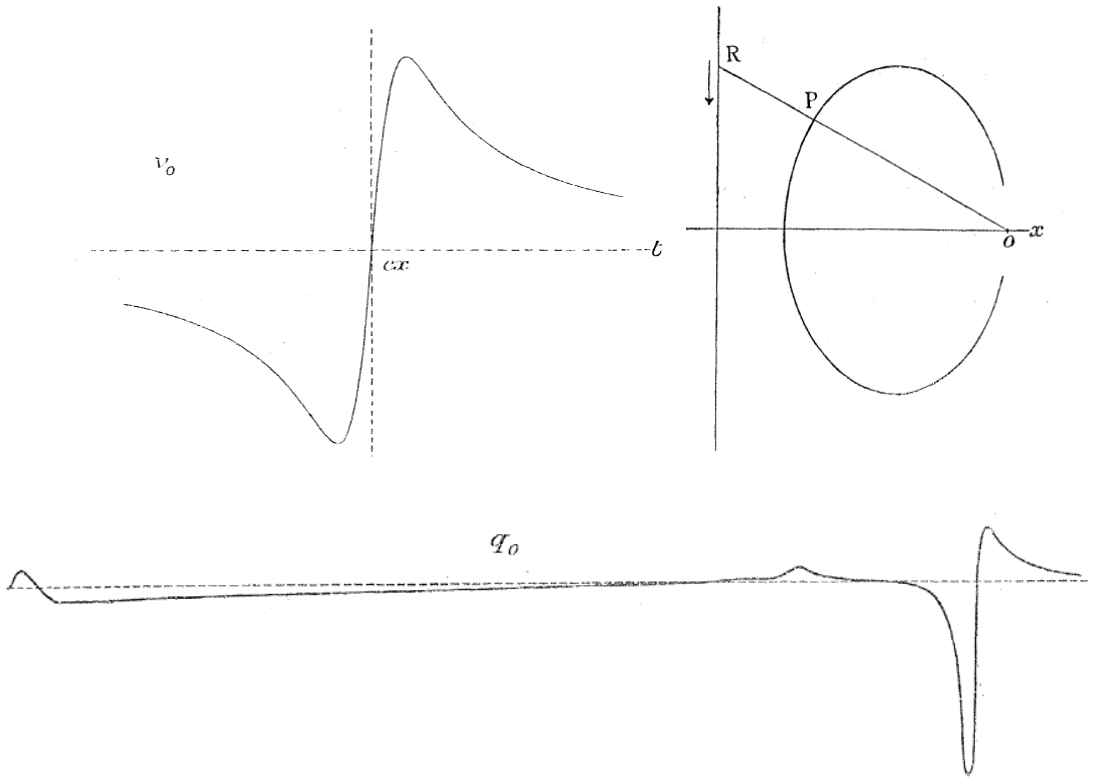

Figure 2-5 The Rayleigh Wave form derived by Lamb in 1904[32]

The propagation of Rayleigh surface wave in crystals is challenging in algebraic analysis. The mechanical displacement not only need to satisfy the three coupled wave equations, but also need to satisfy three boundary conditions, which is free of stress at the boundary for Rayleigh type waves. The Rayleigh velocity equation must satisfy the secular equation from equation of motion and the secular equation from mechanical boundary condition. The form of solutions of equation of motion is also changes since the decay in the thickness direction need to be considered.

2.3 Reflection and Refraction at Liquid-Solid Interface

The acoustic wave generation and propagation in solid that is submerged in water couplant is based on the fundamentals of reflection and refraction at liquid-solid interface. The direction of refracted acoustic wave is described by Snell's Law [1] shown in Fig. 2-6.

$$\frac{V_W}{\sin\theta_I} = \frac{V_L}{\sin\theta_L} = \frac{V_T}{\sin\theta_T} \tag{2-16}$$

The incident wave is a longitudinal wave with incident angle θ_I and propagation velocity V_W in water as medium. Given to the mismatch of acoustic impedance ($Z_W = \rho_W V_W \neq Z_S = \rho_S V_L$) in water and solid medium, reflection and refraction occur at the interface. The reflection angle is the same with incident angle. As solid material supports transverse particle movement, both longitudinal wave and transverse waves can be generated, and the propagation directions (θ_L and θ_T) of the refracted longitudinal and transverse wave are determined through equation (2-8).

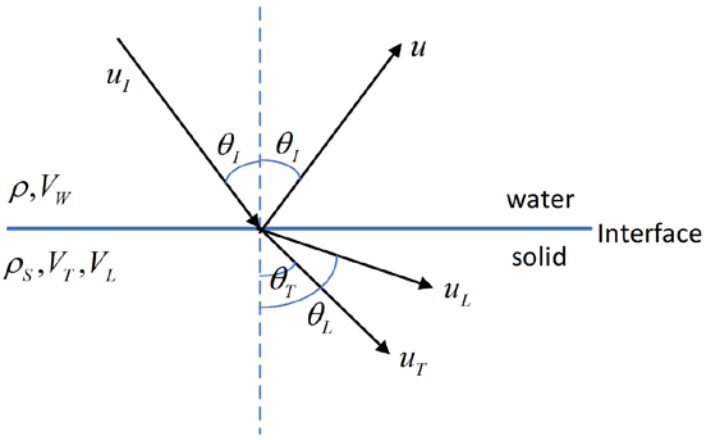

Figure 2-6 Reflection and refraction at interface between a water and an isotropic solid

As we can see, for the incidence wave makes an angle with the normal to the interface (i.e. $\theta_I \neq 0$), this angle naturally changes the direction of the reflected and refracted waves. If $V_L > V_W$

(2-8) there is an incident angle θ_1 such that $\sin\theta_1 = \frac{V_W}{V_L}$ with $\theta_L = 90°$, there is no longitudinal wave transmitted straightforwardly into solid. This incident angle is called the first critical angle. Similarly, the second critical angle is defined as the incident angle reaches θ_2 that $\sin\theta_2 = \frac{V_W}{V_T}$. If the incident angle continuously to increase after passes the first and second incident angle, the Rayleigh surface wave is generated when the incident angle equals to θ_R that $\sin\theta_R = \frac{V_W}{V_R}$ where V_R is the Rayleigh surface wave propagating velocity in that solid medium as shown in Fig. 2-7. This is the working principle to generate Rayleigh surface wave in a solid with an ultrasound transducer.

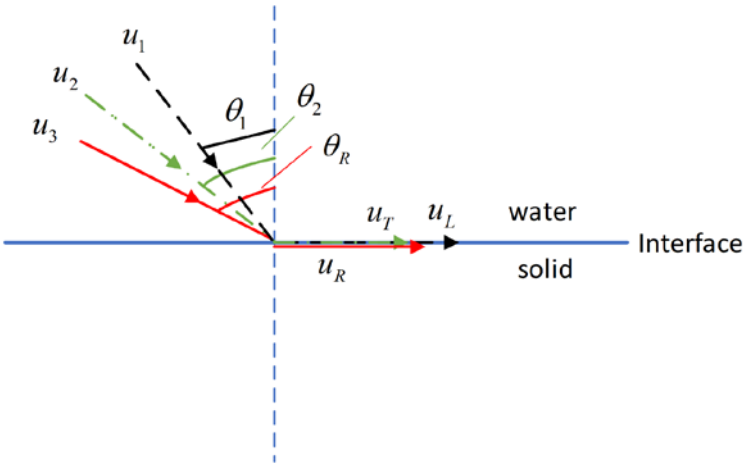

Figure 2-7 The critical angles of Refraction at interface

3.0 Calibration of Line-focus Ultrasound system using Isotropic Materials

The fabrication and experimental calibration of a line-focus ultrasound transducer system is presented in this chapter. The line-focus transducer was made by conforming piezoelectric PVDF thin film to a convex cylindrical surface with a tungsten-powder-loaded epoxy resin composite as the backing material. Both longitudinal bulk wave and Raleigh surface wave can be generated in the metal alloys by pulse excitation using the ultrasound transducer system that consists of a pulse generator and receiver, an X-Y-Z stage and a rotary stage, a line-focus transducer, an oscilloscope and a computer for data acquisition and analysis. Using the time-resolved defocusing method, a series of received waveform was collected at different defocus position (z). The longitudinal bulk wave velocity (c_L) and surface wave velocity (c_R) were obtained by analyzing the waveforms in the time domain.

The measurement system is first calibrated by using commercial metal alloys including stainless steel, aluminum, and copper by characterizing the elastic constants and comparing with the values from materials data sheet. It is then applied to characterize the elastic constants of SS316, IN725, AlSi10Mg, and Ti64 alloys made by different additive manufacturing methods. Due to the layer by layer fabrication character, the testing parts could have a course surface roughness and some anisotropic character on different building directions. The effect of surface roughness and anisotropy of materials are investigated, and the results indicate (i) the metal alloys can be modeled as isotropic material and the anisotropy introduced through fabrication process can be ignored; (ii) the measured c_R is a parameter that representing material property without the interference from surface roughness. the surface roughness does not interfere the surface wave propagation as it is two magnitude smaller than the surface wave length. Thus, the elastic constant

of the additive manufacture can be obtained. The results show the ultrasound transducer system is very promising for characterizing the materials properties of metal alloys.

3.1 System Configuration and Fabrication

A line focus ultrasound transducer system is made to generate Rayleigh surface wave and longitudinal bulk wave in solid. As presented in the system schematic diagram in Fig. 3-1, the testing sample is placed on the bottom of a water container in which deionized water is used as couplant for ultrasound propagation between the piezoelectric transducer and the sample. The relative position between the transducer and the sample is precisely manipulated by fixing the transducer to motorized linear and rotary stages both of which are controlled by a stage controller (DS102, Suruga Seiki Ltd.) driven by a LabView Program. Specifically, the linear stage controls the vertical distance between the transducer and the sample while rotary stage controls the surface wave propagation direction on the sample. The line focus piezoelectric transducer is used for both generating and receiving acoustic wave and its echo. A Pulser/receiver (5072PR, OLYMPUS) sends an electric pulse signal on the transducer to generate acoustic wave in water and receives echo from solid sample. The received signal is converted to voltage response through the same transducer and is presented on a digital oscilloscope (4034A, Agilent Technologies) with sampling frequency of 350MHz. A lens-less line focus transducer is fabricated by attaching a piezoelectric thin film to a cylindrical concave surface made by high damping factor backing material which is pre-casted into an aluminum cage [33]. In this study, A PVDF (Polyvinylidene fluoride) piezoelectric thin film (DT-028, NEG, Measurement Specialties (MEAS), TE Connectivity Ltd.) of size of 60 mm×12.5 mm, and thickness of 30 μm is made into a transducer with focal distance(

l) 25 mm, and aperture half angle ($\theta_{\max}$) of 35 degree. The backing material is a mixture of tungsten power and low viscosity epoxy (Devcon 2 Ton Epoxy, ITW Polymer Adhesives) with weight ratio 2:1 to achieve a large acoustic impedance mismatch with the PVDF piezoelectric element so that a broadband pulse can be properly generated. This PVDF transducer is presented in Fig. 3-2.

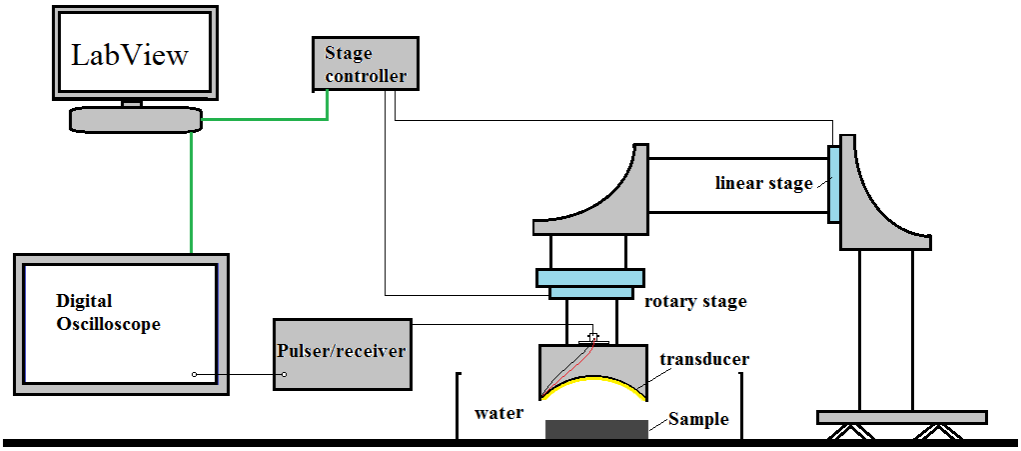

Figure 3-1 Schematic diagram of the measurement system

Three kinds of commercial metal alloys, specifically Stainless steel 420, Aluminum 6061, and Copper 110, are first tested for the calibration of the line focus transducer on elastic constant characterization of isotropic material. The commercial metal alloys are fabricated by traditional casting method and machined into bars 20*mm* wide and 6 *mm* thick for general application, and the bars are cut into 60*mm* long testing samples.

After system being calibrated and validated, on the additive manufactured materials are then tested to study the anisotropic character. Binder jet and laser sinter methods, two of the popular additive manufacture methods, are employed to fabricate metal parts from powder. Binder

jet using inkjet printer head drops glue-like binding material to hold powder of build part together and then the whole parts are sintered in oven. Whereas, in laser sintering process powder is firstly melt in one thin layer by precisely controlled laser and then cured as building process continues into the next layer. Metal samples made from both methods are experimentally investigated to evaluate the general measurement performance of line focus ultrasound system developed in-house on additive manufactured materials. The testing samples are bars with $30\ _{mm} \times 20\ _{mm} \times 5\ _{mm}$ (length × width × thickness) made by Stainless Steel 316L and Nickel alloy (IN625) fabricated by powder-based binder jet forming (M-flex system, The ExOne Company) and Aluminum alloy (AlSi10Mg), Titanium alloy (Ti64) and Nickel alloy (IN718) fabricated by laser sintering (Model No. M 290, EOS Electro Optical System).

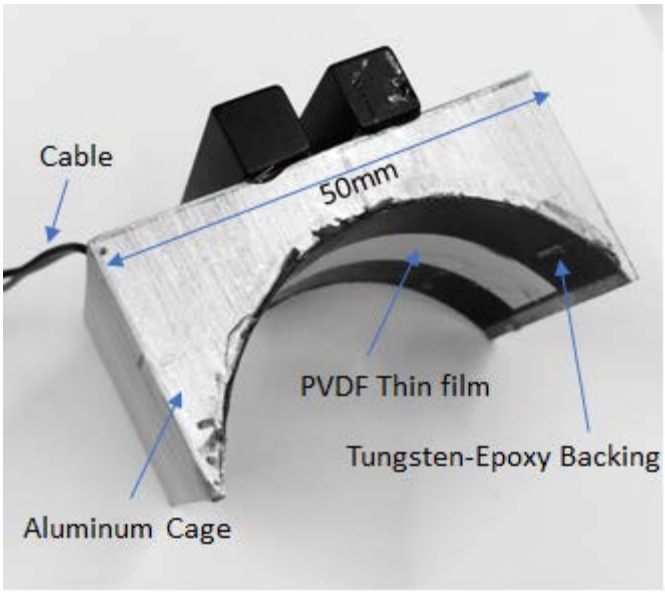

Figure 3-2 A line-focus ultrasound transducer based on PVDF film

3.2 Measurement Principle

The schematic diagram of a side view of waves propagating between a lens-less PVDF transducer and solid sample is presented in Fig. 3-3. When the top surface of the test sample is placed right at the focal plane of transducer (Fig. 3-3(a)), incident waves are concentrated on focal line O on solid top surface and reflected back to transducer travelling through a series of paths such as AOA, BOC and DOE etc., contributing one echo pulse (W1) on the transducer. A portion of the axial waves that are incident through AO can penetrate into the solid and be reflected at the bottom surface of the solid back to transducer. Consequently, another echo pulse echo pulse (W2) will be generated from path AFA, and additional traveling distance within the solid causes the time delay in echo pulse W2 compared to W1.

When the sample moves toward transducer at distance (z), as shown in Fig. 3-3(b), Rayleigh surface wave is generated on solid when the wave incident angle equals to the surface wave critical angle (θ_R). As the Rayleigh surface wave propagates on the solid surface, it continuously leaks energy back to water with angle θ_R , and numerous studies have shown that the ray that can efficiently reach to transducer and generate pulse follows the path BGO'HC [13, 33, 34]. Based on this geometric relationship of the wave propagation, the measurement principle of the Rayleigh surface wave velocity (V_R) can be presented as follows.

The traveling time (t_1) of axial wave directly reflected from top surface (W1 through path AO'A) is:

$$t_1 = \frac{2|AO'|}{V_w} = \frac{2(l-z)}{V_w} \qquad \textbf{(3-1)}$$

where l is the focus distance of transducer, z is the defocus distance, and V_w is the acoustic wave velocity in deionized water ($c_w = 1480 m/s$ at 23℃).

The traveling time (t_2) of wave propagating through path BGO'HC is

$$t_2 = \frac{|BG| + |HC|}{V_w} + \frac{|GH|}{V_R} = \frac{2(l - z/\cos\theta_R)}{V_w} + \frac{2\tan\theta_R}{V_R} \quad \textbf{(3-2)}$$

Thus, the time delay $t_R = t_2 - t_1$ is

$$t_R = 2z\left(\frac{1}{V_w} - \frac{1}{V_w \cos\theta_R} + \frac{\sin\theta_R}{V_R \cos\theta_R}\right) \quad \textbf{(3-3)}$$

Based on the Snell's law of refraction at water-solid interface, there is $V_R = V_w/\sin\theta_R$, and then substituted in (3-3) to obtain

$$z = \frac{V_w}{2(1-\cos\theta_R)} t_R \quad \textbf{(3-4)}$$

Therefore, there is a linear relationship between z and t_R that the surface wave velocity (V_R) can be represented as

$$V_R = \left[\frac{1}{V_w(dz/dt_R)} - \frac{1}{4(dz/dt_R)^2}\right]^{-1/2} \quad \textbf{(3-5)}$$

where dz/dt_R is the slope of z as a function of t_R from (3-4).

Meanwhile, the wave reflected from the bottom surface of the test sample propagates along path AFA has an additional travelling distance O'FO' (two times of the sample thickness) comparing to the axial wave directly reflected from the top surface, which causes a time delay t_L to arrive at the transducer. The longitudinal bulk wave travel within the solid test sample can be calculated by following equation

$$V_L = \frac{2d}{t_L} \quad \textbf{(3-6)}$$

where d is the thickness of the testing sample and t_L is the travel time in the tested solid material.

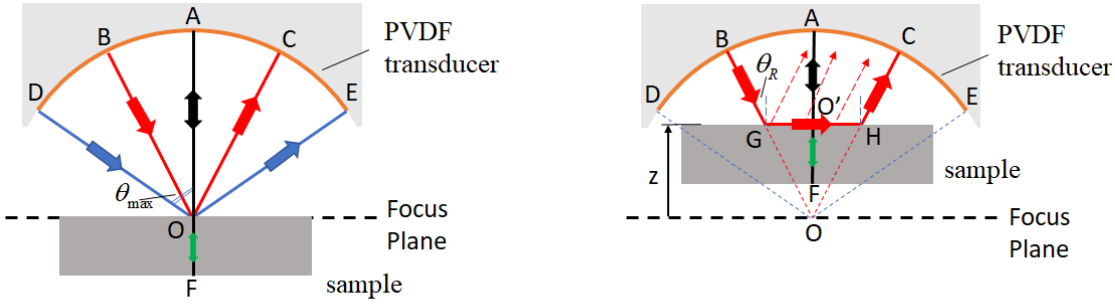

(a) (b)

Figure 3-3 Schematic of wave generation and propagation in solid (a) sample surface at focus plane (b) sample moves towards transducer with distance z

3.3 Experiment and Results

3.3.1 Time domain waveform analysis

The longitudinal bulk wave velocity and Rayleigh surface wave velocity of sample materials are obtained by analyzing the voltage response of the echo signal received by the piezoelectric transducer of from the sample in time domain. The plot for data reduction consists of series of V(z,t) waveforms at various focus locations of Z(t) based on the measurement principle in section 3.

As an example, Fig. 3-4 presents the voltage response (V(t)) of PVDF transducer on two focus positions of Stainless steel 316 made by binder jet method. In Fig. 3-4(a), the waveform is obtained when the sample top surface is right at the focus plane of the transducer (Fig. 3-3(a)). The

two pulses correspond to the transducer responses to the reflected echoes from sample top surface (W1) and bottom surface (W2), respectively. The amplitude of W1 is much larger than W2, because the amplitude of the pulse is determined by the acoustic energy carried by the reflected wave, and more than 90% of energy from incident wave are directly reflected at top surface due to the mismatch of acoustic impedance of water and steel. The time delay (t_L) between either peaks or troughs of W1 and W2 waves is used to calculate the longitudinal wave velocity in solid by equation (3-6), with sample thickness measured from caliper with accuracy in 0.1mm. Fig. 3-4(b) presents the waveform when the sample is out of the focus plane by being moved towards transducer at *z=5mm* as for an example of wave propagation explained in Fig. 3-3(b). The direct reflected echo from the top surface is now only having wave from axial path (i.e. AO') that would efficiently arrive transducer and contribute to most of the energy of received pulse echo, thus the amplitude of W1 is much smaller about 5 fives than from focus position presented in Fig. 3-4(a). Rayleigh surface wave (R) is generated on the sample at critical incident angle θ_R and the time delay (t_R) is measured from the peak of pulses W1 and R. Based on equation (3-5), t_R is a positive number, indicating the arrival time of R always after W1. Considering the fact that the c_L of steel is about 5500m/s and the surface wave generated must have a θ_R smaller than $\theta_{\max}$ (45º), t_L is expected to be larger than t_R at this defocus plane by using equations (3-5) and (3-6). Thus, the three pulses in Fig. 4(b) from left to right in time scale can be identified as W1, R and W2, respectively.

The frequency spectrum of waveform from the above two positions are presented in Fig. 3-5. At focus position, the voltage pulses are from W1 and W2 (Fig. 3-4(a)), and there is a broad spectrum with center frequency about 8MHz shown in Fig. 3-5(a). As the transducer moves toward sample, the acoustic field becomes complicated (shown in Fig. 3-5(b)), the overall spectrum is still

centered around frequency of about 8MHz, and the extra peak that exists at 9.8MHz corresponds to the separation of R from the W1 as shown in Fig. 3-4(b). The energy magnitude of echoes that can be received from transducer decreases as *z* increases with greater defocus. Therefore, it can also be observed substantially lower voltage amplitude in Fig. 3-5(b).

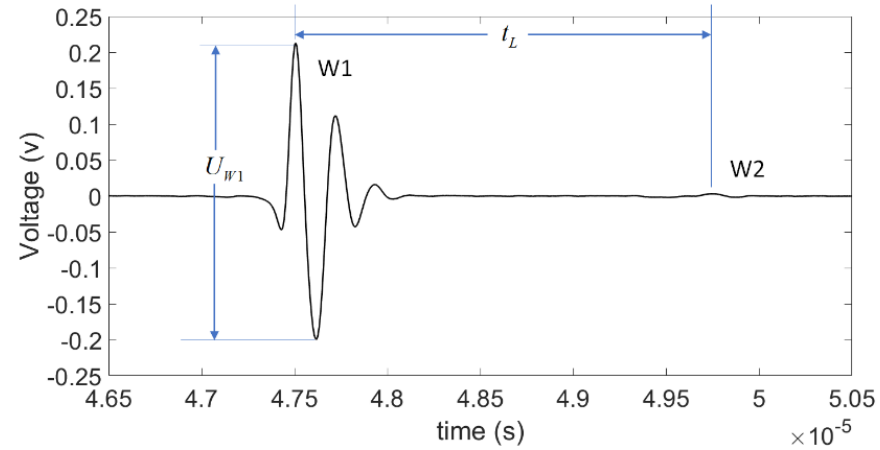

(a)

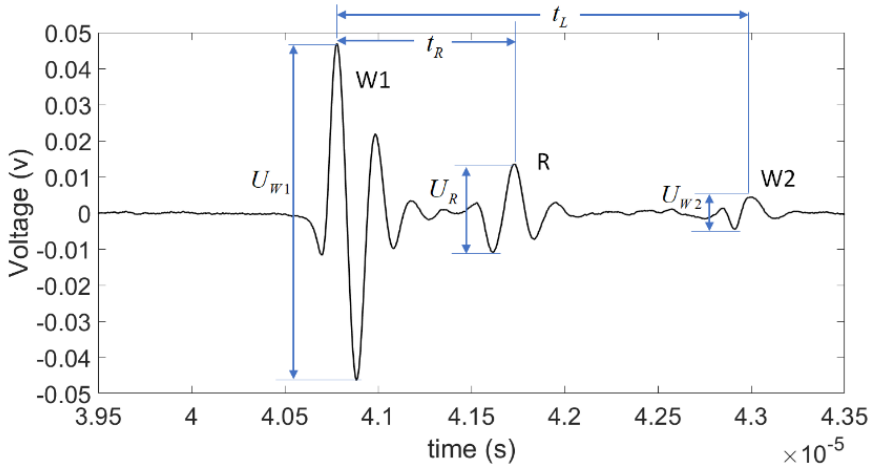

(b)

Figure 3-4 V(t) waveform from Additive manufactured SS316L (a) when sample is placed at the transducer focus position z=0; (b) when sample moves toward the ultrasound transducer at z=5mm.

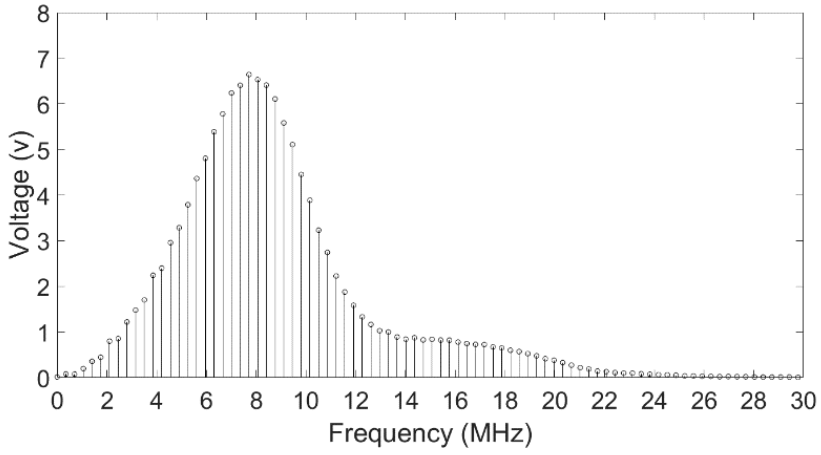

(a)

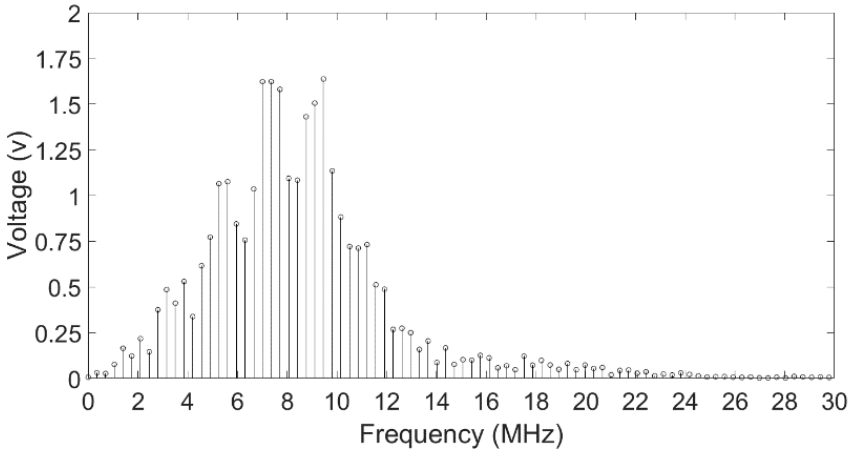

(b)

Figure 3-5 Frequency spectrum of V(t) from Additive manufactured SS316L (a) z=0*mm*; (b) z=5*mm*.

The V(t) waveforms from multiple defocus positions, when z changes from 0 to 8*mm* with incremental of 0.25*mm*, are collected and presented in a $V(z,t)$ plot (shown in Fig. 3-6(a)). According to equations (3-5) and (3-6), compared to the echo W1 from the top surface, the time delay (t_R) of Rayleigh surface wave is expected to linearly increase with z, while the time delay (t_L) of echo from the bottom surface is independent of z. The observation from Fig. (3-6) supports both the theoretical expectations. In addition, it can be seen that another type of surface wave echo, called surface skimming wave and denoted as SS in the plot, is received by the transducer. Compared to Rayleigh surface wave R, its time delay is also in linear relationship with z but much

greater as can be seen the smaller slope of SS wave peak line. Such phenomenon can be explained that the propagation velocity of SS wave is much smaller than R as it is more bounded to the water other than solid, although it is also generated on solid-water interface [25].

The amplitudes (U_{W1}, U_R, U_{W2}) of W1, R and W2 pulses is further analyzed and compared as a function of z as shown in Fig. 3-6(b), in which a base-10 logarithmic scale is used for y-axis due to the distinctive difference in U_{W1}, U_R, and U_{W2} as can be seen from Fig. 3-4. Two important observations can be made here. Firstly, the U_{W1} significantly decreases with z (transducer moves toward sample), because less portion of waves generated from the transducer could initiate echo that can be received efficiently by the transducer with the top surface of the test sample being gradually defocused. While, the pulse amplitudes of R and W2 are less sensitive to the location. Secondly, the amplitude of R wave is one order of magnitude higher than W2 wave, indicating its much stronger wave energy being received by the transducer. Such characteristic makes R wave signal more advantageous in such testing system for material property characterization on a basis of wave propagation and measurement, as its stronger signal is less susceptible to other noise signals, making measurement more accurate and testing system more robust. This is one of the reasons that this work proposes utilizing the Rayleigh surface wave as one of the measurement signals for material property characterization. In Fig. 3-6(c), the peak of R wave is presented at different z locations and corresponding time delays, and thus the slope can be obtained to calculate the Rayleigh surface wave velocity according to equation (3-5). Similarly, the V(z,t) plots from other commercial and additive manufactured materials are presented in Fig. (3-7).

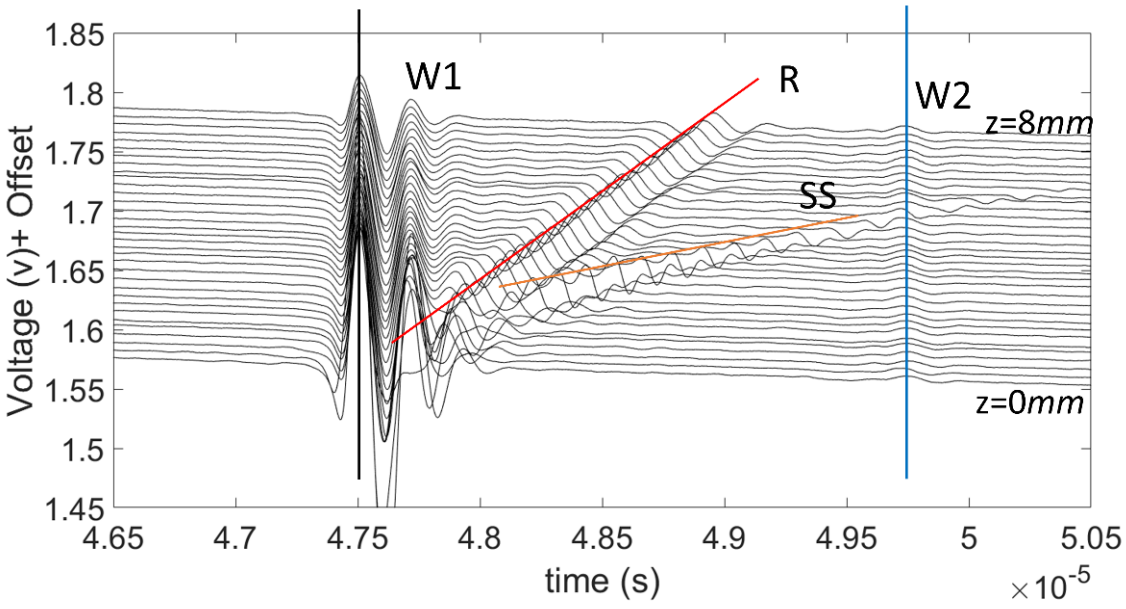
W1
R
W2
SS
z=8mm
z=0mm
Voltage (v)+ Offset
time (s)
×10^-5

(a)

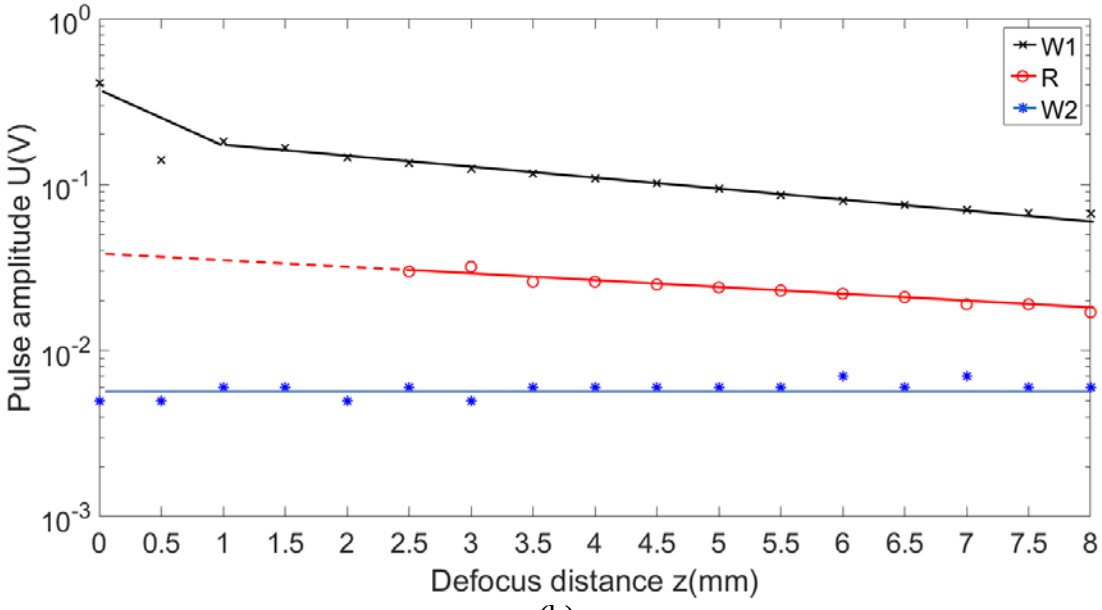
W1
R
W2
Pulse amplitude U(V)
Defocus distance z(mm)

(b)

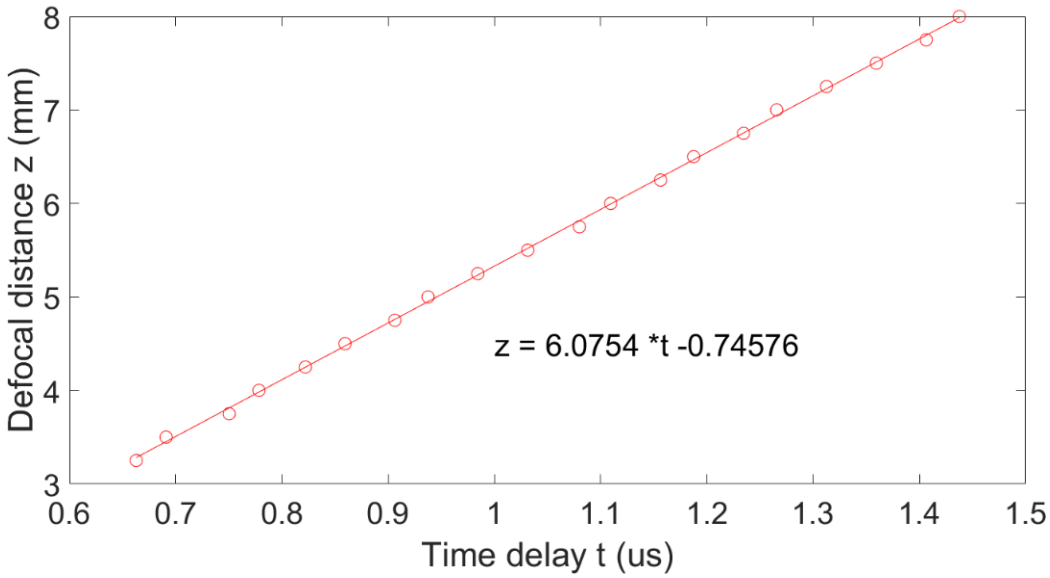

(c)

Figure 3-6 Additive manufactured SS416 (a) $V(z,t)$ **waveforms (b) Pulse amplitude vs z (c) Z(t) plot**

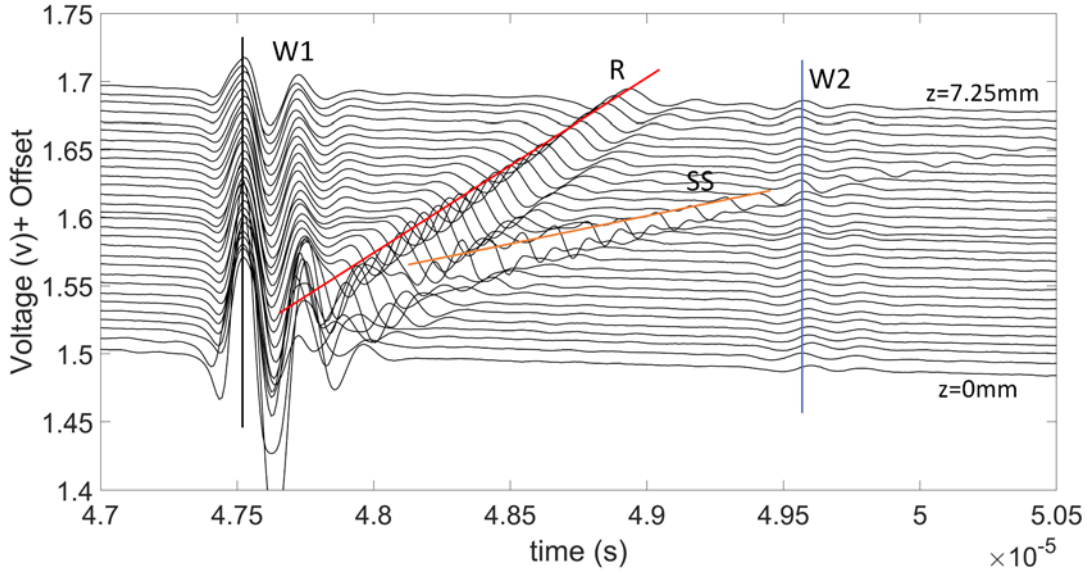

(a)

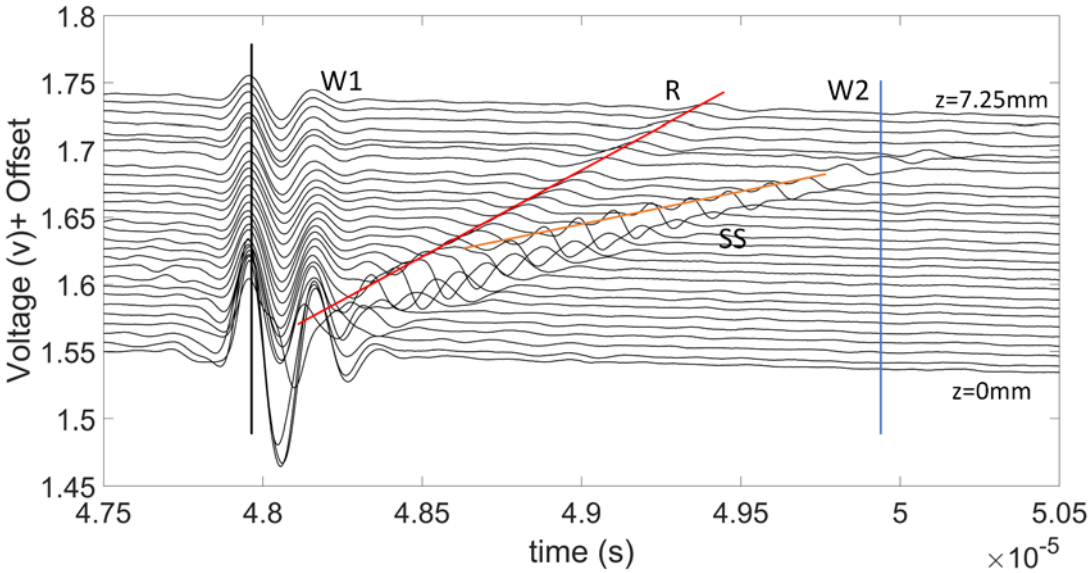

(b)

Figure 3-7 V(z,t) of (a) Commercial Aluminum alloy 6061 (b) Additive manufactured IN625

3.3.2 Evaluation of Material Anisotropy

Metal alloys fabricated by traditional casting method are modeled as isotropic materials in macroscale, and the material property is independent of the orientation of the sample being tested.

Whereas, the metal alloy built by additive manufacturing can show some anisotropy due to the strong directional character of the fabrication process. The coordinates used in machines using laser sintering and binder jet technology is Cartesian coordinate system (shown in Fig. 3-8) where building tray is placed on the XY plane and moves downward along Z direction as build layers are continuously stacked on top of layers. XY plane is the construction plane, where the laser (of laser sintering) or the printhead (of binder jet) can move interpedently on X or Y direction to melt or bind the metal powder on selected positions based on the building pattern programmed by the control system. Specifically, laser sintering method focuses the laser as a straight line on building plane to melt and cure metal; and binder jet method aligns a series of printhead to drop binding material in a line on building plane. In this study, for the discussion convenience, X direction refers to the laser or printhead alignment direction (shown as the stripe direction of the filled pattern in Fig. 3-8) and Y direction refers to the moving direction of laser and printhead which is orthogonal to X as presented in Fig. 3-8. If any anisotropy is introduced in the material due to the manufacturing direction, the property is expected to exhibit the most distinction between X and Y directions. Therefore, the mechanical property will be analyzed and compared on these two directions for evaluating the degree of anisotropy.

As the wave velocities in the solid material along certain directions are determined by its properties, the Rayleigh surface wave velocities measured by the line focus ultrasound system and abovementioned reduction method are used to indicate the anisotropy. For comparison purpose, the Rayleigh surface wave is also generated on two orthogonal directions X and Y on the same plane of the test samples. To minimize random uncertainty in individual measurement, the V_R on specific directions of additive manufactured and commercial metal alloys are measured 6 times repeatedly on all three samples, and the averaged velocities are presented in Fig. 3-9. The random

error of V_R during the repeated measurements shows an overall less than 1.5% about the averaged velocities for both commercial and additive manufactured materials.

SS420, Al and Cu are the three commercial materials, and from Fig. 3-9, the averaged V_R between the two measurement directions shows a difference less than 1%, confirming the isotropy character of the commercial materials. For additive manufactured samples SS316, IN625, AlSi10Mg, Ti64 and IN718, the velocity from X direction is consistently higher than from Y direction by 2.5%, 3.1%, 2.7%, 1.8% and 0.3%, respectively. Such trend can be a consequence of directional fabrication procedure, where the continuity of laser strength and the amount of binder material is more consistent on the alignment direction (X) than the movement direction (Y). Therefore, on X direction, the material continuity is better and resulting higher acoustic propagation velocity. Still this influence on the velocity is very small considering the error are smaller than 3%. Therefore, although some degree of anisotropic character could be expected, particularly from some AM materials such as SS316, IN625, AlSi10Mg and Ti64, the influence on the material overall property could be still negligible for practical application and the elastic constant of those AM materials will be quantified based on the wave propagation theory of isotropic materials, whose mechanical property remains same regardless of the measurement direction on the material, in the following section.

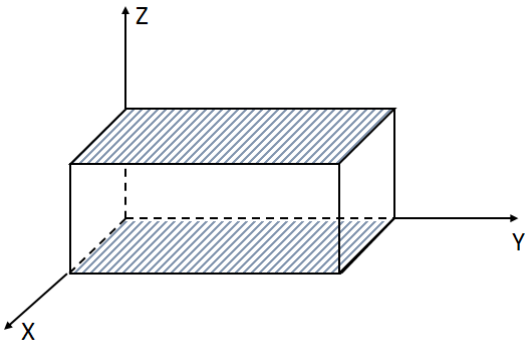

Figure 3-8 Fabrication directions by Additive Manufacturing

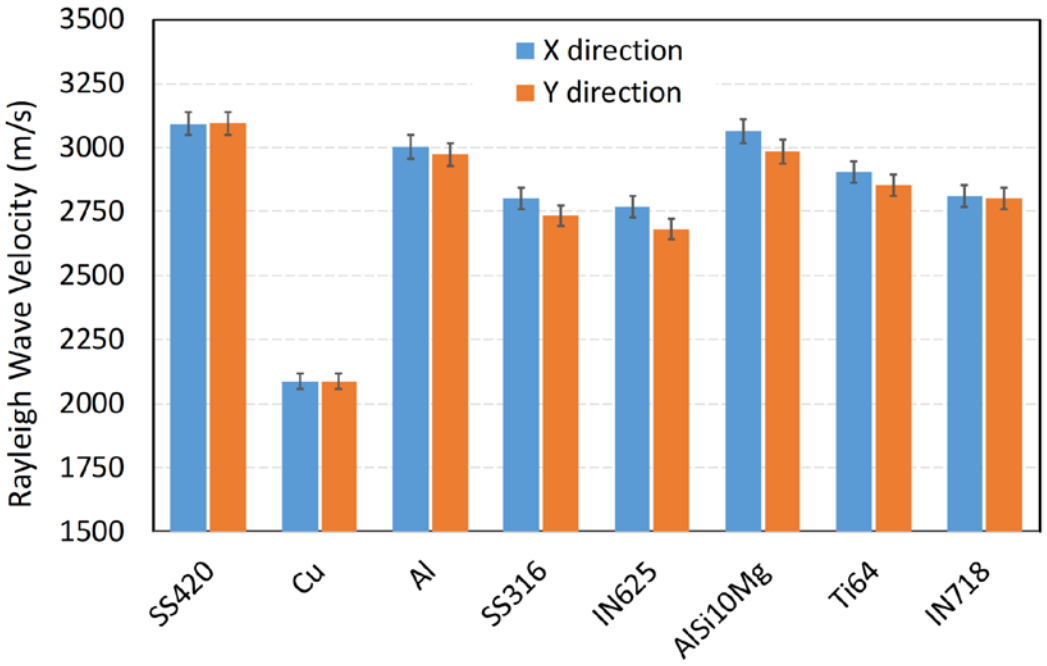

Figure 3-9 Rayleigh surface wave velocity measured from multiple directions of sample materials

3.3.3 Analysis of Surface Roughness of Test Samples

Surface roughness is an important factor which could affect the measurement results of surface wave velocity as the roughness will introduce extra gaps or discontinuity on the sold surface on which Rayleigh surface wave propagates. The surface roughness of the test samples,

described as R_a (the arithmetical mean of roughness profile), is measured with a surface profiler (Alpha-Step IQ, KLA-Tencor Instruments) and is presented in Table 3-1. The surface roughness of commercial material samples is very small with a magnitude of $0.1\mu m$, because such commercial products are subject to final polishing in the manufacturing process per standard. Whereas, the additive manufacture materials are directly 'built in machine' without any surface polishing, thus their surface is expected to be much coarser with R_a in magnitude of $10\mu m$. From Table 3-1, the measured R_a also shows good agreement with the reference value from official data sheet [35-39]. This means the surface roughness of the samples remains consistent on different fabrications and thus the measurement resutls from this study could be generally adopted for all samples made by the same fabrication instrument with the default building condition. Based on the measurement results in Fig. 3-9, the Rayleigh surface wave velocity (V_R) in the metals is in general around 3000 *m/s*. Considering the center frequency of the transducer is 8MHz (Fig. 3-5) and thus the wave propagation frequency (*f*) is estimated as 8MHz, the wavelength of the Rayleigh surface waves can be estimated to be about $375\mu m$ given $\lambda_R = V_R / f$. Since the surface roughness is two orders of magnitude smaller than the wave length, its impact is expected to be very negligible on the wave propagation and velocity measurement. Therefore, the additive manufactured samples without any surface polishing treatment can be directly used for the material property evaluation by measuring Rayleigh surface wave velocity.

Table 3-1 Sample Surface Roughness

Fabrication Method	Material	Surface Roughness R_a (μm)	
		Measured	Reference
Commercial	SS420	0.23	---
	Aluminum	0.34	---
	Copper	0.32	---
Additive Manufacture	SS316L	14	15 [38]
	IN 625	7	10 [39]
	AlSi10Mg	6.5	6-10 [35]
	IN718	4.5	4-6.5 [36]
	Ti64	9.5	5-9 [37]

3.3.4 **Material Elastic Constant Characterization & Sensitivity Analysis**

Analysis in previous sections demonstrate that the anisotropy character and possible influence of surface roughness can be ignored on those metal samples fabricated by AM method, and therefore the wave velocities measured by the single line-focus transducer can be further used to characterize elastic constants of the materials based on the wave propagating theory of isotropic materials. Additionally, the elastic constants based on line focus ultrasound testing can be compared to the corresponding reference parameters from the official datasheet to evaluate the measurement accuracy of this ultrasound method.

For isotropic solid, the velocity of Rayleigh surface wave (V_R) can be expressed in terms of longitudinal bulk wave velocity (V_L) and transverse bulk wave velocity (V_T) [40]:

$$V_R = V_T \frac{0.718 - \left(\frac{V_T}{c_L}\right)^2}{0.75 - \left(\frac{V_T}{c_L}\right)^2} \quad \textbf{(3-7)}$$

(3-7) can be rewrite in the polynomial equation format

$$\left(\frac{V_T}{V_L}\right)^3-\left(\frac{V_R}{V_L}\right)\left(\frac{V_T}{c_L}\right)^2-0.718\left(\frac{V_T}{V_L}\right)+0.75\left(\frac{V_R}{V_L}\right)=0 \quad \textbf{(3-8)}$$

When V_R and V_L is given, equation (3-7) becomes a third order polynomial about V_T, which can be directly solved. Studies show that there is only one acceptable solution that satisfies $(V_T/V_L)<1/\sqrt{2}$ according to the bulk wave propagation character in isotropic solid [28].

The mechanical property of isotropic solid is described using elastic constants such as Young's modulus, Poison ratio, and shear modulus. Based on the bulk wave propagation theory in solid, the elastic constants can be calculated using the longitudinal and transverse bulk wave velocities with given velocity equations which had been extensively studied. Therefore, once the density of the materials (ρ) is measured, the elastic constants of the material can be calculated [28]:

$$E=\rho V_T^2\frac{3V_L^2-4V_T^2}{V_L^2-V_T^2} \quad \textbf{(3-9)}$$

$$G=\rho V_T^2 \quad \textbf{(3-10)}$$

$$\nu=\frac{2V_T^2-V_L^2}{2\left(V_T^2-V_L^2\right)} \quad \textbf{(3-11)}$$

where *E* is Young's modulus, *G* is shear modulus and *v* is Poisson's ratio.

The densities of metals are obtained by measuring the mass with a digital scale and measuring volume using graduated cylinder with accuracy as $0.0001g$ and $0.1mm^3$ correspondingly. The measured densities, together with the measured V_R and V_L are summarized in Table 3-2 and Table 3-3. Based on the measured V_R and V_L, the V_S is calculated using equation (3-8), and the elastic constants are then obtained. As the elastic constants are characterized by the

manufacturing company with traditional tensile testing methods, they are used as a reference standard with which the results based on line focus ultrasound system is compared, so that the measurement accuracy of this system can be evaluated.

For commercial metals (Table 3-2), the difference of the measurement vs reference values (in parenthesis) from official datasheet for SS420, Aluminum and Copper are -1.9%, 1.6%, and 0.0002%, so ±2% can be used as standard uncertainty for density. Similar for elastic constants, the overall uncertainty is ±7% for E and G, and ν. These uncertainty level will be used as a standard to evaluate if the measured parameters match the reference values with good accuracy for AM fabricated materials.

Table 3-2 Elastic constants of commercial metal alloys

Material	Rayleigh Critical Angle θ_R	Mass Density ρ (kg/m^3)	Measured Velocities			Elastic Constants		
			Rayleigh Surface Wave Velocity V_R (m/s)	Bulk Longitudinal Wave Velocity V_L (m/s)	Bulk Transverse Wave Velocity V_T (m/s)	Young's Modulus E (GPa)	Poison Ratio ν	Shear Modulus G (GPa)
Stainless Steel 420	29º	7649 (7800)	3093.82	5969.8	3344.87	213 (200)	0.27 (0.3)	83.9 (79.3)
Aluminum	30º	2743 (2700)	2988.19	6147.9	3209.24	73 (69)	0.31 (0.33)	27.1 (25.5)
Copper	45º	8928 (8930)	2086.76	4585.2	2221.99	118 (117)	0.34 (0.335)	44.1 (44.7)

*The values in parenthesis are standard density and elastic constants reference from material datasheet [41].

The ultrasound system is further applied to characterization of elastic constants of materials fabricated by additive manufacturing method. The measurement and calculation results are summarized in Table 3-3. The results show that among the five types of test materials, the elastic

constants of IN725, AlSi10Mg, and Ti64 have very good agreement with reference data and the measurement error is within 3% and the density difference is less than 1%, both error sit within the uncertainty range (±7% for elastic constants and ±2% for density) from commercial materials. However, the *E* of SS316L made by binder-jet method show the highest error 10%. The error could be explained by unique qualities of test material caused by different fabrication procedure. SS316L sample in this study has a density about notably 8% lower than reference value. Such significant difference has two effects on elastic constant measurements. Firstly, lower density means higher porosity in the solid material and larger energy dissipation is expected for wave propagation, resulting in lower wave velocity measured in this study. Secondly, the elastic constant calculated according to equation (3-5) is linearly to material density. If the same density value is used, the elastic constant error is reduced as low as 2%. The Young's modulus of IN718 which is made by selective laser sintering method is 8% larger than the official data, which is relatively larger error comparing to other materials, but considering the 10% uncertainty [36] provided from manufacture, this error still stays in reasonable range.

Overall, irrespective with the possible variation on material property introduced by different fabrication methods, the line-focus ultrasound system demonstrates a reasonably good measurement accuracy in charactering material elastic constants. In addition, such validation/calibration work for the measurement method is a necessary step for further development and validation of the line focus system to evaluate anisotropic materials.

The elastic constants characterization shows that among the 7% uncertainty in E and G from commercial materials, 5% comes from the velocity measurement; for AM materials this uncertainty is 2%. Therefore, if the overall uncertainty of E from velocity measurement is taken as 5%, based on equations (8) and (9), the measurement uncertainty from V_R and V_L are required

to be within 22%, which is much larger than the actual uncertainty from the experiment (i.e. 1-3% from section 3.2). Therefore, the measurement accuracy of this line focus system using time domain analysis on Young's modulus and shear modulus evaluation is 0.1%.

Table 3-3 Elastic constants of alloy samples prepared by additive manufacturing

Material	Rayleigh Critical Angle θ_R	Mass Density ρ (kg/m^3)	Measured Velocities			Elastic Constants		
			Rayleigh Surface Wave Velocity V_R (m/s)	Bulk Longitudinal Wave Velocity V_L (m/s)	Bulk Transverse Wave Velocity V_T (m/s)	Young's Modulus E (GPa)	Poison Ratio ν	Shear Modulus G (GPa)
Stainless Steel 316L	32º	7279 (7900)	2796.9	5433.1	3015.36	167.25 (186)	0.277 (0.27)	65.46
IN 625	32º	8355 (8350)	2763.7	5238.1	2988.86	187.88 (193)	0.259 (0.3)	73.63
AlSi10Mg	29º	2672 (2670)	3021.9	6702.3	3220.4	74.82 (75)	0.35	27.71
Ti64	31º	4437 (4410)	2872.8	6258.8	3065.1	111.9 (110)	0.34	41.68
IN 718	32º	8158 (8150)	2811.3	5911.1	3007.2	195.56 (180)	0.33	73.77

*The density and elastic constants shown in parenthesis are the available reference values from official data sheet of the materials: Stainless Steel 316L[38], IN 625[39], AlSi10Mg[35], Ti64[37], IN718[36].

3.4 Discussions

In this study, a PVDF line focus ultrasound transducer was fabricated and its application on elastic constants characterization of metal alloys built by additive manufacture technology was calibrated. The calibration assumes that the surface wave generated on the solid sample is in

Rayleigh mode, which requires the testing sample is one order of magnitude higher than the wavelength of Rayleigh surface wave. As the center frequency of the transducer is 8MHz, and most metal alloys have a surface wave velocity about 3000m/s, the wavelength of Rayleigh surface wave in metal alloys is about 370μm. Considering that test sample has 5 mm thickness, the assumption of surface wave propagation in Rayleigh mode is valid. If test sample is much thinner, saying 1 mm thick, then a much higher frequency transducer needs to be used to generate Rayleigh wave with much smaller wave length than the sample thickness. Meantime, the influence from surface roughness of the unpolished test samples can be ignored because the wavelength 370μm is an order of magnitude higher than the surface roughness (i.e. averaged 10μm from Table 3-1). Therefore, the testing samples built by additive manufacture can be directly put into testing without extra surface polish, which makes the testing method eligible for convenient on-site material quality monitoring in field.

This study is the first step to develop an elastic constants characterization method for isotropic and anisotropic materials, which is based on the velocities of Rayleigh surface wave and longitudinal bulk wave measured by single line-focus transducer. By using the time domain analysis on the voltage response of the transducer, both Rayleigh surface wave and longitudinal bulk wave velocities of testing materials are obtained, which enables the characterization of the two independent elastic constants of isotropic materials be achieved with single transducer through one testing process, which is not possible for neither traditional ultrasound method nor the V(z) curve method, which both require two types of transducers to measure the two velocities, because the traditional transducer only generates one specific type of wave (i.e. either longitudinal or transverse wave), and V(z) curve method lose the longitudinal wave information during the signal processing although it also uses line focus transducer. Therefore, it will simplify the elastic

constant characterization procedure for anisotropic materials who have higher number of independent elastic constants and require more velocity measured. In future study, the authors will conduct analytical study on surface wave propagating in true anisotropic materials, such as cubic and trigonal crystals, to derive the relationship between surface wave velocity and elastic constants, so that the line focus ultrasound system can be used as a novel material property characterization method.

3.5 Summary

Elastic constants of metal alloy have been measured nondestructively by using line-focus ultrasound system. It has been proved that both Rayleigh surface wave and longitudinal bulk wave can be generated on solid samples using single line-focus transducer, and the wave velocities can be measured using time-resolved defocusing method with $V(t,z)$ waveforms which is a collection of directly received waveforms from transducer at different focal positions. The elastic constants of metal made by casting method and two additive manufacturing methods are calculated from the measured velocities. The results show very good agreement with values obtained from material datasheets which are obtained from tensile testing method. This proves that this non-destructive experiment method using line-focus ultrasound system and time-resolved defocusing data analysis approach is accurate and efficient in determining the elastic constants of isotropic solid materials built by additive manufacturing method, providing a new promising method to evaluate material mechanical property.

4.0 Cubic Material

This chapter proposes a novel stiffness constant characterization method for anisotropic cubic materials based on acoustic wave propagation. The theoretical study based on fundamental wave propagation equations is first conducted to develop the mechanistic model that describes Rayleigh surface wave propagation as a function of stiffness constants and then the model is validated experimentally using single crystal silicon as an example. Based on the validated mechanistic model, the novel approach to characterize stiffness constants of anisotropic cubic material is proposed based on the simultaneous measurements of Rayleigh surface wave and longitudinal bulk wave realized by a lens-less line-focus transducer. Two different modes of surface waves, regular and pseudo, are also investigated. As a potential better alternative to traditional methods which is only based on bulk wave and therefore requires two or more step measurements, this new method has simplified test procedure and reduced sample usage/preparation for full characterization of stiff constants. The stiff constants of test sample predicted by the new method demonstrates a very good agreement of less 6% difference with reference value from literature. In addition, two different approaches are also discussed and evaluated depending on the combinations of different types of velocity measurements.

4.1 Mechanistic Model Development

Considering the propagation of the elastic wave in infinite anisotropic continuous homogeneous solid, the wave arises from particle localized displacements. The displacement u_i

of arbitrary point in the solid is in a function of coordinates (x_k) and time (t) as $u_i = u_i(x_k, t)$. Given the mass density of the solid ρ, the general wave equation is

$$\rho \frac{\partial^2 u_i}{\partial t^2} = c'_{ijkl} \frac{\partial^2 u_l}{\partial x_j \partial x_k} \quad (i, j, k, l = 1, 2, 3) \tag{4-1}$$

where the tensor c'_{ijkl} is related to material stiffness tensor c_{pqrs}, and c'_{ijkl} is equal to c_{pqrs} when the wave propagation coordinates (x_1, x_2, x_3) coincides with crystallographic coordinates (X, Y, Z).

For surface waves, the stress-free boundary condition must be satisfied. Different modes of surface wave arise when different boundary conditions are applied. For Rayleigh type surface wave, the solid is considered as semi-infinite plane [1], so the thickness of the solid must be larger than the wavelength such that the wave that propagates near one surface is not influenced by the reflection from the other side of the sample surface. In addition, the decay of surface wave magnitude in the thickness direction shouldn't be ignored as the surface wave cannot propagate deep into this direction.

Considering the surface wave propagates on (x_1, x_3) plane along direction $\mathbf{n}$, where $n_1 = \sin\varphi, n_2 = 0, n_3 = \cos\varphi$ as shown in Fig. 4-1, based on the theory of wave propagation [1], the general particle polarization displacement u_l is assumed in the format:

$$u_l = U_r(x_2) \exp\left(ik\left(Vt - n_1 x_1 - n_3 x_3\right)\right) \tag{4-2}$$

Where the decay term $U_r(x_2)$ can be specified as $U_r(x_2) = \left(\sum_{r=1}^{3} A_r \circ u_l \exp(-ikq_r x_2)\right)$ in which A_r is the amplitude, $\circ u_l$ is the components of polarization vector, and q_r is the decay constants. And in the sinusoidal wave term, V is the propagating phase velocity, and k is the wavenumber. The

plane of contains propagating direction $\mathbf{n}$ and surface normal $\mathbf{x_2}$ is often called sagittal plane. For cubic crystals, when wave propagates on cubic axis X, Y or Z, the wave polarization is on sagittal plane [1].

Substitute (4-2) into (4-1), the differential equation (4-1) is transformed to a polynomial equation called Christoffel equation given as

$$\left(\Gamma_{il} - \rho V^2 \delta_{il}\right) \circ u_i = 0 \qquad \textbf{(4-3)}$$

Where the Christoffel tensor is

$$\Gamma_{il} = c'_{i11l}\, n_1^2 + c'_{i22l}\, q_r^2 + c'_{i33l}\, n_3^2 + \left(c'_{i12l} + c'_{i21l}\right) n_1 q_r + \left(c'_{i23l} + c'_{i32l}\right) n_3 q_r + \left(c'_{i13l} + c'_{i31l}\right) n_1 n_3$$

And at $x_2 = 0$, the stress-free boundary condition gives

$$\begin{aligned} T_2 = T_{22} &= c'_{22kl} \frac{\partial u_l}{\partial x_k} = 0 \\ T_4 = T_{32} &= c'_{32kl} \frac{\partial u_l}{\partial x_k} = 0 \qquad \textbf{at } x_2 = 0 \\ T_6 = T_{12} &= c'_{12kl} \frac{\partial u_l}{\partial x_k} = 0 \end{aligned} \qquad \textbf{(4-4)}$$

The following subsections presented the analytical analysis on Rayleigh surface waves propagating on (100) and (110) planes. Velocity equations are derived to describe the relationship between wave phase velocity and stiffness constants. The directions and structure of cubic crystal are shown in Fig. 4-2.

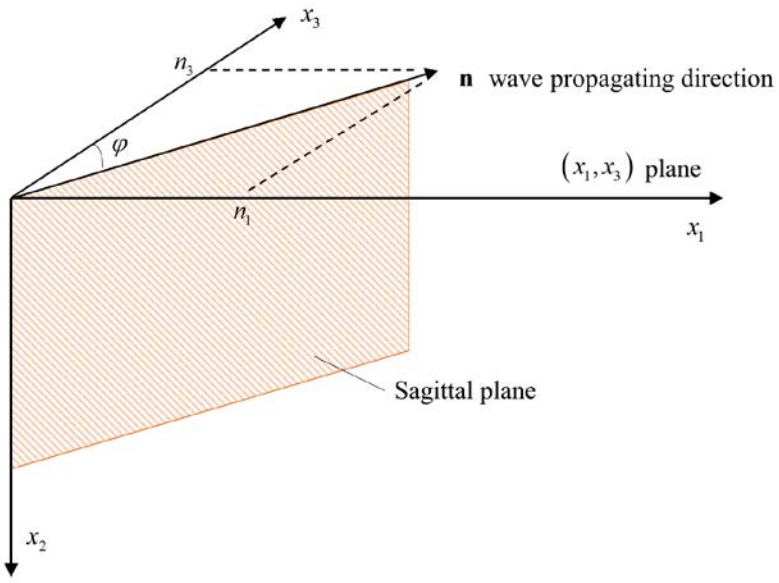

Figure 4-1 Wave propagation coordinate system

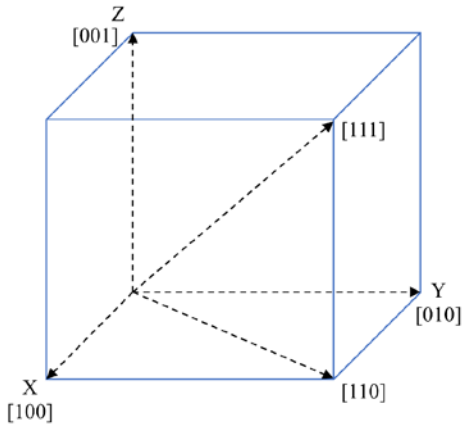

Figure 4-2 Cubic crystal crystallographic coordinate system and critical directions

4.1.1 **(1 0 0) Plane**

For the surface wave propagating along the face of a cubic crystal, the tensor c'_{ijkl} is equal to the stiffness tensor c_{pqrs}.

$$\left(c_{\alpha\beta}\right)=\left(c_{pqrs}\right)=\begin{pmatrix} c_{11} & c_{12} & c_{12} & 0 & 0 & 0 \\ c_{12} & c_{11} & c_{12} & 0 & 0 & 0 \\ c_{12} & c_{12} & c_{11} & 0 & 0 & 0 \\ 0 & 0 & 0 & c_{66} & 0 & 0 \\ 0 & 0 & 0 & 0 & c_{66} & 0 \\ 0 & 0 & 0 & 0 & 0 & c_{66} \end{pmatrix}$$

Substitute this stiffness tensor in (4-3) to have a simplified Christoffel equation:

$$\begin{pmatrix} \Gamma_{11}-\zeta & \Gamma_{12} & \Gamma_{13} \\ \Gamma_{12} & \Gamma_{22}-\zeta & \Gamma_{23} \\ \Gamma_{13} & \Gamma_{23} & \Gamma_{33}-\zeta \end{pmatrix}\begin{pmatrix} {}^{\circ}u_1 \\ {}^{\circ}u_2 \\ {}^{\circ}u_3 \end{pmatrix}=0 \qquad \textbf{(4-5)}$$

And the Christoffel's Matrix Γ_{il} has the non-zero components:

$$\begin{aligned} \Gamma_{11} &= c_{11}n_1^2+c_{66}q_r^2+c_{66}n_3^2 & \Gamma_{12} &= \left(c_{12}+c_{66}\right)\left(n_1q_r\right) \\ \Gamma_{22} &= c_{66}n_1^2+c_{11}q_r^2+c_{66}n_3^2 & \Gamma_{13} &= \left(c_{12}+c_{66}\right)\left(n_1n_3\right) \\ \Gamma_{33} &= c_{66}n_1^2+c_{66}q_r^2+c_{11}n_3^2 & \Gamma_{23} &= \left(c_{12}+c_{66}\right)\left(n_3q_r\right) \end{aligned} \qquad \textbf{(4-6)}$$

Therefore, the secular equation is

$$\det\left(\Gamma_{il}-\delta_{il}\zeta\right)=0 \qquad \textbf{(4-7)}$$

$\zeta=\rho V_R{}^2$ is the eigenvector of Γ_{il}. Chose eigenvector of Γ_{il}

$$\begin{pmatrix} {}^{\circ}u_1^{(r)} \\ {}^{\circ}u_2^{(r)} \\ {}^{\circ}u_3^{(r)} \end{pmatrix}=\begin{pmatrix} p_r \\ s_r \\ 1 \end{pmatrix} \quad \textbf{where } (r=1,2,3)\textbf{, with} \quad \begin{aligned} p_r &= \frac{\Gamma_{12}\left(\Gamma_{33}-\zeta\right)-\Gamma_{13}\Gamma_{23}}{\Gamma_{23}\left(\Gamma_{11}-\zeta\right)-\Gamma_{12}\Gamma_{23}} \\ s_r &= \frac{\left(\Gamma_{11}-\zeta\right)\left(\Gamma_{33}-\zeta\right)-\Gamma_{13}^2}{\Gamma_{12}\Gamma_{13}-\Gamma_{23}\left(\Gamma_{11}-\zeta\right)} \end{aligned} \qquad \textbf{(4-8)}$$

Then, substitute the eigenvector $\begin{pmatrix} p_r & s_r & 1 \end{pmatrix}^T$ in general solution (4-2) and then substitute into (4-4) that the boundary condition can be written as

$$\begin{pmatrix} \Lambda_{11} & \Lambda_{12} & \Lambda_{13} \\ \Lambda_{21} & \Lambda_{22} & \Lambda_{23} \\ \Lambda_{31} & \Lambda_{32} & \Lambda_{33} \end{pmatrix} \begin{pmatrix} A_1 \\ A_2 \\ A_3 \end{pmatrix} = 0 \tag{4-9}$$

Where the matrix $\mathbf{\Lambda}$ is given as

$$\begin{array}{lll} \Lambda_{11} = c_{12}n_1p_1 + c_{13}n_3 + c_{22}q_1s_1 & \Lambda_{12} = c_{12}n_1p_2 + c_{13}n_3 + c_{22}q_2s_2 & \Lambda_{13} = c_{12}n_1p_3 + c_{13}n_3 + c_{22}q_3s_3 \\ \Lambda_{21} = c_{66}\left(n_3s_1 + q_1\right) & \Lambda_{22} = c_{66}\left(n_3s_2 + q_2\right) & \Lambda_{23} = c_{66}\left(n_3s_3 + q_3\right) \\ \Lambda_{31} = c_{66}\left(q_1p_1 + n_1s_1\right) & \Lambda_{32} = c_{66}\left(q_2p_2 + n_1s_2\right) & \Lambda_{33} = c_{66}\left(q_3p_3 + n_1s_3\right) \end{array} \tag{4-10}$$

The secular equation for matrix $\mathbf{\Lambda}$ must be satisfied so that the boundary condition is satisfied:

$$\det\left(\Lambda_{ij}\right) = 0 \tag{4-11}$$

For the special case that the surface wave propagates on **[100] direction** given $n_1 = 1$ and $n_3 = 0$, such that $\Gamma_{13} = \Gamma_{23} = 0$, the Christoffel's equation can further be simplified as:

$$\begin{pmatrix} \Gamma_{11} - \zeta & \Gamma_{12} \\ \Gamma_{12} & \Gamma_{22} - \zeta \end{pmatrix} \begin{pmatrix} {}^{\circ}u_1 \\ {}^{\circ}u_2 \end{pmatrix} = \begin{pmatrix} 0 \\ 0 \end{pmatrix} \tag{4-12}$$

Where $\zeta = \rho V_{R[100]}^2$; $\Gamma_{11} = c_{11} + c_{66}q^2$; $\Gamma_{22} = c_{66} + c_{11}q^2$; $\Gamma_{12} = \left(c_{12} + c_{66}\right)q$

The characteristic equation is:

$$\left(c_{11} + c_{66}q^2 - \zeta\right)\left(c_{66} + c_{11}q^2 - \zeta\right) - \left(c_{12} + c_{66}\right)^2 q^2 = 0 \tag{4-13}$$

Which can be reorganized as:

$$q^4 - Sq^2 + P = 0 \tag{4-14}$$

Where

$$\begin{aligned} S &= q_1^2 + q_2^2 = \frac{c_{11}^2 - c_{22}^2 - \left(c_{11} + c_{66}\right)\zeta - 2c_{12}c_{66}}{c_{11}c_{66}} \\ P &= q_1^2 q_2^2 = \frac{\left(c_{11} - \zeta\right)\left(c_{66} - \zeta\right)}{c_{11}c_{66}} \end{aligned} \tag{4-15}$$

Taking eigenvector as $^{\circ}u_1^{(r)} = 1, ^{\circ}u_2^{(r)} = p_r, ^{\circ}u_3^{(r)} = 0$, Where $p_r = \frac{\zeta - c_{11} - c_{66}q_r^2}{(c_{12} + c_{66})q_r}$ for $r = 1,2$. From (4-9) and (4-10), the boundary condition is given as

$$\begin{aligned} (p_1 + q_1)A_1 + (p_2 + q_2)A_2 = 0 \\ (c_{12} + c_{11}p_1q_1)A_1 + (c_{12} + c_{11}p_2q_2)A_2 = 0 \end{aligned} \quad \textbf{(4-16)}$$

For non-trivial A_1 and A_2, the secular equation from boundary condition is given as:

$$(p_1 + q_1)(c_{12} + c_{11}p_2q_2) - (p_2 + q_2)(c_{12} + c_{11}p_2q_2) = 0 \quad \textbf{(4-17)}$$

which gives

$$q_1q_2 = -\frac{\zeta(c_{11} - \zeta)}{c_{11}^2 - c_{12}^2 - \zeta} \quad \textbf{(4-18)}$$

Since from (4-15):

$$q_1^2q_2^2 = \frac{(c_{11} - \zeta)(c_{66} - \zeta)}{c_{11}c_{66}} \quad \textbf{(4-19)}$$

As (4-18)^2= (4-19)

written in explicit form as:

$$c_{66}(c_{11} - \zeta)\zeta^2 - c_{11}(c_{66} - \zeta)\left(c_{11} - \frac{c_{12}^2}{c_{11}} - \zeta\right)^2 = 0 \quad \textbf{(4-20)}$$

Where $\zeta = \rho V_{R[100]}^2$.

4.1.2 **(1 1 0) Plane**

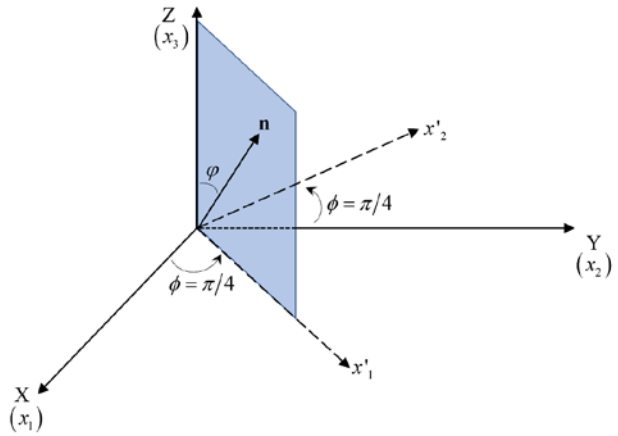

Figure 4-3 New Coordinate axes for wave propagate in diagonal plane (110)

For the surface wave propagating on the diagonal plane (i.e. (110) plane) of a cubic crystal, the tensor c'_{ijkl} is obtained from the stiffness tensor c_{pqrs} by transformation matrix $\boldsymbol{\alpha}$ by $c'_{ijkl} = \alpha_i^p \alpha_j^q \alpha_k^r \alpha_l^s c_{pqrs}$ [1], where for (110) plane, the transformation is presented in Fig. 4-3. given

$$\boldsymbol{\alpha} = \begin{pmatrix} \alpha_1^1 & \alpha_1^2 & \alpha_1^3 \\ \alpha_2^1 & \alpha_2^2 & \alpha_2^3 \\ \alpha_3^1 & \alpha_3^2 & \alpha_3^3 \end{pmatrix} = \begin{pmatrix} \cos\phi & \sin\phi & 0 \\ -\sin\phi & \cos\phi & 0 \\ 0 & 0 & 1 \end{pmatrix} = \begin{pmatrix} 1/\sqrt{2} & 1/\sqrt{2} & 0 \\ -1/\sqrt{2} & 1/\sqrt{2} & 0 \\ 0 & 0 & 1 \end{pmatrix} \tag{4-21}$$

So that the new tensor c'_{ijkl} is given as

$$\left(c'_{ijkl}\right) = \begin{pmatrix} c'_{11} & c'_{12} & c'_{13} & 0 & 0 & 0 \\ c'_{12} & c'_{11} & c'_{13} & 0 & 0 & 0 \\ c'_{13} & c'_{13} & c'_{33} & 0 & 0 & 0 \\ 0 & 0 & 0 & c'_{44} & 0 & 0 \\ 0 & 0 & 0 & 0 & c'_{44} & 0 \\ 0 & 0 & 0 & 0 & 0 & c'_{66} \end{pmatrix} \quad \text{with} \quad \begin{aligned} c'_{11} &= (c_{11} + c_{12})/2 + c_{66} \\ c'_{12} &= (c_{11} + c_{12})/2 - c_{66} \\ c'_{13} &= c_{12} \\ c'_{33} &= c_{11} \\ c'_{44} &= c_{66} \\ c'_{66} &= (c_{11} - c_{12})/2 \end{aligned} \tag{4-22}$$

The Christoffel's Matrix Γ_{ij} has the non-zero components:

$$\begin{aligned}
\Gamma_{11} &= c'_{11} n'^2_1 + c'_{66} q_r^2 + c'_{44} n'^2_3 & \Gamma_{12} &= \left(c'_{12} + c'_{66}\right) n'_1 q_r \\
\Gamma_{22} &= c'_{66} n'^2_1 + c'_{11} q_r^2 + c'_{44} n'^2_3 & \Gamma_{13} &= \left(c'_{13} + c'_{44}\right) n'_1 n'_3 \\
\Gamma_{33} &= c'_{44} n'^2_1 + c'_{44} q_r^2 + c'_{33} n'^2_3 & \Gamma_{23} &= \left(c'_{13} + c'_{44}\right) n'_3 q_r
\end{aligned} \qquad \textbf{(4-23)}$$

This gives the secular equation

$$\det\left(\Gamma_{il} - \delta_{il}\zeta\right) = 0 \qquad \textbf{(4-24)}$$

For the acceptable eigenvalues $q_r (r = 1,2,3)$ and assume the eigenvector has the same format with equation (8), then the mechanical boundary condition gives the secular equation:

$$\det\left(\Lambda_{ij}\right) = 0 \qquad \textbf{(4-25)}$$

Where the components of tensor $\mathbf{\Lambda}$ is given as

$$\begin{aligned}
\Lambda_{11} &= c'_{12} n'_1 p_1 + c'_{11} q_1 s_1 + c'_{13} n'_3 & \Lambda_{12} &= c'_{12} n'_1 p_2 + c'_{11} q_2 s_2 + c'_{13} n'_3 & \Lambda_{13} &= c'_{12} n'_1 p_3 + c'_{11} q_3 s_3 + c'_{13} n'_3 \\
\Lambda_{21} &= n'_3 s_1 + q_1 & \Lambda_{22} &= n'_3 s_2 + q_2 & \Lambda_{23} &= n'_3 s_3 + q_3 \\
\Lambda_{31} &= p_1 q_1 + n'_1 s_1 & \Lambda_{32} &= p_2 q_2 + n'_1 s_2 & \Lambda_{33} &= p_3 q_3 + n'_1 s_3
\end{aligned}$$

For [111] direction, the direction vector has components $n'_1 = \sin 35.26^\circ$ and $n'_3 = \cos 35.26^\circ$. Consider the wave propagating on the **[110] direction** of a cubic crystal, that $n_1^{'} = 1$ and $n_3^{'} = 0$. The Christoffel equation can be simplified as:

$$\begin{pmatrix} \Gamma_{11} - \zeta & \Gamma_{12} \\ \Gamma_{12} & \Gamma_{22} - \zeta \end{pmatrix} \begin{pmatrix} {}^\circ u_1 \\ {}^\circ u_2 \end{pmatrix} = \begin{pmatrix} 0 \\ 0 \end{pmatrix} \qquad \textbf{(4-26)}$$

with $\zeta = \rho V^2_{R[110]}$; $\Gamma_{11} = c'_{11} + c'_{66} q^2$; $\Gamma_{22} = c'_{66} + c'_{11} q^2$; $\Gamma_{12} = (c'_{12} + c'_{66}) q$

The secular equation from Christoffel equation is

$$\left(c'_{11} + c'_{66} q^2 - \zeta\right)\left(c'_{66} + c'_{11} q^2 - \zeta\right) - \left(c'_{12} + c'_{66}\right)^2 q^2 = 0 \qquad \textbf{(4-27)}$$

And the secular equation from boundary condition is

$$\left(p_1 + q_1\right)\left(c'_{12} + c'_{11} p_2 q_2\right) - \left(p_2 + q_2\right)\left(c'_{12} + c'_{11} p_2 q_2\right) = 0 \qquad \textbf{(4-28)}$$

Similar with the case of propagation on (1 0 0) direction (20), combining (27) and (28) will generate

$$c_{66}^{'}\left(c_{11}^{'}-\zeta\right)\zeta^{2}-c_{11}^{'}\left(c_{66}^{'}-\zeta\right)\left(c_{11}^{'}-\frac{c_{12}^{'}}{c_{11}^{'}}-\zeta\right)^{2}=0 \qquad \textbf{(4-29)}$$

The form using stiffness constants is given as:

$$\left(c_{11}-c_{12}\right)\left(c-\zeta\right)\zeta^{2}-c(c_{11}-c_{12}-2\zeta)\left(\frac{b}{16c}-\zeta\right)^{2}=0 \qquad \textbf{(4-30)}$$

where $\zeta=\rho V_{R[110]}^{2}$, $c=\frac{1}{2}(c_{11}+c_{12})+c_{66}$, $b=(4c_{11}+3c_{12})(c_{12}+8c_{66})$.

4.2 Numerical Solution

The phase velocity of wave propagation in solid is derived through solving the Christoffel equation [1]. By transforming the wave equation to Christoffel equation, solving the partial differential equation is simplified as searching for eigenvalues and eigenvectors of Christoffel matrix. For the bulk waves in solid, Christoffel matrix is in terms of stiffness constants, and the wave propagation direction, thus the phase velocity in specific direction can be easily found [1]. However, for the surface wave, the searching process becomes complicated given to two factors. (i) the stress-free boundary condition according to equation (4-4); (ii) Based on equation (4-2), the decay of displacement in the thickness direction should be considered, which adds a decay constant into wave propagation equation as unknown variable that needs to be solved.

Based on the equations presented in the previous section, the phase velocity of Rayleigh surface wave propagating on (100) or (110) cubic planes can be solved through numerical iteration using both the secular equation from the Christoffel equation (F1) and secular equation from

boundary condition (F2). Both F1 and F2 are functions with respect to solid density (ρ), stiffness constants (c_{pqrs}), wave propagation direction ($\mathbf{n}$), phase velocity (V_R) and decay constant (q). The unknown variables would be V_R and q for problem solving velocity on specific direction of a given material. So F1 and F2 is a closed equation system.

The 'simplicity method' [24] is used as the searching algorithm. The velocity searching procedure is briefly summarized as follows. 1. Assume a wave velocity as an initial value to substitute into F1, making a hexic polynomial equations about decay constant q_r ; 2. Solve F1 about q_r to get six solutions in forms of three pairs of complex conjugates, but only those with negative imaginary part are meaningful considering that Rayleigh surface wave must decay along the thickness direction according to fundamental physics [24]; 3. The three solutions selected are substitute in to F2 and the velocity is found when $\det\left(\Lambda_{ij}\right)$ is closest to zero within preset convergent criterion.

There are many different free surfaces and directions of propagation for cubic solid, but it is neither practical nor necessary to calculate all cases. Thus, in this study, the calculation is focus on three typical directions of cubic structure (i.e. [100], [110] and [111] directions) by using equation (7) and (11) for [100] and equation (24) and (25) for [110] and [111] directions. The calculation results of single crystal silicon are summarized in Table 1.

Consider the special directions [100] and [110], the secular equations from Christoffel equation and boundary condition can be combined and then decay constant is eliminated to obtain one single velocity equation (i.e. equation (20) for [100] and (30) for [110]) that only have stiffness and velocity terms, and simply the velocity on this equation can be 'directly solved' without numerical iteration, and the results are also summarized in Table 1. The calculation results from

both methods show good agreement indicating that the equation (20) and (30) can be directly used for further calculation with less calculation effort in more practical cases.

Table 4-1 Velocity from calculation of Silicon

V_R (m/s)	Simplicity method	Direct solve
[100]	4920	4916
[110]	4491	4485
[111]	4995	----------

4.3 Experimental Model Validation

4.3.1 Material

Single crystal silicon is used for the experimental study in order to validate the developed model for surface wave propagation in anisotropic cubic material. As a typical material in *m3m* group of cubic structure, it is a good benchmark to evaluate the performance of the line-focus ultrasound system and time-resolved defocusing method, since the material is easily commercially accessible with stable material quality. This consistent property will help mitigate possible measurement uncertainty generated from quality variation of test material. In addition, the mechanical property of single crystal silicon has been examined in detail for decades in many open literatures [1], therefore providing reliable data as reference.

The customized single crystal silicon bulks (by University Wafers Inc., MD) with 50mm in diameter and 10mm thick are used for experiment measurement, and test samples consist of three different directional cuts: (100), (110) and (111), with corresponding primary flats on [110],

[100], and [110] directions respectively. Referring to the crystallographic coordinates in Fig. 4-2, the measurement directions for each cut of test samples are depicted in Fig. 4-4. The Rayleigh wave (V_R) and longitudinal bulk wave (V_L) velocities are both generated and measured by a line-focus ultrasound testing system. The V_L and V_R on [100], [110] and [111] directions are all measured to evaluate the measurement to full extent. Since velocities in certain directions such as V_R on [100] and [110] can be generated and measured from either of (100) and (110) sample cuts, the velocities from all accessible directions are measured to evaluate the propagation similarity and difference from different measurement planes. Using (100) cut sample, V_L on [100] and V_R on [100] and [110] are measured; V_L on [110] and V_R on [100], [110] and [111] are measured from (110) cut sample; and V_L on [111] is obtained from the (111) cut sample.

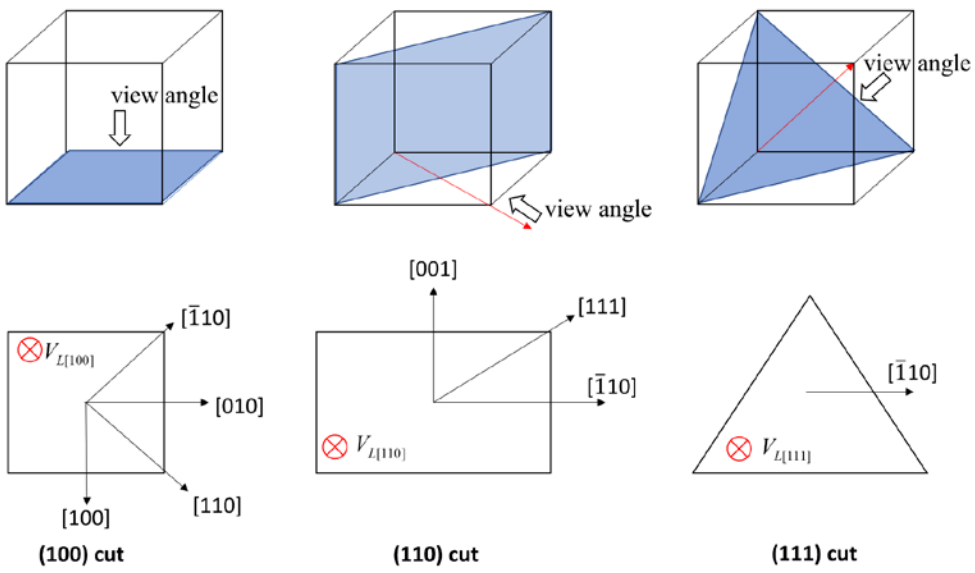

Figure 4-4 Diagram of directions of the testing samples (100) cut, (110) cut and (111) cut

Figure 4-5 The testing sample of (110) cut with primary flat on (100) direction

4.3.2 Results and Discussions

4.3.2.1 Longitudinal Bulk Wave

Table 4-2 compares the longitudinal bulk wave velocities on three different directions obtained in three different approaches. Specifically, the model prediction is calculated from stiffness constants measured from resonate method and theoretical equations for bulk wave velocity given by [1]; the experiment data is obtained by using the measured time delay t_L and equation (4-31), and the error in the parentheses (such as ±1%) represents the relative standard derivation from measurement in the line-focus ultrasound system established in this study; the reference value is from open literature which is based on traditional ultrasound testing method [1].

$$V_{L[100]} = \sqrt{c_{11}/\rho}\,,\ V_{L[110]} = \sqrt{\left(c_{11}+c_{12}+2c_{66}\right)/\left(2\rho\right)}\,,\ V_{L[111]} = \sqrt{\left(c_{11}+2c_{12}+4c_{66}\right)/\left(3\rho\right)}\,,$$

where the stiffness constants are $c_{11} = 16.56$, $c_{12} = 6.39$, and $c_{66} = 7.95$ (in $10^{10} N/m^2$), and mass density $\rho = 2329\,(kg/m^3)$ [1].

Overall, both experimental data and model prediction agree very well with reference data from open literature. This demonstrates that very good measurement accuracy can be obtained from the line-focus ultrasound experiment system. In addition, the velocity prediction has acceptable accuracy the model prediction based on stiffness constants measured from resonate method.

However, in order to characterize the three stiffness constants by velocity measurements, it is insufficient to only use these three longitudinal bulk waves. This is because the fact that the two velocity equations for $V_{L[110]}$ and $V_{L[111]}$ are two dependent equations about c_{12} and c_{66}. Thus, velocities of other mode such as transverse bulk wave or surface wave need to be used.

Table 4-2 Comparison of longitudinal bulk velocities obtained in different approaches

V_L	Model Prediction (m/s)	Experiment Data (m/s)	Reference Value [1]
[100]	8432	8442 (±1.1%)	8433
[110]	9132	9135 (±1.0%)	9134
[111]	9354	9369 (±1.0%)	9360

4.3.2.2 **Rayleigh Surface Wave**

Utilizing the same method as it is described in chapter 3, the V(z,t) curves are measured and the Z(t) plots are made, based on which the Rayleigh surface wave velocities are obtained.

The V(z,t) curves and Z(t) plots are shown in Fig. 4-6 and Fig. 4-7. Similar style of V(z,t) curves are found comparing to the ones of metal alloys.

Based on the symmetric structure of cubic crystal (Fig. 4-2) and geometric relationship from test samples with different cut directions (Fig. 4-4), the same Rayleigh surface wave can be measured in different directions at corresponding cut samples. For example, the Rayleigh surface wave velocity on [100] direction ($V_{R[100]}$) can be measured from [100] and [010] directions in (100) cut, or from [001] direction in (110) cut sample, whereas $V_{R[110]}$ can be measured from [110] and [10] directions on (100) cut, or from [110] direction on (110) cut. The averaged values of the same Rayleigh surface wave velocities are summarized in Fig. 4-8 with error bar representing the relative standard derivation from multiple measurements which is majorly caused by the uncertainty introduced from wave peak identification during multiple measurements.

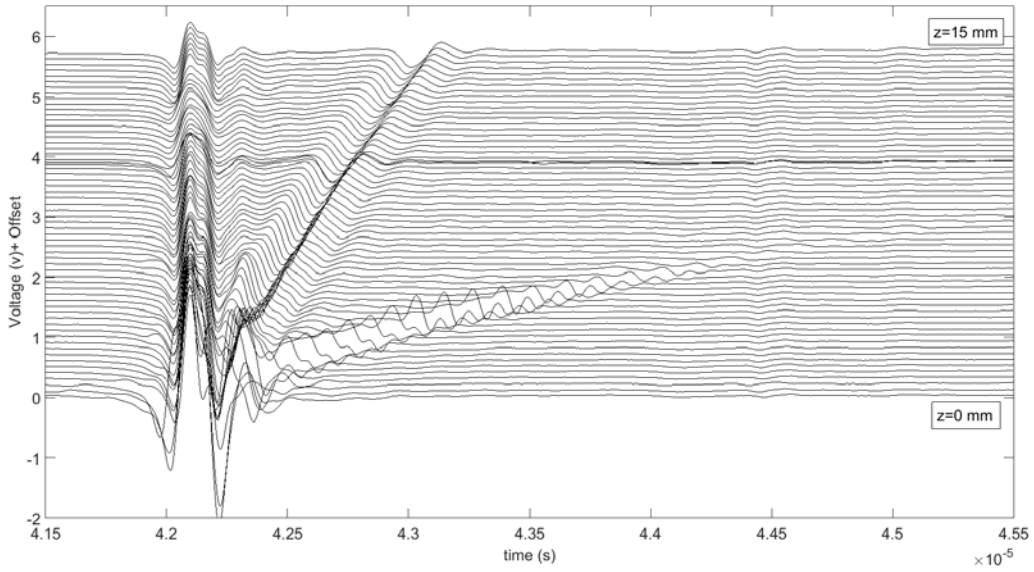

(a)

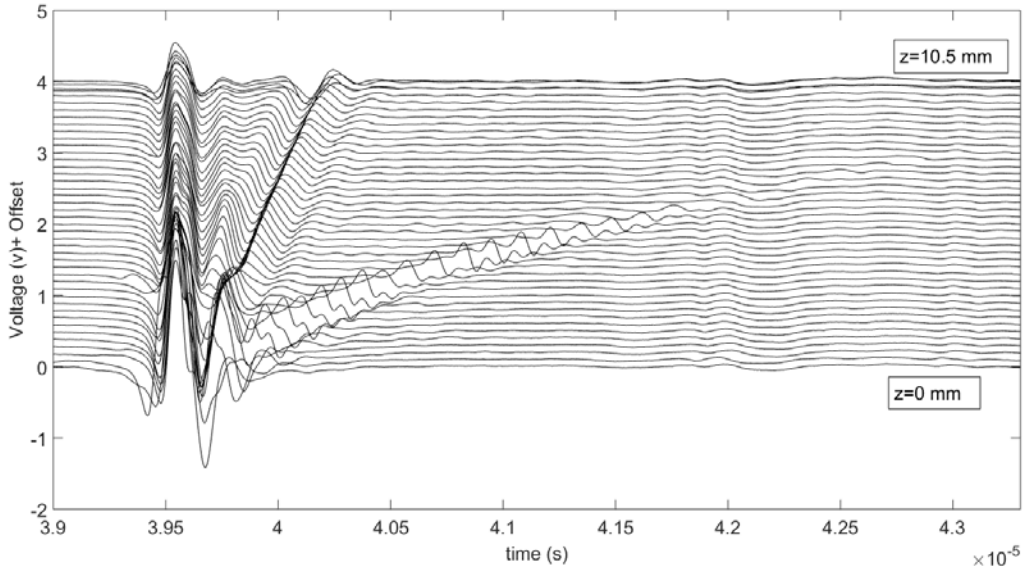

(b)

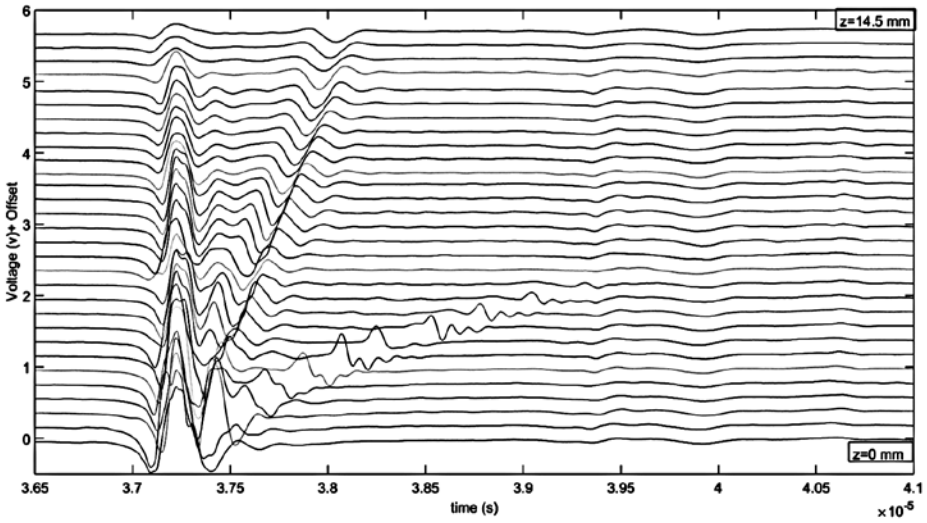

(c)

Figure 4-6 Examples of V(z,t) curves measured from (a) [100], (b) [110] and (c) [111] directions from Silicon sample

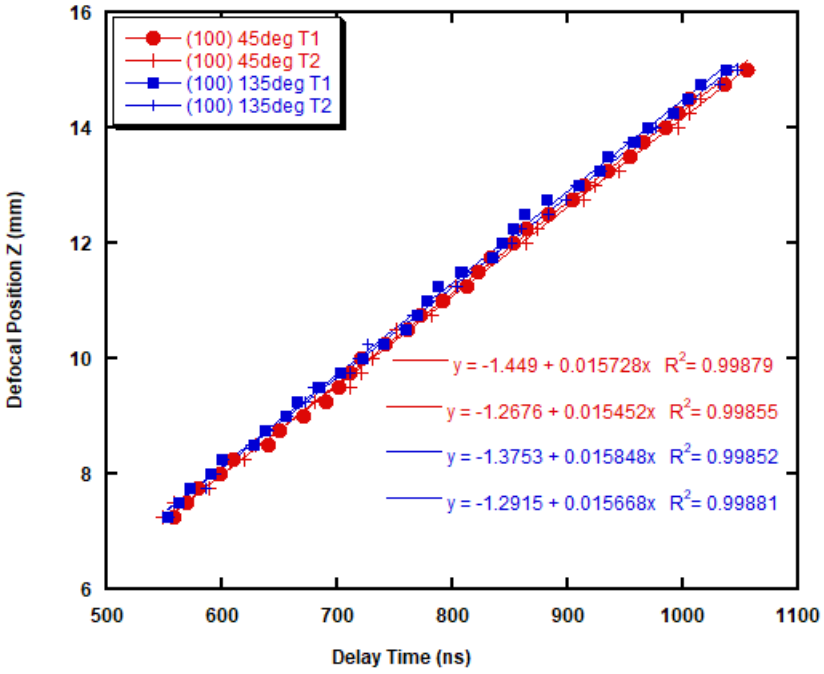
(100) 45deg T1
(100) 45deg T2
(100) 135deg T1
(100) 135deg T2
y = -1.449 + 0.015728x R²= 0.99879
y = -1.2676 + 0.015452x R²= 0.99855
y = -1.3753 + 0.015848x R²= 0.99852
y = -1.2915 + 0.015668x R²= 0.99881
Defocal Position Z (mm)
Delay Time (ns)
16
14
12
10
8
6
500
600
700
800
900
1000
1100

(a)

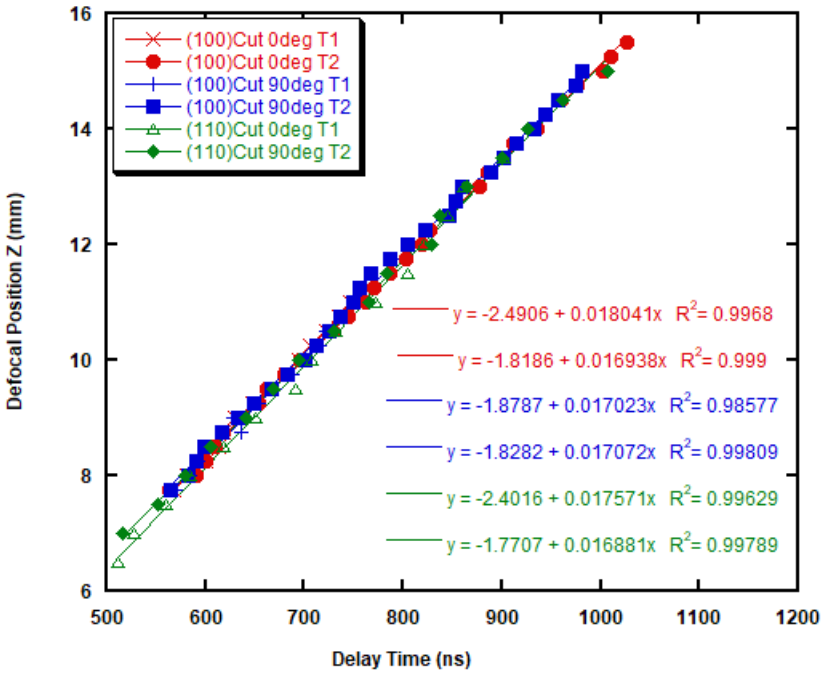
(100)Cut 0deg T1
(100)Cut 0deg T2
(100)Cut 90deg T1
(100)Cut 90deg T2
(110)Cut 0deg T1
(110)Cut 90deg T2
y = -2.4906 + 0.018041x R²= 0.9968
y = -1.8186 + 0.016938x R²= 0.999
y = -1.8787 + 0.017023x R²= 0.98577
y = -1.8282 + 0.017072x R²= 0.99809
y = -2.4016 + 0.017571x R²= 0.99629
y = -1.7707 + 0.016881x R²= 0.99789
Defocal Position Z (mm)
Delay Time (ns)
16
14
12
10
8
6
500
600
700
800
900
1000
1100
1200

(b)

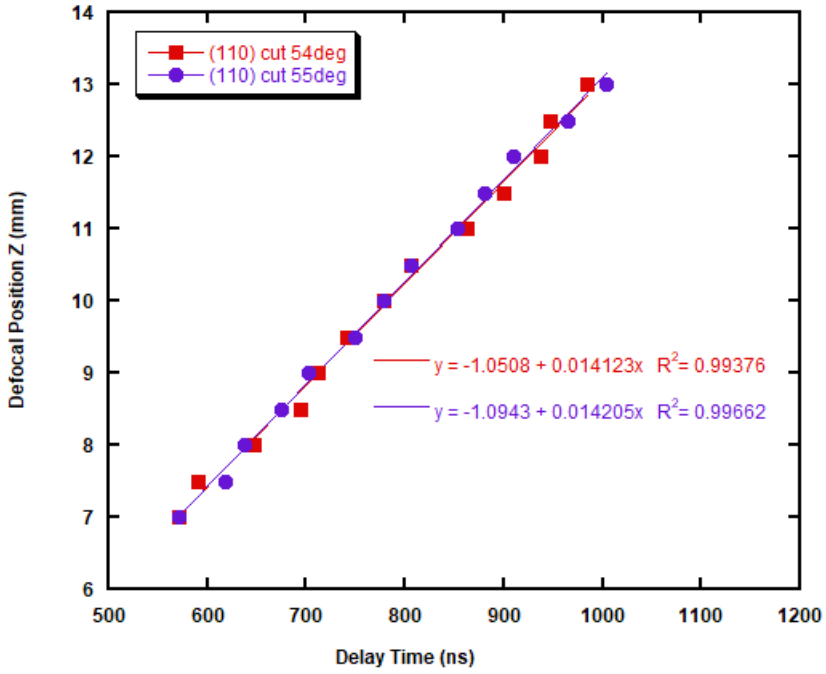

(c)

Figure 4-7 Z(t) Plots from different measurement directions on testing sample of wave propagting on (a) [100] (b) [110] (c) [111] directions of cubic structure

From Fig. 4-8, the results of $V_{R[100]}$ shows good consistency among different measurements. The velocities from both [100] and [010] directions from (100) cut are similar with the one measured from [001] direction from (110) cut. Beside the symmetric nature of cubic materials along the [100], [010] and [001] directions, such good agreement is also attributed to the fact that these three directions are crystallographic axis in cubic material. When Rayleigh surface wave propagates along those directions, it is always in the consistent wave mode without other surface wave modes being excited and compounding with each other [1]. For the same reason of material symmetry, the measured $V_{R[110]}$ are almost the same obtained from two symmetric directions [110] and [10] on (100) cut. However, the velocity $V_{R[110]}$ measured in (110) cut sample is about 10% higher. Such noticeable difference can be explained based on the complicity in

surface wave modes propagating in anisotropic solids. Different surface wave modes could be generated when propagating on different cuts in anisotropic solid. This interference of multiple wave modes was also observed in the experimental studied using the V(z) method analysis on different cubic materials such as Ge(111) [13] $LiNbO_3$ [42] and Si(100) [14, 17].

Based on the numerical studies on surface wave propagating on (100) plane and (110) plane of cubic crystal [43], two kinds of surface waves (i.e. regular Rayleigh surface wave (R) and pseudo-Rayleigh surface wave(p-R)) could be generated depending on the propagation plane and direction of the surface wave. The regular Rayleigh wave propagates with a velocity lower than bulk waves, while the velocity of the pseudo-Rayleigh wave, which exists within some isolated angles on certain anisotropic planes, is higher than the lowest transverse bulk wave [24]. When the propagating direction of surface wave is away from crystallographic axis, either R or p-R is generated depending on the anisotropic planes on which the surface wave is generated [24]. Studies [24, 43] also show that for cubic materials whose anisotropic ratio meets $\eta = 2c_{66}/(c_{11} - c_{12}) > 1$, there exists a 30 degrees isolated angle about [110] direction on (100) plane within which the velocity of regular Rayleigh wave is close to the smallest transverse bulk wave, and the pseudo-Rayleigh wave would appear on these directions; whereas, for (110) plane the isolated angle doesn't exist, resulting the surface wave always propagating as regular Rayleigh mode even on [110] direction. Having a closer look at the hexic Christoffel equation (Equation 4-7 for (100) plane or Equation 4-24 for (110) plane), the regular Rayleigh wave corresponds to the three roots with negative imaginary part out of the six or three pairs of complex solutions, which indicates wave attenuation along the thickness direction. While pseudo-Rayleigh wave corresponds to the case when there are two or more real solutions for the secular equation. Such kind of wave with real solutions will have an un-decaying velocity component along the thickness direction and

propagate much deeper into solid. Overall propagation velocity for pseudo-Rayleigh wave is expected to be higher than regular Rayleigh wave [24]. Based on the above explanation, for silicon, whose $\eta = 1.56$, the V_R measured on (100) plane is the pseudo-Rayleigh wave velocity while the one obtained from (110) plane is the regular Rayleigh wave velocity, resulting two different measured velocities.

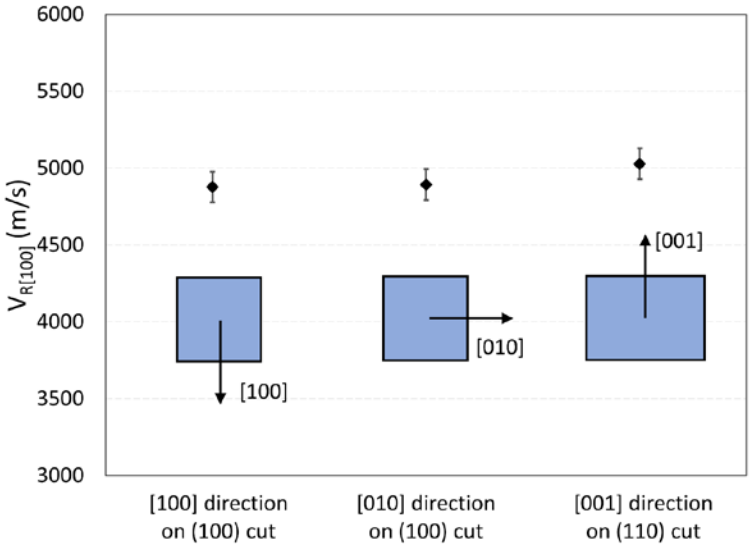

(a)

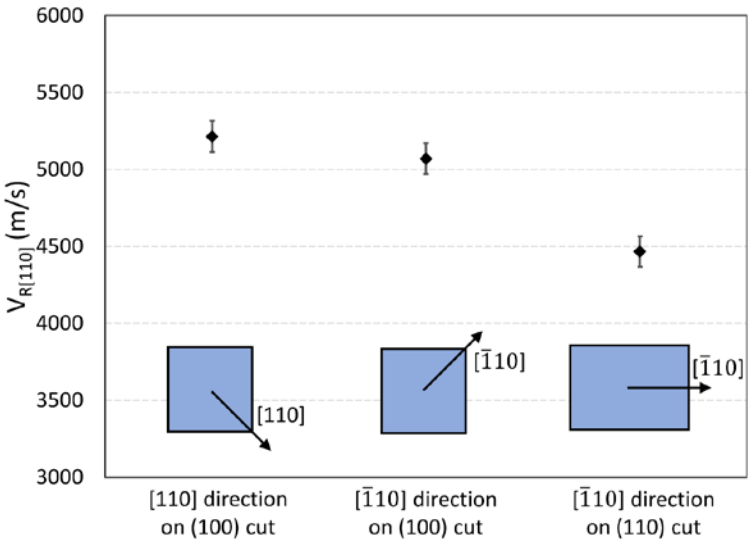

(b)

Figure 4-8 (a) VR on [100] directions; (b) VR on [110] directions

Based on the cubic structure symmetry and the experiment results discussed above, an averaged $V_{R[100]}$ is calculated from the measured V_R from multiple testing conducted on [100] and [010] directions on (100) cut. Similar calculation is performed for $V_{p-R[110]}$ on (100), and $V_{R[100]}$,

$V_{R[110]}$ and $V_{R[111]}$ from (110) cut. The averaged wave velocities are summarized in Table 3 in order to validate the velocities predicted by the model developed in Section 4-2 (the 'Calculated velocity' in Table 4-3). Overall, the prediction shows reasonably good agreement with experimental measurement results within less 1% difference, except in [111] direction on (110) plane model prediction about 4% higher. Such difference is probably because the alignment error increases as [111] direction is not directly parallel or orthogonal to the reference direction which is the primary cut direction on testing sample. However, as being for the concern of material property characterization method developed by this work, the discrepancy is proven to have negligible impact on predicting material property in the following section. In addition, Lee's work [17] for velocity measurement on (100) plane is also listed out as reference cases for comparison, and similar result further confirms the accuracy of model and experiment method in this work.

Particularly, after further examining two different surface wave modes in the same [110] direction but different cut planes (100) and (110), the model matches with experiment measures very well and more importantly predicts the p-R wave velocity about 13% higher than R wave as a result of its undampened velocity component. Such conformity demonstrates that mechanistic model derived in this work well captures the underlying surface wave propagation physics and theory.

Table 4-3 Measured Rayleigh surface velocity vs Calculated Velocity

	Surface wave Mode	Velocity direction	Measured velocity (m/s)	Calculated Velocity (m/s)	Reference velocity [17]
(100) plane/cut	R	[100]	4930 (±2.9%)	4916	4915
	p-R	[110]	5057 (±2.7%)	5100	5082
(110) plane/cut	R	[100]	4928 (±3.2%)	4916	------
	R	[110]	4500 (±2.9%)	4490	------
	R	[111]	4774 (±2.9%)	4990	------

4.4 Application of Developed Model for Elastic Constants Characterization

From the comparison between model and experiment data discussed in the above section, it is very obvious that the developed mechanistic model for surface wave propagation can be employed to predict the propagation velocity in various directions and cuts when the material properties, i.e. stiffness constants are given. More importantly, the significance and objective of this research work is to introduce an improved but simplified method for material property characterization based on experimentally measured velocities and corresponding wave propagation equations which is used in form of inverse functions. Although such concept has been introduced and studied for several decades, the traditional ultrasound-based methods normally are limited to utilize longitudinal and transverse velocities. Consequently, in order to obtain three independent velocity measurements, such method typically requires at least two transducers and two cut samples. Specifically, longitudinal velocity V_L and transverse bulk wave velocity V_T are measured by longitudinal type and transverse type transducers, respectively. $V_{L[100]}$ and $V_{T[100]}$ are from (100) cut sample, and $V_{L[110]}$ from (110) cut sample.

The mechanistic model and corresponding algebraic equation proposed in this work make possible to utilize surface wave together with longitudinal wave for property characterization. Additionally, the line-focus transducer is able to measure both types of wave velocities simultaneously and therefore this work can propose much simplified characterization method on a basis of a single transducer for a single or two cut samples. As being demonstrated in previous section, both longitudinal and Rayleigh surface wave velocities on [100], [110], and [111] directions can be measured and calculated from line-focus transducer echo signals from (100), (110), and (111) three different cut samples. Those available data allow multiple possible combinations of independent velocity measurement for solving three unknown stiffness constants. However, only two combinations are proposed for simplified and practical material characterization method and summarized in Table 4-4. Both disregard the $V_{L[111]}$ to eliminate the need of three cut samples and $V_{R[111]}$ to avoid complicated computation process that Rayleigh surface wave model is involved on this direction. Approach (I) has slightly less computation complexity but requires two sample cuts, as it needs to measure two longitudinal bulk waves $V_{L[100]}$ and $V_{L[110]}$ on (100) and (110) cut samples in addition to one Rayleigh surface wave $V_{R[100]}$ from either of two cut samples. As a comparison, approach (II) only requires a single sample cut (110) to obtain two Rayleigh surface waves $V_{R[100]}$ and $V_{R[110]}$, and one longitudinal wave $V_{L[110]}$. It is worth noting that, $V_{R[110]}$ from (100) cut sample, although also available to use, is still disregarded given the fact that pseudo-Rayleigh wave interferes the velocity measurement.

The prediction of stiffness constants of silicon cubic material is performed by these two approaches and compared against reference values from literature [1] which is based on traditional ultrasound method. Overall, results from both approaches have reasonably good agreement with

reference values of three independent stiffness constants. Approach (I) predicts very well on c_{11} with marginally higher value but overpredicts c_{12} and c_{66} by about 3~4%, while approach (II) matches well with reference value on c_{66} but overpredicts c_{11} and c_{12} roughly by 3~6%. This indicates using Rayleigh surface wave mode and measurement can be a better alternative to traditional method for industrial application, considering its much simpler test setup and acceptably good measurement accuracy. Firstly, measurement for Rayleigh surface wave is based on the generating surface wave on the surfaces of the test sample, which is initiated by the longitudinal wave incidents at special direction on the sample, so it could be generated by the same transducer that generates longitudinal bulk wave. While, the traditional method based on longitudinal and transverse waves require at least two transducers, specifically one longitudinal and one transverse type transducer, to generate both types of waves. Secondly, the orientation of the test sample can be easily and precisely controlled with motorized stages for wave measurement on certain directions. However, the only limitation of the line focus ultrasound system established in this work is that only relative thick test sample can be characterized, because the mechanic model is based on an assumption of wave propagating on semi-infinite plane and the thickness is at least one scale larger than the wavelength (λ). For silicon studied in this work, the test sample thickness is about 10 mm, because the surface wave length is estimated about 0.6 mm ($\lambda = V/f = 0.6mm$) given the surface wave in a magnitude of 5000 m/s and transducer frequency of about 8 MHz. However, this limitation can be overcome by employing transducer with much higher frequency [13] and therefore the test sample can be one or two magnitude thinner.

Table 4-4 Calculation equation summary

Approach	Velocity	Equations	Sample Cut
I	$V_{L[100]}$	$\rho V_{L[100]}^2 = c_{11}$ [1]	(100)
	$V_{L[110]}$	$2\rho V_{L[110]}^2 = \left(c_{11} + c_{12} + 2c_{66}\right)$ [1]	(100) or (110)
	$V_{R[100]}$	$c_{66}(c_{11} - \zeta)\zeta^2 - c_{11}(c_{66} - \zeta)\left(c_{11} - \frac{c_{12}^2}{c_{11}} - \zeta\right)^2 = 0$	(110)
II	$V_{L[110]}$	$2\rho V_{L[110]}^2 = \left(c_{11} + c_{12} + 2c_{66}\right)$ [1]	(110)
	$V_{R[100]}$	$c_{66}(c_{11} - \zeta)\zeta^2 - c_{11}(c_{66} - \zeta)\left(c_{11} - \frac{c_{12}^2}{c_{11}} - \zeta\right)^2 = 0$	
	$V_{R[110]}$	$(c_{11} - c_{12})(c - \zeta)\zeta^2 - c(c_{11} - c_{12} - 2\zeta)\left(\frac{b}{16c} - \zeta\right)^2 = 0$	

Table 4-5 Characterization of Stiffness constants

Stiffness (10^{10} N/m)	Approach I	Approach II	Ref [1]
c_{11}	16.59	17.04	16.56
c_{12}	6.69	6.82	6.39
c_{66}	8.22	7.93	7.95

*Mass density $\rho = 2329 kg / m^3$

4.5 Summary

A stiffness constant characterization method on cubic materials is developed based on the simultaneous measurement of Rayleigh surface wave and longitudinal bulk wave velocities. A theoretical mechanistic model is established to describe the relationship between stiffness

constants and Rayleigh surface wave propagating on two characteristic planes (100) and (110) of cubic material, and the velocity equations on [100] and [110] crystallographic directions are derived. Single crystal silicon is used as a testing material to validate the mechanistic model against experiment using the inhouse developed ultrasound test system with a lens-less line-focus ultrasound transducer. The model validation is conducted and shows that the mechanistic model derived in this work can well predict the surface wave propagating character in cubic solids. The difference between the predicted and measured wave velocities is less 4%. In addition, the validation of this mechanistic model for Rayleigh surface wave propagation is further achieved by successfully predicting the presence in certain propagation planes and the values of two different kinds of Rayleigh surface wave, i.e. regular and pseudo.

Using the mechanistic model inversely that predicts stiffness constants with given wave velocities, a new characterization method is established with simultaneous measurement of Rayleigh surface and longitudinal bulk waves. Compared to traditional methods that are only based on bulk waves and therefore requires two or more step measurements, the new method significantly simplifies the test procedure and reduces sample usage/preparation efforts, because single sample cut is required for a single measurement to obtain three independent velocities – one bulk wave and two surface waves along different propagation directions. Overall, for the test material of anisotropic crystal silicon, the predicted stiff constants, compared to reference values, demonstrates a reasonably good accuracy with less 6% discrepancy.

5.0 Trigonal Material

This chapter continues the study of stiffness constant characterization method based on acoustic wave propagation for anisotropic trigonal materials. The theoretical study based on fundamental wave propagation equations is conducted to develop the mechanistic model of trigonal material and then the model is validated experimentally using single crystal quartz as an example. Based on the validated mechanistic model, the novel approach to characterize stiffness constants of anisotropic trigonal material is proposed based on the simultaneous measurements of Rayleigh surface wave and longitudinal bulk wave on X, Y, and Z directions realized by the lens-less line-focus transducer. As a potentially better alternative to traditional methods which is only based on bulk wave and therefore requires two or more step measurements, this new method has simplified test procedure and reduced sample usage/preparation for full characterization of stiffness constants. The stiffness constants of test sample predicted by the new method demonstrates a very good agreement of less 5% difference with reference value from literature.

5.1 Mechanistic Model Development

For solid which has a crystal structure belongs to classes of $\bar{3}m$, 32 and $3m$ of trigonal system, the stiffness matrix is given as:

$$c_{pqrs} = \left(c_{\alpha\beta}\right) = \begin{pmatrix} c_{11} & c_{12} & c_{13} & c_{14} & 0 & 0 \\ c_{12} & c_{11} & c_{13} & -c_{14} & 0 & 0 \\ c_{13} & c_{13} & c_{33} & 0 & 0 & 0 \\ c_{14} & -c_{14} & 0 & c_{44} & 0 & 0 \\ 0 & 0 & 0 & 0 & c_{44} & c_{14} \\ 0 & 0 & 0 & 0 & c_{14} & c_{66} \end{pmatrix} \text{ where } c_{66} = \frac{c_{11} - c_{12}}{2}$$

For the surface wave propagating along the crystal axes of a trigonal crystal, the tensor c'_{ijkl} is equal to the stiffness tensor c_{pqrs}. Refer to the general Christoffel tensor in (A7), the specific Christoffel equation for Trigonal materials is obtained:

$$\begin{pmatrix} \Gamma_{11} - \zeta & \Gamma_{12} & \Gamma_{13} \\ \Gamma_{12} & \Gamma_{22} - \zeta & \Gamma_{23} \\ \Gamma_{13} & \Gamma_{23} & \Gamma_{33} - \zeta \end{pmatrix} \begin{pmatrix} {}^{\circ}u_1 \\ {}^{\circ}u_2 \\ {}^{\circ}u_3 \end{pmatrix} = 0 \qquad \textbf{(5-1)}$$

And the Christoffel's Matrix Γ_{il} has the non-zero components:

$$\begin{aligned} \Gamma_{11} &= c_{11}l_1^2 + c_{66}l_2^2 + c_{44}l_3^2 + 2c_{14}l_2l_3 & \Gamma_{12} &= \Gamma_{21} = \left(c_{12} + c_{66}\right)l_1l_2 + 2c_{14}l_1l_3 \\ \Gamma_{22} &= c_{66}l_1^2 + c_{11}l_2^2 + c_{44}l_3^2 - 2c_{14}l_2l_3 & \Gamma_{13} &= \Gamma_{13} = 2c_{14}l_1l_2 + \left(c_{13} + c_{44}\right)l_1l_3 \\ \Gamma_{33} &= c_{44}l_1^2 + c_{44}l_2^2 + c_{33}l_3^2 & \Gamma_{23} &= \Gamma_{23} = c_{14}l_1^2 - c_{14}l_2^2 + \left(c_{13} + c_{44}\right)l_2l_3 \end{aligned} \qquad \textbf{(5-2)}$$

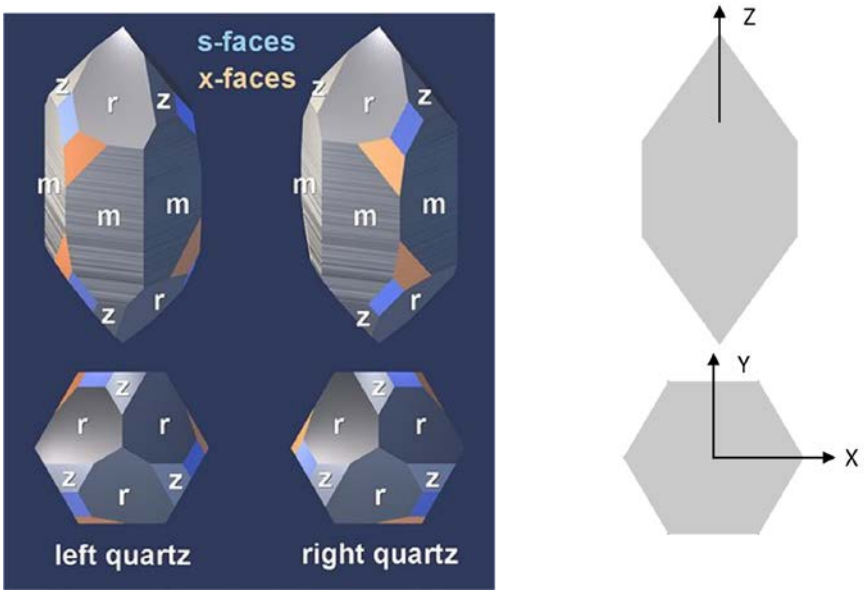

Figure 5-1 Structure and Crystallographic Axis [44]

5.1.1 XZ-Plane

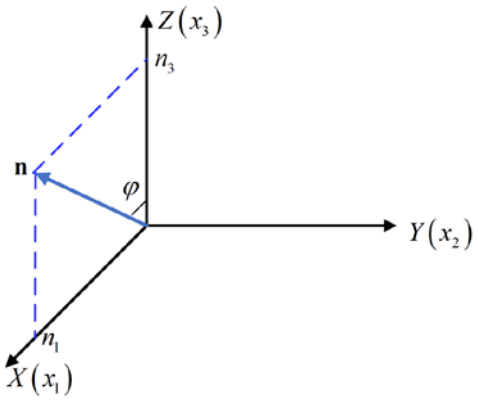

Figure 5-2 Coordinate and propagation direction of Surface wave on XZ plane

Considering the surface wave propagates on (x_1, x_3) plane along direction $\mathbf{n}$, where $n_1 = \sin\varphi, n_2 = 0, n_3 = \cos\varphi$ as shown in Fig. 5-2, based on the theory of wave propagation [1], the general particle polarization displacement u_l is assumed in the format:

$$u_l = U_l(x_2)\exp\left(ik\left(Vt - n_1x_1 - n_3x_3\right)\right) \quad \textbf{(5-3)}$$

Where the decay term $U_l(x_2)$ can be specified as $U_l(x_2) = \left(\sum_{r=1}^{3} A_r \circ u_l^{(r)} \exp(-ikq_r x_2)\right)$ in which A_r is the amplitude, $\circ u_l^{(r)}$ is the components of polarization vector, and q_r is the decay constants where r =1,2,3. And in the sinusoidal wave term, V is the propagating phase velocity, and k is the wavenumber. Therefore, the l_1, l_2 and l_3 in (5-2) are replaced by n_1, q_r and n_3 correspondingly, so the Christoffel tensor has the six components:

$$\begin{aligned}
\Gamma_{11} &= c_{11}n_1^2 + c_{66}q_r^2 + c_{44}n_3^2 + 2c_{14}q_r n_3 & \Gamma_{12} &= \Gamma_{21} = \left(c_{12} + c_{66}\right)n_1 q_r + 2c_{14}n_1 n_3 \\
\Gamma_{22} &= c_{66}n_1^2 + c_{11}q_r^2 + c_{44}n_3^2 - 2c_{14}q_r n_3 & \Gamma_{13} &= \Gamma_{31} = 2c_{14}n_1 q_r + \left(c_{13} + c_{44}\right)n_1 n_3 \\
\Gamma_{33} &= c_{44}n_1^2 + c_{44}q_r^2 + c_{33}n_3^2 & \Gamma_{23} &= \Gamma_{32} = c_{14}n_1^2 - c_{14}q_r^2 + \left(c_{13} + c_{44}\right)q_r n_3
\end{aligned} \quad \textbf{(5-4)}$$

Therefore, the secular equation of Christoffel equation is

$$\det\left(\Gamma_{il} - \delta_{il}\zeta\right) = 0 \quad \textbf{(5-5)}$$

$\zeta = \rho V_R^{\,2}$ is the eigenvalue of Γ_{il}.

As the surface wave propagates on the $\left(x_1, x_3\right)$ plane, the Mechanical boundary condition on the free surface need to be satisfied.

$$\begin{aligned}
T_2 = T_{22} &= c'_{22kl}\frac{\partial u_l}{\partial x_k} = \frac{\partial}{\partial x_1}\left(c_{12}u_1\right) + \frac{\partial}{\partial x_2}\left(c_{11}u_2 - c_{14}u_3\right) + \frac{\partial}{\partial x_3}\left(-c_{14}u_2 + c_{13}u_3\right) = 0 \\
T_4 = T_{32} &= c'_{32kl}\frac{\partial u_l}{\partial x_k} = \frac{\partial}{\partial x_1}\left(c_{14}u_1\right) + \frac{\partial}{\partial x_2}\left(-c_{14}u_2 + c_{44}u_3\right) + \frac{\partial}{\partial x_3}\left(c_{44}u_2\right) = 0 \qquad \textbf{at } x_2 = 0 \\
T_6 = T_{12} &= c'_{12kl}\frac{\partial u_l}{\partial x_k} = \frac{\partial}{\partial x_1}\left(c_{66}u_2 + c_{14}u_3\right) + \frac{\partial}{\partial x_2}\left(c_{66}u_1\right) + \frac{\partial}{\partial x_3}\left(c_{14}u_1\right) = 0
\end{aligned} \quad \textbf{(5-6)}$$

Then, substitute the general solution (5-3) into (5-6).

$\frac{\partial u_l}{\partial x_k} = n_k U_l$ (when k =1,3), where $U_l(x_2) = \left(\sum_{r=1}^{3} A_r \circ u_l^{(r)} \exp(-ikq_r x_2)\right)$

$\frac{\partial u_l}{\partial x_k} = W_l$ (when $k = 2$), where $W_l(x_2) = \left(\sum_{r=1}^{3} A_r \circ u_l^{(r)} q_r \exp(-ikq_r x_2)\right)$

So that the boundary condition can be written as

$$\begin{pmatrix} \Lambda_{11} & \Lambda_{12} & \Lambda_{13} \\ \Lambda_{21} & \Lambda_{22} & \Lambda_{23} \\ \Lambda_{31} & \Lambda_{32} & \Lambda_{33} \end{pmatrix} \begin{pmatrix} A_1 \\ A_2 \\ A_3 \end{pmatrix} = 0 \qquad \textbf{(5-7)}$$

Where the boundary condition matrix $\mathbf{\Lambda}$ is in terms of c_{ijkl}, ρ, V_R and q_r. The secular equation for matrix $\mathbf{\Lambda}$ must be satisfied so that the boundary condition is satisfied:

$$\det\left(\Lambda_{ij}\right) = 0 \qquad \textbf{(5-8)}$$

For the special case when the surface wave propagates on **X direction** ($n_1 = 1, n_3 = 0$), $\mathbf{\Gamma}$ has the components:

$$\begin{aligned} \Gamma_{11} &= c_{11} + c_{66} q_r^2 & \Gamma_{12} &= \Gamma_{21} = \left(c_{12} + c_{66}\right) q_r \\ \Gamma_{22} &= c_{66} + c_{22} q_r^2 & \Gamma_{13} &= \Gamma_{31} = 2c_{14} q_r \\ \Gamma_{33} &= c_{44} + c_{44} q_r^2 & \Gamma_{23} &= \Gamma_{32} = c_{14} - c_{14} q_r^2 \end{aligned} \qquad \textbf{(5-9)}$$

Chose eigenvector of Γ_{il} as

$$\begin{pmatrix} {}^{\circ}u_1^{(r)} \\ {}^{\circ}u_2^{(r)} \\ {}^{\circ}u_3^{(r)} \end{pmatrix} = \begin{pmatrix} 1 \\ s_r \\ p_r \end{pmatrix} \quad \textbf{where } (r = 1,2,3)\textbf{, with } \begin{aligned} p_r &= \frac{\left(\Gamma_{11} - \zeta\right)\Gamma_{23} - \Gamma_{12}\Gamma_{13}}{\Gamma_{12}\left(\Gamma_{33} - \zeta\right) - \Gamma_{13}\Gamma_{23}} \\ s_r &= \frac{\Gamma_{13}\left(\Gamma_{13} - \Gamma_{33} + \zeta\right)}{\Gamma_{12}\left(\Gamma_{33} - \zeta\right) - \Gamma_{13}\Gamma_{23}} \end{aligned} \qquad \textbf{(5-10)}$$

Substitute (5-10) into (5-6) to get the matrix $\mathbf{\Lambda}$ has the components:

$$\begin{aligned} \Lambda_{11} &= c_{14} p_1 + c_{66} q_1 + c_{66} s_1 & \Lambda_{12} &= c_{14} p_2 + c_{66} q_2 + c_{66} s_2 & \Lambda_{13} &= c_{14} p_3 + c_{66} q_3 + c_{66} s_3 \\ \Lambda_{21} &= c_{12} - c_{14} p_1 q_1 + c_{11} q_1 s_1 & \Lambda_{22} &= c_{12} - c_{14} p_2 q_2 + c_{11} q_2 s_2 & \Lambda_{23} &= c_{12} - c_{14} p_3 q_3 + c_{11} q_3 s_3 \\ \Lambda_{31} &= c_{14} + c_{44} p_1 q_1 - c_{14} q_1 s_1 & \Lambda_{32} &= c_{14} + c_{44} p_2 q_2 - c_{14} q_2 s_2 & \Lambda_{33} &= c_{14} + c_{44} p_3 q_3 - c_{14} q_3 s_3 \end{aligned} \qquad \textbf{(5-11)}$$

For the special case when the surface wave propagates on **Z direction** ($n_1 = 0, n_3 = 1$), the Christoffel equation can be simplified as

$$\begin{pmatrix} \Gamma_{22} & \Gamma_{23} \\ \Gamma_{23} & \Gamma_{33} \end{pmatrix} \begin{pmatrix} {}^{\circ}u_2 \\ {}^{\circ}u_3 \end{pmatrix} = 0 \qquad \textbf{with} \qquad \begin{aligned} \Gamma_{22} &= c_{11}q_r^2 + c_{44} - 2c_{14}q_r \\ \Gamma_{33} &= c_{44}q_r^2 + c_{33} \\ \Gamma_{23} &= -c_{14}q_r^2 + (c_{13} + c_{44})q_r \end{aligned} \tag{5-12}$$

The secular equation $\det(\Gamma_{il} - \delta_{il}\zeta) = 0$ can be expressed as:

$$(c_{11}q_r^2 + c_{44} - 2c_{14}q_r - \zeta)(c_{44}q_r^2 + c_{33} - \zeta) - (-c_{14}q_r^2 + (c_{13} + c_{44})q_r)^2 = 0 \tag{5-13}$$

For the two acceptable solutions $q_r (r = 1, 2)$, which have negative imaginary parts, the components ${}^{\circ}u_i^{(r)}$ are given by the Christoffel equation:

$$\begin{pmatrix} {}^{\circ}u_1^{(r)} \\ {}^{\circ}u_2^{(r)} \\ {}^{\circ}u_3^{(r)} \end{pmatrix} = \begin{pmatrix} 0 \\ s_r \\ 1 \end{pmatrix} \textbf{ where } (r = 1, 2) \textbf{, with } s_r = \frac{-\Gamma_{23}}{\Gamma_{22} - \zeta} = \frac{c_{14}q_r^2 - (c_{13} + c_{44})q_r}{c_{11}q_r^2 + c_{44} - 2c_{14}q_r - \zeta} \tag{5-14}$$

Therefore, the boundary condition can be simplified as:

$$\begin{pmatrix} T_{22} \\ T_{32} \end{pmatrix} = \begin{pmatrix} \Lambda_{11} & \Lambda_{12} \\ \Lambda_{21} & \Lambda_{22} \end{pmatrix} \begin{pmatrix} A_1 \\ A_2 \end{pmatrix} = \begin{pmatrix} 0 \\ 0 \end{pmatrix} \tag{5-15}$$

where $\begin{aligned} \Lambda_{11} &= c_{11}s_1q_1 - c_{14}(q_1 + s_1) + c_{13} & \Lambda_{12} &= c_{11}s_2q_2 - c_{14}(q_2 + s_2) + c_{13} \\ \Lambda_{21} &= -c_{14}s_1q_1 + c_{44}(q_1 + s_1) & \Lambda_{22} &= -c_{14}s_2q_2 + c_{44}(q_2 + s_2) \end{aligned}$, so that the secular equation $\det(\Lambda_{ij}) = 0$ is given as:

$$\begin{aligned} &(c_{11}s_1q_1 - c_{14}(q_1 + s_1) + c_{13})(-c_{14}s_2q_2 + c_{44}(q_2 + s_2)) \\ &-(c_{11}s_2q_2 - c_{14}(q_2 + s_2) + c_{13})(-c_{14}s_1q_1 + c_{44}(q_1 + s_1)) = 0 \end{aligned} \tag{5-16}$$

5.1.2 **XY-Plane**

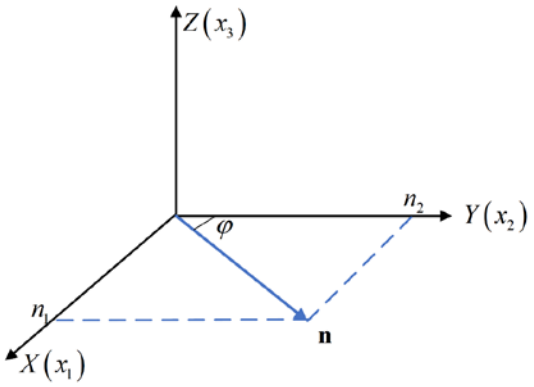

Figure 5-3 Coordinate and propagation direction of Surface wave on XY plane

Similarly, considering the surface wave propagates on (x_1, x_2) plane along direction $\mathbf{n}$, where $n_1 = \sin\varphi, n_2 = \cos\varphi, n_3 = 0$ as shown in Fig. 5-3, based on the theory of wave propagation [1], the general particle polarization displacement u_l is assumed in the format:

$$u_l = U_r(x_3)\exp\left(ik\left(Vt - n_1x_1 - n_2x_2\right)\right) \tag{5-17}$$

Where the decay term $U_r(x_3)$ can be specified as $U_r(x_3) = \left(\sum_{r=1}^{3} A_r \circ u_l \exp(-ikq_r x_3)\right)$. Therefore, the l_1, l_2 and l_3 in (5-2) is replaced by n_1, n_2 and q_r correspondingly, so the Christoffel tensor has the six components:

$$\begin{aligned}
\Gamma_{11} &= c_{11}n_1^2 + c_{66}n_2^2 + c_{44}q_r^2 + 2c_{14}n_2q_r & \Gamma_{12} &= \Gamma_{21} = (c_{12} + c_{66})n_1n_2 + 2c_{14}n_1q_r \\
\Gamma_{22} &= c_{66}n_1^2 + c_{11}n_2^2 + c_{44}q_r^2 - 2c_{14}n_2q_r & \Gamma_{13} &= \Gamma_{13} = 2c_{14}n_1n_2 + (c_{13} + c_{44})n_1q_r \\
\Gamma_{33} &= c_{44}n_1^2 + c_{44}n_2^2 + c_{33}q_r^2 & \Gamma_{23} &= \Gamma_{23} = c_{14}n_1^2 - c_{14}n_2^2 + (c_{13} + c_{44})n_2q_r
\end{aligned} \tag{5-18}$$

For the special case when the surface wave propagates on **Y direction** ($n_1 = 0, n_2 = 1$), the Christoffel equation can be simplified as

$$\begin{pmatrix} \Gamma_{22}-\zeta & \Gamma_{23} \\ \Gamma_{23} & \Gamma_{33}-\zeta \end{pmatrix}\begin{pmatrix} {}^{\circ}u_2 \\ {}^{\circ}u_3 \end{pmatrix}=0 \qquad \textbf{with} \qquad \begin{aligned} \Gamma_{22} &= c_{11}+c_{44}q_r^2-2c_{14}q_r \\ \Gamma_{33} &= c_{44}+c_{33}q_r^2 \\ \Gamma_{23} &= -c_{14}+(c_{13}+c_{44})q_r \end{aligned} \tag{5-19}$$

Therefore, the secular equation of Christoffel equation is

$$(\Gamma_{22}-\zeta)(\Gamma_{33}-\zeta)-\Gamma_{23}^2=0 \tag{5-20}$$

where $\zeta=\rho V_{R-Y}{}^2$ is the eigenvalue of Christoffel tensor.

Based on the mechanical boundary condition, at $x_3=0$, $T_{i3}=\dfrac{\partial}{\partial x_k}(c_{i3kl}u_l)=0$ must be satisfied, it could be represented in explicit form:

$$\begin{aligned} T_{13} &= \frac{\partial}{\partial x_1}(c_{14}u_2+c_{44}u_3)+\frac{\partial}{\partial x_2}(c_{14}u_1)+\frac{\partial}{\partial x_3}(c_{44}u_1) \\ T_{23} &= \frac{\partial}{\partial x_1}(c_{14}u_1)+\frac{\partial}{\partial x_2}(-c_{14}u_2+c_{44}u_3)+\frac{\partial}{\partial x_3}(c_{44}u_2) \\ T_{33} &= \frac{\partial}{\partial x_1}(c_{13}u_1)+\frac{\partial}{\partial x_2}(c_{13}u_2)+\frac{\partial}{\partial x_3}(c_{33}u_3) \end{aligned} \tag{5-21}$$

For the two acceptable solutions $q_r\,(r=1,2)$, which have negative imaginary parts, the components ${}^{\circ}u_i^{(r)}$ are given by the Christoffel equation:

$$\begin{pmatrix} {}^{\circ}u_1^{(r)} \\ {}^{\circ}u_2^{(r)} \\ {}^{\circ}u_3^{(r)} \end{pmatrix}=\begin{pmatrix} 0 \\ s_r \\ 1 \end{pmatrix} \textbf{ where } (r=1,2)\textbf{, with } s_r=\frac{-\Gamma_{23}}{\Gamma_{22}-\zeta}=\frac{c_{14}q_r^2-(c_{13}+c_{44})q_r}{c_{11}+c_{44}q_r^2-2c_{14}q_r-\zeta} \tag{5-22}$$

Therefore, the boundary condition can be simplified as:

$$\begin{pmatrix} T_{23} \\ T_{33} \end{pmatrix}=\begin{pmatrix} \Lambda_{11} & \Lambda_{12} \\ \Lambda_{21} & \Lambda_{22} \end{pmatrix}\begin{pmatrix} A_1 \\ A_2 \end{pmatrix}=\begin{pmatrix} 0 \\ 0 \end{pmatrix} \tag{5-23}$$

where $\begin{aligned} \Lambda_{11} &= -c_{14}s_1+c_{44}(1+s_1q_1) & \Lambda_{12} &= -c_{14}s_2+c_{44}(1+s_2q_2) \\ \Lambda_{21} &= c_{13}s_1+c_{33}q_1 & \Lambda_{22} &= c_{13}s_2+c_{33}q_2 \end{aligned}$, so that the secular equation $\det(\Lambda_{ij})=0$ is obtained:

$$\left(-c_{14}s_1 + c_{44}\left(1+s_1q_1\right)\right)\left(c_{13}s_2 + c_{33}q_2\right) - \left(-c_{14}s_2 + c_{44}\left(1+s_2q_2\right)\right)\left(c_{13}s_1 + c_{33}q_1\right) = 0 \qquad \textbf{(5-24)}$$

5.2 Numerical Solution and Experimental Validation

5.2.1 Material

α-Quartz is used for the experimental and numerical study in order to validate the developed model for surface wave propagation in anisotropic trigonal material. As a typical material in *32* group of trigonal structure, it is a good benchmark to evaluate the performance of the line-focus ultrasound system and time-resolved defocusing method, since the material is easily commercially accessible with stable material quality. This consistent property will help mitigate possible measurement uncertainty generated from quality variation of test material. In addition, the mechanical property of α-Quartz has been examined in detail for decades in many open literatures [1], therefore providing reliable data as reference.

The customized single crystal α-Quartz bulks (by University Wafers Inc., MD) with 50mm in diameter and 10mm thick are used for experiment measurement, and test samples consist of three different directional cuts: X-cut, Y-cut and Z-cut (i.e. YZ-plane, XZ-plane and XY-plane), with corresponding primary flats on Z, Z, and Y directions respectively. Referring to the crystallographic coordinates in Fig. 5-1, the measurement directions for each cut of test samples are depicted in Fig. 5-4. The Rayleigh wave (V_R) and longitudinal bulk wave (V_L) velocities are both generated and measured by a line-focus ultrasound testing system. The V_L and V_R on X, Y and Z directions are all measured to evaluate the measurement to full extent. Since Rayleigh wave velocities on X, Y and Z directions each can be measured from two different sample cuts, for

example V_{R-X} can be measured from either Y-cut or Z-cut sample, the velocities from all accessible directions are measured to evaluate the propagation similarity and difference from different measurement planes which is summarized in Table 5-1.

Table 5-1 Velocity Measurement Direction

Sample cut	Longitudinal bulk wave V_L	Rayleigh surface wave V_R
X	V_{L-X}	V_{R-Y} and V_{R-Z}
Y	V_{L-Y}	V_{R-X} and V_{R-Z}
Z	V_{L-Z}	V_{R-X} and V_{R-Y}

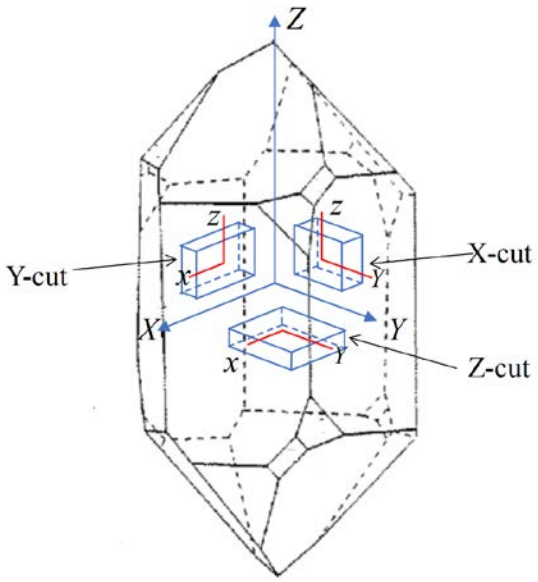

Figure 5-4 Diagram of directions of the Quartz samples of X-cut, Y-cut and Z-cut

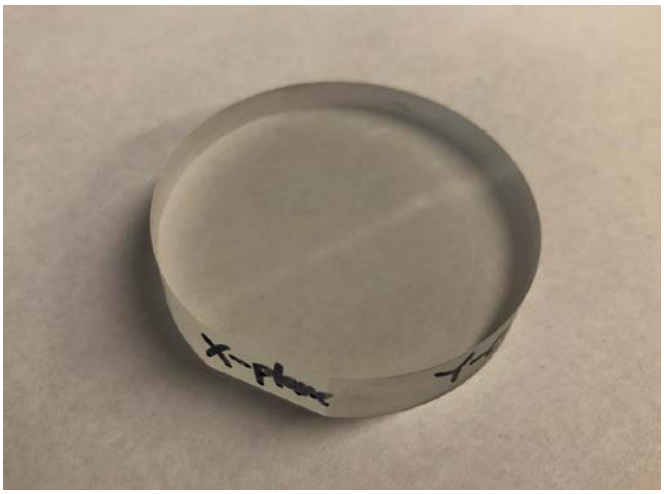

Figure 5-5 Sample picture of a Y-cut Quartz with primary flat on X direction

5.2.2 Results and Discussion

5.2.2.1 Longitudinal Bulk Wave

Figure 5-5 and Table 5-2 compare the longitudinal bulk wave velocities on three different directions obtained by three different approaches. Specifically, the model prediction is calculated from stiffness constants measured from resonate method and theoretical equations for bulk wave velocity given by [1]; the experiment data is obtained by using the measured time delay t_L and equation $V_L = 2d/t_L$ (equation 3-6) , and the uncertainty represents the standard derivation from multiple repeated experiment with the line-focus ultrasound system described in previous chapters. The velocity equations of bulk wave velocity and stiffness constants are given [1]:

$$V_{L-X} = \sqrt{c_{11}/\rho} \tag{5-25}$$

$$V_{L-Y} = \sqrt{\left(c_{11} + c_{44} + \sqrt{\left(c_{11} - c_{44}\right)^2 + 4c_{14}^2}\right)/2\rho} \tag{5-26}$$

$$V_{L-Z} = \sqrt{c_{44}/\rho} \tag{5-27}$$

where the stiffness constants are $c_{11} = 8.67$, $c_{12} = 0.7$, $c_{13} = 1.19$, $c_{14} = -1.79$, $c_{33} = 10.72$, and $c_{44} = 5.79$ (in $10^{10} N/m^2$), and mass density $\rho = 2648\,(kg/m^3)$ [1].

Overall, the experimental data has a very good agreement with model prediction based on stiffness constants measured from resonate method (error less than 1%). This demonstrates very good measurement accuracy from the line-focus ultrasound experiment system.

Therefore, to characterize the six independent unknown stiffness constants by velocity measurements, c_{11}, c_{44} and c_{14} can be obtained from the longitudinal bulk wave velocities based on equations (5-4), (5-5) and (5-6). Velocities of other modes such as transverse bulk wave and surface wave are utilized to solve the other three stiffness constants c_{12}, c_{13} and c_{33}.

Table 5-2 Summary of longitudinal bulk velocities obtained in different approaches

V_L	Model Prediction (m/s)	Experiment Data (m/s)
V_{L-X}	5722	5792 (±0.9%)
V_{L-Y}	5998	5964 (±0.7%)
V_{L-Z}	6363	6336 (±0.6%)

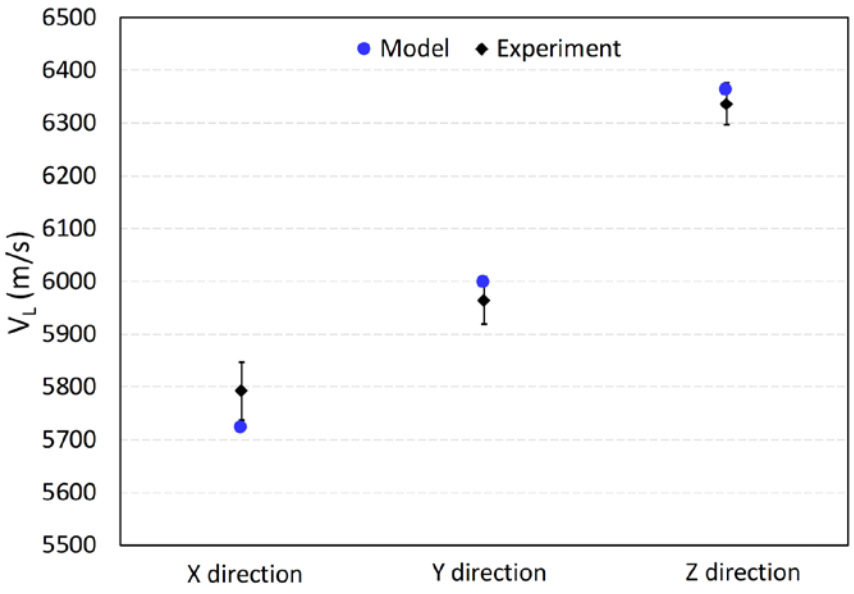

Figure 5-6 Longitudinal bulk wave from experiment measurement and model calculation

5.2.2.2 **Rayleigh surface wave**

Based on the symmetric structure of trigonal crystal (Fig. 5-1) and geometric relationship from test samples with different cut directions (Fig. 5-4), the same Rayleigh surface wave can be measured on different directions at corresponding cut samples as it is summarized in Table 5-3. The averaged values of the same Rayleigh surface wave velocities from different measurement sample cuts are summarized in Fig. 5-7. As three samples of each sample cut were used, and velocity measurements are repeated five times on each sample, the error bar in Fig. 5-7 represents the relative standard derivation from the total 15 experimental measurements from the same direction. The deviation in Fig 5-7 is less than 1% for all three directions, indicating the good measurement consistency and repeatability. The two averaged velocities measured on the same crystallographic direction but from two different sample cuts have a difference of about 2-3%, and however considering the relative standard derivation are 1.5-2.9% within the same sample cut, the

velocity difference between sample cuts is negligible. This indicates the Rayleigh surface wave has similar propagation character as long as on the same direction irrespective of crystallographic planes. Therefore, the experimental velocity on the same crystallographic direction are obtained by averaging experimental results regardless of the sample measurement direction, and their values are listed in Table 5-4.

Based on the mechanistic model developed in section 5.1, the secular equations of Christoffel equation and boundary condition are all very complex, and it is extremely difficult to directly combine both equations into one velocity equation that eliminates decay term q and therefore impossible to derive explicit expression of stiffness constants with respect to Rayleigh surface velocity. As the calculation accuracy of simplicity method has been proved in Chapter 4 for cubic material, the same approach is used for the X, Y and Z directions of α-Quartz. The searching condition first assumes that the surface wave velocity is in Rayleigh mode in which the decay constants have negative imaginary part. Table 5-4 summarizes the calculated velocities by this approach.

The experimental measurements are compared with the model prediction in Fig. 5-8. The results show good agreement between the two. This also implies that the surface waves propagating along the X, Y and Z directions on the crystallographic planes (i.e. XZ, XY and XY-planes) are always in the consistent wave mode without exciting other surface wave modes that could interfere with each other.

Table 5-3 Rayleigh Velocity and measurement cut

Rayleigh surface wave V_R	Sample cut
V_{R-X}	Y-cut, Z-cut
V_{R-Y}	X-cut, Z-cut
V_{R-Z}	X-cut, Y-cut

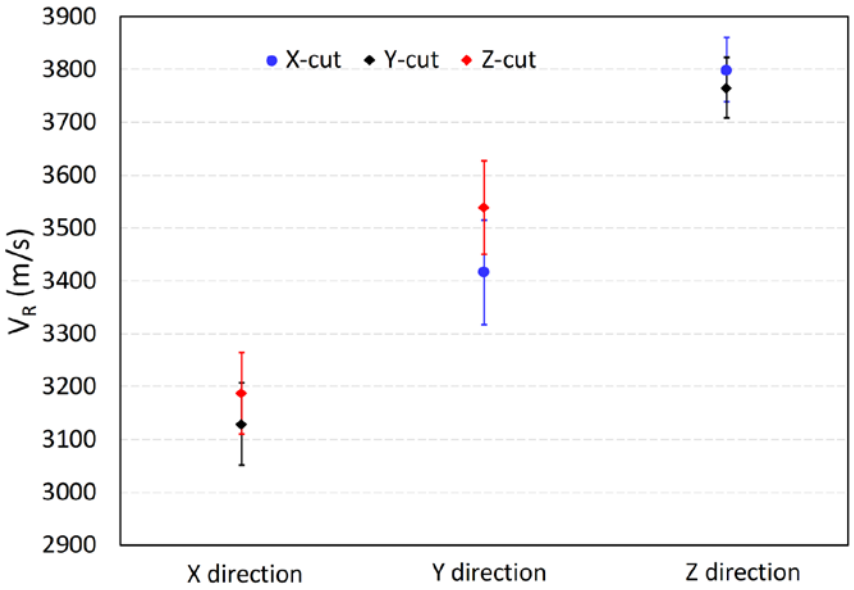

Figure 5-7 Measured velocities from different sample cut

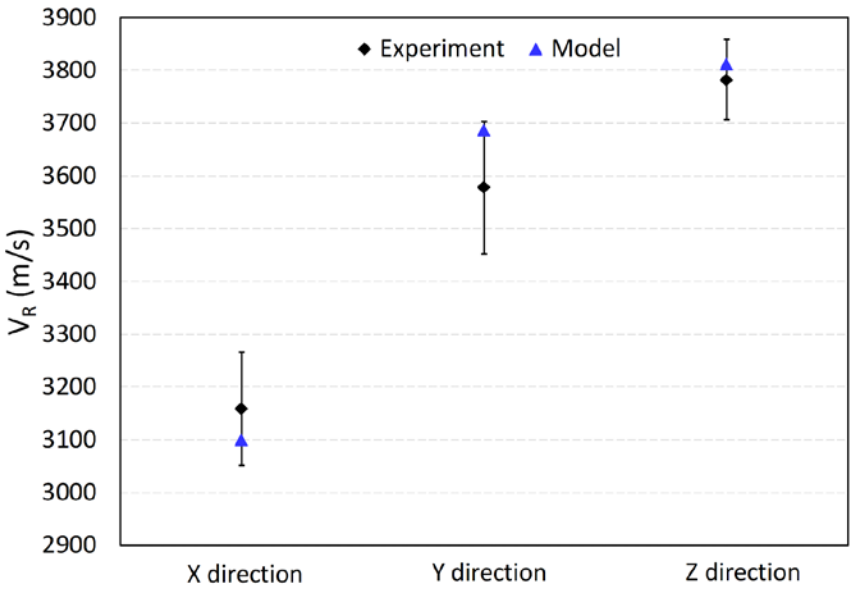

Figure 5-8 Calculated Velocity vs averaged Measured Velocity

Table 5-4 Summary of Measured Rayleigh surface velocity and Calculated Velocity

Surface wave	Calculated Velocity (m/s)	Measured velocity (m/s)	Sample cut	Averaged Measured Velocity (m/s)
V_{R-X}	3100	3129 (±2.5%)	Y cut	3158 (±3.4%)
		3187 (±2.4%)	Z cut	
V_{R-Y}	3687	3639 (±2.5%)	Z cut	3578 (±3.6%)
		3516 (±2.9%)	X cut	
V_{R-Z}	3812	3799 (±1.6%)	X cut	3782 (±2.0%)
		3765 (±1.5%)	Y cut	

Although, very little work from other scholars conducted experimental measurement of all the Rayleigh surface wave from Quartz material, there are some results reported for some other trigonal materials. Table 5-5 summarizes the comparison between the velocity predicted by this model and the reference velocity from literature, and the results shows a good agreement with less than 4% difference. This validation against independent study from literature demonstrates that

the mechanistic model developed in this work accurately describes the relationship between stiffness constants and Rayleigh surface wave velocities in trigonal materials.

Table 5-5 Model Validation on Trigonal materials

Crystal	class	Direction	Model Prediction (m/s)	Reference Velocity (m/s)	Difference
LiNbO3	3*m*	Z	3371	3488 [45]	3.3%
LiNbO3	3*m*	X	3875	3992 [45]	2.9%
LiTaO3	3*m*	Z	3214	3230 [46]	0.4%
Quartz	32	X	3100	3158 [1]	1.8%

5.3 Application of Developed Model for Stiffness Constant Characterization

The significance and objective of this research work is to introduce an improved and simplified method for material property characterization for practical industrial application based on the validated wave propagation model to solve unknown stiffness constants when there are sufficient measured velocities. As being demonstrated in previous section, both longitudinal and Rayleigh surface wave velocities on X, Y, and Z directions can be measured and calculated from line-focus transducer echo signals from X-cut, Y-cut, and Z-cut three different cut samples. Those available data allow multiple possible combinations of independent velocity measurement for solving six unknown stiffness constants. For simplified and practical material characterization method, the longitudinal bulk wave velocities on X, Y and Z directions are used to solve c_{11}, c_{14} and c_{44}. More specifically, as it is summarized in Table 5-6, V_{L-X} is used to directly solve c_{11} with equation (5-25), V_{L-Z} is used to directly solve c_{44} with equation (5-27), and substituting these

two stiffness constants into (5-26) together with the measured V_{L-Y} can obtain the constant c_{14} . From Table 5-4, due to the computation simplicity, the three stiffness constants predicted by three longitudinal bulk wave velocities match well with reference value, which is from literature and was obtained by resonant method, with difference less than 1%. However, as stiffness constants c_{12}, c_{13} and c_{33} are solved by numerical iteration in six equations (5-9), (5-11), (5-13), (5-16), (5-20) and (5-24), the final results as it is presented in Table 5-6, c_{33} is well predicted but c_{12} is underpredicted for 0.2, c_{13} is overpredicted for 0.18, this indicates that large calculation error is introduced during the numerical iteration procedure. This can be caused by the lose convergence requirement used in this study. To find the three stiffness constants using Rayleigh surface wave, the initial guess values of stiffness constants are first assumed, and substitute into (5-9) to solve decay constants, and then the solve decay constants together with the assumed stiffness constants are substitute into (5-11) to check if the equation is close to zero (within the range of ±0.1), similarly for (5-13) and (5-20) to solve decay constant and check the value of (5-16) and (5-24). If all three polynomials of (5-11), (5-16) and (5-24) are close to zero, the stiffness constants are found. In order to solve the stiffness constants with timely manner, the threshold for convergence is when the polynomials have a value within the range of ±0.1. This introduce 10% uncertainty. But this error can be minimized by using more rigorous calculation condition. Regardless of the relatively large error in c_{13} and c_{12}, which are the stiffness constants with smaller values, using the Rayleigh surface wave and Longitudinal bulk wave based on the model developed in this research, the stiffness constants are well predicted. This indicates using Rayleigh surface wave mode and measurement can be a better alternative to traditional method for industrial application, considering its much simpler test setup and acceptably good measurement accuracy.

Based on Table 5-4, the Rayleigh surface wave velocity on X, Y and Z directions are measured from (i) Y, Z and X cut samples correspondingly; (ii) Z, X, Y cut samples correspondingly. Using either approach (i) or (ii), the three longitudinal bulk wave velocities from X, Y and Z direction are measured simultaneously when the Rayleigh wave velocities are measured. Therefore, six velocities are measured from three testing and three cut samples, and the six independent stiffness constants can be characterized. Traditional methods such as resonant method and ultrasound method using bulk waves require at least six different cuts and shapes of sample and one additional type of transducer. Additionally, unlike resonant method that require the material has piezoelectric property, and the sample cuts must be cut into specific shape to generate the vibration in specific mode, the solid sample doesn't have to have piezoelectricity to support elastic acoustic wave propagation, and there is no additional sample shape requirement.

Table 5-6 Characterization of Stiffness constants

Stiffness (10^{10} N/m)	Model Prediction	Calculation Approach	Ref [1]
c_{11}	8.69	Direct solve (5-25)	8.67
c_{14}	-1.82	Solve (5-26)	-1.79
c_{44}	5.75	Direct solve (5-27)	5.79
c_{12}	0.5	Solve equations (5-9), (5-11), (5-13), (5-16), (5-20) and (5-24).	0.7
c_{13}	1.41		1.19
c_{33}	10.33		10.72

5.4 Summary

A stiffness constant characterization method on trigonal materials is developed based on the simultaneous measurement of Rayleigh surface wave and longitudinal bulk wave velocities. A theoretical mechanistic model is established to describe the relationship between stiffness constants and Rayleigh surface wave propagating on X, Y and Z crystallographic axis are derived. Single crystal Quartz is used as a testing material to validate the mechanistic model against experiment using the inhouse developed ultrasound test system with a lens-less line-focus ultrasound transducer. The model validation is conducted and shows that the mechanistic model derived in this work can well predict the surface wave propagating character in trigonal solids. The difference between the predicted and measured wave velocities is less 4%.

Using the mechanistic model inversely that predicts stiffness constants with given wave velocities, a new characterization method is established with simultaneous measurement of Rayleigh surface and longitudinal bulk waves. Overall, for the test material of anisotropic crystal Quartz, the predicted stiffness constants comparing to reference values demonstrates a reasonably good accuracy.

6.0 Mechanistic Model Development of Orthorhombic Material

This chapter further extends the development and application of stiffness constant characterization method based on acoustic wave propagation for anisotropic orthorhombic materials. The velocity equations of bulk wave propagating on the crystallographic axis are derived. And the mechanistic model that describes Rayleigh surface wave velocity as a function of stiffness constants is derived for the wave propagating along the three crystallographic axes. For orthorhombic materials, there are 9 independent stiffness constants, this requires the measurements of 9 wave velocities. In order to simplify the calculation and the measurement process, the longitudinal bulk wave velocities on X, Y and Z axes are derived. The mechanistic model for Rayleigh wave propagating on the crystal planes, and the crystallographic axes are derived. This model can be further applied to characterize the mechanical property of orthorhombic crystals.

The stiffness matrix of orthorhombic material is

$$\left(c_{\alpha\beta}\right)=\left(c_{pqrs}\right)=\begin{pmatrix} c_{11} & c_{12} & c_{13} & 0 & 0 & 0 \\ c_{12} & c_{22} & c_{23} & 0 & 0 & 0 \\ c_{13} & c_{23} & c_{33} & 0 & 0 & 0 \\ 0 & 0 & 0 & c_{44} & 0 & 0 \\ 0 & 0 & 0 & 0 & c_{55} & 0 \\ 0 & 0 & 0 & 0 & 0 & c_{66} \end{pmatrix}$$

Based on the general Christoffel equation and tensor components in (A-6) and (A-7), the Christoffel Equation of orthorhombic material is obtained

$$\begin{pmatrix} \Gamma_{11}-\zeta & \Gamma_{12} & \Gamma_{13} \\ \Gamma_{12} & \Gamma_{22}-\zeta & \Gamma_{23} \\ \Gamma_{13} & \Gamma_{23} & \Gamma_{33}-\zeta \end{pmatrix}\begin{pmatrix} {}^{\circ}u_1 \\ {}^{\circ}u_2 \\ {}^{\circ}u_3 \end{pmatrix}=0 \qquad \textbf{(6-1)}$$

where $\zeta = \rho V^2$ is the eigenvalue of Christoffel tensor, which has components as follow

$$\begin{aligned}
\Gamma_{11} &= c_{11}l_1^2 + c_{66}l_2^2 + c_{55}l_3^2 \quad & \Gamma_{12} &= (c_{12} + c_{66})l_1 l_2 \\
\Gamma_{22} &= c_{66}l_1^2 + c_{22}l_2^2 + c_{44}l_3^2 \quad & \Gamma_{13} &= (c_{13} + c_{55})l_1 l_3 \\
\Gamma_{33} &= c_{55}l_1^2 + c_{44}l_2^2 + c_{33}l_3^2 \quad & \Gamma_{23} &= (c_{23} + c_{44})l_2 l_3
\end{aligned}$$

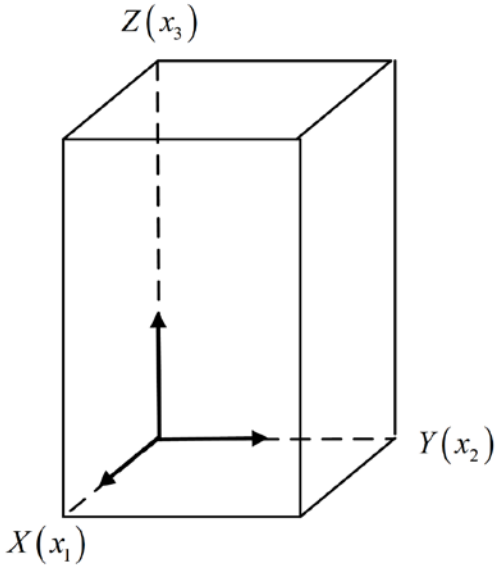

Figure 6-1 Crystal structure and the crystallographic axis of Orthorhombic materials

6.1 Bulk wave velocity equation

For the bulk wave propagates along X direction ($l_1 = 1$, $l_2 = 0$ and $l_3 = 0$), the Christoffel tensor can be simplified as

$$\Gamma_{il} = \begin{bmatrix} c_{11} & 0 & 0 \\ 0 & c_{66} & 0 \\ 0 & 0 & c_{55} \end{bmatrix}$$

therefore, the three eigenvalues are

$$\zeta_1 = \rho V_1^2 = c_{11}\ ,\ \zeta_2 = \rho V_2^2 = c_{66}\text{, and } \zeta_3 = \rho V_3^2 = c_{55}$$

And the three bulk wave velocities are

$$V_1 = \sqrt{c_{11}/\rho}\,,\ V_2 = \sqrt{c_{66}/\rho}\,,\ \text{and}\ V_3 = \sqrt{c_{55}/\rho}$$

with polarizations $°u_1$, $°u_2$ and $°u_3$ respectively. Given the definition for longitudinal wave that the polarization direction of longitudinal wave is the same with propagation direction the velocity of longitudinal bulk wave propagates on X direction is $V_L = V_1$, whereas V_2 and V_3 are the two transverse waves propagates on X direction whose polarization are orthogonal to the polarization direction.

Similarly, for bulk wave along Y direction ($l_1 = 0$, $l_2 = 1$ and $l_3 = 0$) and Z direction ($l_1 = 0$, $l_2 = 0$ and $l_3 = 1$), the Christoffel tensors are simplified as $\begin{bmatrix} c_{66} & 0 & 0 \\ 0 & c_{22} & 0 \\ 0 & 0 & c_{44} \end{bmatrix}$ and $\begin{bmatrix} c_{55} & 0 & 0 \\ 0 & c_{44} & 0 \\ 0 & 0 & c_{33} \end{bmatrix}$ correspondingly. The bulk wave velocities can be obtained and are summarized in Table 6-1.

Table 6-1 Velocity Equations of Longitudianl bulk wave in Orthorhombic Materials

Propagation Direction	Christoffel Tensor	Longitudinal Bulk Wave		Transverse Bulk Wave	
		Velocity Equation	Polarization Direction	Velocity Equation	Polarization Direction
X	$\begin{bmatrix} c_{11} & 0 & 0 \\ 0 & c_{66} & 0 \\ 0 & 0 & c_{55} \end{bmatrix}$	$V_1 = \sqrt{c_{11}/\rho}$	X	$V_2 = \sqrt{c_{66}/\rho}$	Y
				$V_3 = \sqrt{c_{55}/\rho}$	Z
Y	$\begin{bmatrix} c_{66} & 0 & 0 \\ 0 & c_{22} & 0 \\ 0 & 0 & c_{44} \end{bmatrix}$	$V_2 = \sqrt{c_{22}/\rho}$	Y	$V_1 = \sqrt{c_{66}/\rho}$	X
				$V_3 = \sqrt{c_{44}/\rho}$	Z
Z	$\begin{bmatrix} c_{55} & 0 & 0 \\ 0 & c_{44} & 0 \\ 0 & 0 & c_{33} \end{bmatrix}$	$V_3 = \sqrt{c_{33}/\rho}$	Z	$V_1 = \sqrt{c_{55}/\rho}$	X
				$V_2 = \sqrt{c_{44}/\rho}$	Y

From the Table 6-1, it can be found that the stiffness constants c_{11}, c_{22} and c_{33} are obtained by measuring the longitudinal bulk wave velocities on X, Y and Z directions respectively. The

stiffness constants c_{44} , c_{55} and c_{66} are obtained from measurement transverse bulk wave velocities. However, there are three other stiffness constants unknown. Therefore, it is necessary to establish three additional mathematic functions between stiffness constants and other wave velocities, such as Rayleigh surface wave to fully characterize all the 9 independent stiffness constants of the orthorhombic material.

6.2 Mechanistic model of Rayleigh surface Wave

6.2.1 Non-Crystallographic Directions on the Crystal planes

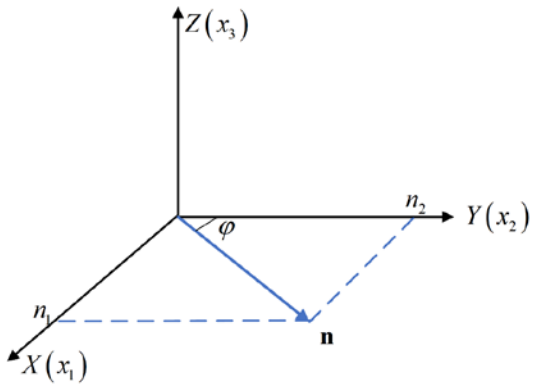

Figure 6-2 Coordinate and propagation direction of Surface wave on XY plane

Considering the surface wave propagates on XY (i.e. (x_1, x_2)) plane along direction $\mathbf{n}$, where $n_1 = \sin\varphi, n_2 = \cos\varphi, n_3 = 0$ as shown in Fig. 6-2, the general particle polarization displacement u_l is assumed to have the format:

$$u_l = U_r(x_3)\exp\left(ik\left(Vt - n_1x_1 - n_2x_2\right)\right) \quad \textbf{(6-2)}$$

where the decay term $U_r(x_3)=\left(\sum_{r=1}^{3}A_r\circ u_i\exp(-ikq_r x_3)\right)$. Therefore, the l_1, l_2 and l_3 in (6-1) is replaced by n_1, n_2 and q_r correspondingly, so the Christoffel tensor Γ_{il} has the six components:

$$\begin{aligned}
\Gamma_{11}&=c_{11}n_1^2+c_{66}n_2^2+c_{55}q_r^2 & \Gamma_{12}&=\left(c_{12}+c_{66}\right)n_1n_2\\
\Gamma_{22}&=c_{66}n_1^2+c_{22}n_2^2+c_{44}q_r^2 & \Gamma_{13}&=\left(c_{13}+c_{55}\right)n_1q_r\\
\Gamma_{33}&=c_{55}n_1^2+c_{44}n_2^2+c_{33}q_r^2 & \Gamma_{23}&=\left(c_{23}+c_{44}\right)n_2q_r
\end{aligned}$$

Therefore, the secular equation of Christoffel equation is

$$\det\left(\Gamma_{il}-\delta_{il}\zeta\right)=0 \tag{6-3}$$

Where $\zeta=\rho V_R^2$ is the eigenvector of Γ_{il}. Chose eigenvector of Γ_{il}

$$\begin{pmatrix}\circ u_1^{(r)}\\ \circ u_2^{(r)}\\ \circ u_3^{(r)}\end{pmatrix}=\begin{pmatrix}p_r\\ s_r\\ 1\end{pmatrix}\ \textbf{where}\ (r=1,2,3)\textbf{, with}\ \begin{aligned}p_r&=\frac{\Gamma_{12}\left(\Gamma_{33}-\zeta\right)-\Gamma_{13}\Gamma_{23}}{\Gamma_{23}\left(\Gamma_{11}-\zeta\right)-\Gamma_{12}\Gamma_{23}}\\ s_r&=\frac{\left(\Gamma_{11}-\zeta\right)\left(\Gamma_{33}-\zeta\right)-\Gamma_{13}^2}{\Gamma_{12}\Gamma_{13}-\Gamma_{23}\left(\Gamma_{11}-\zeta\right)}\end{aligned} \tag{6-4}$$

Because the mechanical boundary condition that at $x_3=0$, $T_{i3}=\dfrac{\partial}{\partial x_k}\left(c_{i3kl}u_l\right)=0$ must be satisfied, for orthorhombic material, it could be represented in explicit form:

$$\begin{aligned}
T_{13}&=\frac{\partial}{\partial x_k}\left(c_{13kl}u_l\right)=c_{55}\left(\frac{\partial u_3}{\partial x_1}+\frac{\partial u_1}{\partial x_3}\right)=0\\
T_{23}&=\frac{\partial}{\partial x_k}\left(c_{23kl}u_l\right)=c_{44}\left(\frac{\partial u_3}{\partial x_2}+\frac{\partial u_2}{\partial x_3}\right)=0\\
T_{33}&=\frac{\partial}{\partial x_k}\left(c_{33kl}u_l\right)=2c_{13}\frac{\partial u_1}{\partial x_1}+2c_{23}\frac{\partial u_2}{\partial x_2}+2c_{33}\frac{\partial u_3}{\partial x_3}=0
\end{aligned} \tag{6-5}$$

And given the general form

$$\begin{aligned}
&\frac{\partial u_l}{\partial x_k}=n_kU_l\ \text{(when } k=1,2\text{), where } U_l(x_3)=\left(\sum_{r=1}^{3}A_r\circ u_l^{(r)}\exp(-ikq_rx_3)\right)\\
&\frac{\partial u_l}{\partial x_k}=W_l\ \text{(when } k=3\text{), where } W_l(x_3)=\left(\sum_{r=1}^{3}A_r\circ u_l^{(r)}q_r\exp(-ikq_rx_3)\right)
\end{aligned} \tag{6-6}$$

(6-5) can be simplified to polynomial equations.

$$
\begin{aligned}
&c_{55}\left(n_1U_3+W_1\right)=0\\
&c_{44}\left(n_2U_3+W_2\right)=0\\
&c_{13}n_1U_1+c_{23}n_2U_2+c_{33}W_3=0
\end{aligned}
\qquad \textbf{(6-7)}
$$

By substituting the eigenvector $\left(p_r \quad s_r \quad 1\right)^T$ in (6-6) to replace $\left(\circ u_1^{(r)} \quad \circ u_2^{(r)} \quad \circ u_3^{(r)}\right)^T$ and take $x_3=0$.

$$
\begin{aligned}
&U_1=A_1p_1+A_2p_2+A_3p_3 \quad && W_1=A_1p_1q_1+A_2p_2q_2+A_3p_3q_3\\
&U_2=A_1s_1+A_2s_2+A_3s_3 \quad && W_2=A_1s_1q_1+A_2s_2q_2+A_3s_3q_3\\
&U_3=A_1+A_2+A_3 \quad && W_3=A_1q_1+A_2q_2+A_3q_3
\end{aligned}
\qquad \textbf{(6-8)}
$$

Substitute (6-8) into (6-7), the boundary condition can be written as

$$
\begin{pmatrix}\Lambda_{11} & \Lambda_{12} & \Lambda_{13}\\ \Lambda_{21} & \Lambda_{22} & \Lambda_{23}\\ \Lambda_{31} & \Lambda_{32} & \Lambda_{33}\end{pmatrix}\begin{pmatrix}A_1\\A_2\\A_3\end{pmatrix}=0
\qquad \textbf{(6-9)}
$$

Where

$$
\begin{aligned}
&\Lambda_{11}=\left(n_1+p_1q_1\right) && \Lambda_{12}=\left(n_1+p_2q_2\right) && \Lambda_{13}=\left(n_1+p_3q_3\right)\\
&\Lambda_{21}=\left(n_2+s_1q_1\right) && \Lambda_{22}=\left(n_2+s_2q_2\right) && \Lambda_{23}=\left(n_3+s_3q_3\right)\\
&\Lambda_{31}=c_{13}n_1p_1+c_{23}n_2s_1+c_{33}q_1 && \Lambda_{32}=c_{13}n_1p_2+c_{23}n_2s_2+c_{33}q_2 && \Lambda_{33}=c_{13}n_1p_3+c_{23}n_2s_3+c_{33}q_3
\end{aligned}
$$

The secular equation for matrix $\mathbf{\Lambda}$ must be satisfied so that the boundary condition is satisfied:

$$
\det\left(\Lambda_{ij}\right)=0
\qquad \textbf{(6-10)}
$$

Similarly, for surface wave propagating along **XZ plane** (i.e. $\left(x_1,x_3\right)$ plane) on $\mathbf{n}$ direction where $n_1=\sin\phi, n_2=0, n_3=\cos\phi$ as shown in Fig. 6-3(a).

$$
\begin{aligned}
&\Gamma_{11}=c_{11}n_1^2+c_{66}q_r^2+c_{55}n_3^2 \quad && \Gamma_{12}=\left(c_{12}+c_{66}\right)n_1q_r\\
&\Gamma_{22}=c_{66}n_1^2+c_{22}q_r^2+c_{44}n_3^2 \quad && \Gamma_{13}=\left(c_{13}+c_{55}\right)n_1n_3\\
&\Gamma_{33}=c_{55}n_1^2+c_{44}q_r^2+c_{33}n_3^2 \quad && \Gamma_{23}=\left(c_{23}+c_{44}\right)q_rn_3
\end{aligned}
\qquad \textbf{(6-11)}
$$

$$T_{12} = \frac{\partial}{\partial x_k}\left(c_{12kl}u_l\right) = c_{66}\left(\frac{\partial u_2}{\partial x_1} + \frac{\partial u_1}{\partial x_2}\right) = 0$$
$$T_{22} = \frac{\partial}{\partial x_k}\left(c_{22kl}u_l\right) = 2c_{21}\frac{\partial u_1}{\partial x_1} + 2c_{22}\frac{\partial u_2}{\partial x_2} + 2c_{23}\frac{\partial u_3}{\partial x_3} = 0 \quad \textbf{at} \quad x_2 = 0 \qquad \textbf{(6-12)}$$
$$T_{32} = \frac{\partial}{\partial x_k}\left(c_{32kl}u_l\right) = c_{44}\left(\frac{\partial u_3}{\partial x_2} + \frac{\partial u_2}{\partial x_3}\right) = 0$$

$$\begin{aligned} &n_1U_2 + W_1 = 0 \\ &c_{21}n_1U_1 + c_{22}W_2 + c_{23}n_3U_3 = 0 \\ &W_3 + n_3U_2 = 0 \end{aligned} \qquad \textbf{(6-13)}$$

$$\begin{aligned} &\Lambda_{11} = n_1s_1 + p_1q_1 \quad &&\Lambda_{12} = n_1s_2 + p_2q_2 \quad &&\Lambda_{13} = n_1s_3 + p_3q_3 \\ &\Lambda_{21} = c_{12}n_1p_1 + c_{22}s_1q_1 + c_{23}n_3 \quad &&\Lambda_{22} = c_{12}n_1p_2 + c_{22}s_2q_2 + c_{23}n_3 \quad &&\Lambda_{23} = c_{12}n_1p_3 + c_{22}s_3q_3 + c_{23}n_3 \\ &\Lambda_{31} = q_1 + n_3s_1 \quad &&\Lambda_{32} = q_2 + n_3s_2 \quad &&\Lambda_{33} = q_3 + n_3s_3 \end{aligned} \qquad \textbf{(6-14)}$$

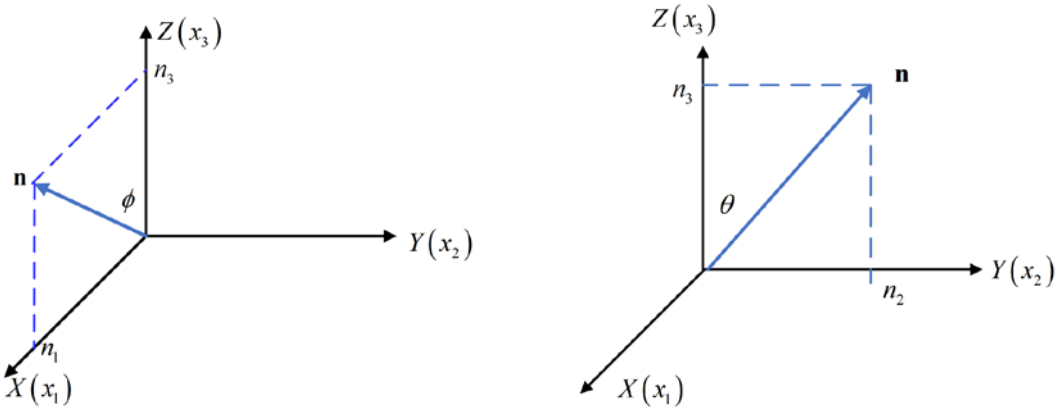

(a) (b)

Figure 6-3 XZ Plane and YZ Plane

For surface wave propagating along **YZ plane** (i.e. (x_2, x_3) plane) on **n** direction where $n_1 = 0, n_2 = \sin\theta, n_3 = \cos\theta$ as shown in Fig. 6-3(b).

$$\begin{aligned} &\Gamma_{11} = c_{11}q_r^2 + c_{66}n_2^2 + c_{55}n_3^2 \quad &&\Gamma_{12} = (c_{12} + c_{66})q_rn_2 \\ &\Gamma_{22} = c_{66}q_r^2 + c_{22}n_2^2 + c_{44}n_3^2 \quad &&\Gamma_{13} = (c_{13} + c_{55})q_rn_3 \\ &\Gamma_{33} = c_{55}q_r^2 + c_{44}n_2^2 + c_{33}n_3^2 \quad &&\Gamma_{23} = (c_{23} + c_{44})n_2n_3 \end{aligned} \qquad \textbf{(6-15)}$$

$$T_{11} = \frac{\partial}{\partial x_k}\left(c_{11kl}u_l\right) = 2c_{11}\frac{\partial u_1}{\partial x_1} + 2c_{12}\frac{\partial u_2}{\partial x_2} + 2c_{13}\frac{\partial u_3}{\partial x_3} = 0$$

$$T_{21} = \frac{\partial}{\partial x_k}\left(c_{21kl}u_l\right) = c_{66}\left(\frac{\partial u_2}{\partial x_1} + \frac{\partial u_1}{\partial x_2}\right) = 0 \qquad \textbf{at } x_1 = 0 \qquad \textbf{(6-16)}$$

$$T_{31} = \frac{\partial}{\partial x_k}\left(c_{31kl}u_l\right) = c_{55}\left(\frac{\partial u_3}{\partial x_1} + \frac{\partial u_1}{\partial x_3}\right) = 0$$

$$\begin{aligned} &c_{11}W_1 + c_{12}n_2U_2 + c_{13}n_3U_3 = 0 \\ &W_2 + n_2U_1 = 0 \\ &W_3 + n_3U_1 = 0 \end{aligned} \qquad \textbf{(6-17)}$$

$$\begin{aligned} &\Lambda_{11} = c_{11}p_1q_1 + c_{12}n_2s_1 + c_{13}n_3 \quad \Lambda_{12} = c_{11}p_2q_2 + c_{12}n_2s_2 + c_{13}n_3 \quad \Lambda_{13} = c_{11}p_3q_3 + c_{12}n_2s_3 + c_{13}n_3 \\ &\Lambda_{21} = s_1q_1 + n_2p_1 \quad \Lambda_{22} = s_2q_2 + n_2p_2 \quad \Lambda_{23} = s_3q_3 + n_2p_3 \\ &\Lambda_{31} = q_1 + n_3p_1 \quad \Lambda_{32} = q_2 + n_3p_2 \quad \Lambda_{33} = q_3 + n_3p_3 \end{aligned} \qquad \textbf{(6-18)}$$

6.2.2 Crystallographic Axis

Consider the surface wave propagating on **XY-plane**

X direction $n_1 = 1$ and $n_2 = 0$

$$\begin{aligned} &\Gamma_{11} = c_{11} + c_{55}q_r^2 \quad \Gamma_{12} = 0 \\ &\Gamma_{22} = c_{66} + c_{44}q_r^2 \quad \Gamma_{13} = \left(c_{13} + c_{55}\right)q_r \\ &\Gamma_{33} = c_{55} + c_{33}q_r^2 \quad \Gamma_{23} = 0 \end{aligned} \qquad \textbf{(6-19)}$$

$$\begin{bmatrix} \Gamma_{11} - \zeta_{R-X} & \Gamma_{13} \\ \Gamma_{13} & \Gamma_{33} - \zeta_{R-X} \end{bmatrix}\begin{pmatrix} {}^{\circ}u_1 \\ {}^{\circ}u_3 \end{pmatrix} = 0 \qquad \textbf{(6-20)}$$

The secular equation from Christoffel equation is

$$\left(c_{11} + c_{55}q_r^2 - \zeta_{R-X}\right)\left(c_{55} + c_{33}q_r^2 - \zeta_{R-X}\right) - \left(\left(c_{13} + c_{55}\right)q_r\right)^2 = 0 \qquad \textbf{(6-21)}$$

$$\begin{pmatrix} {}^{\circ}u_1^{(r)} \\ {}^{\circ}u_2^{(r)} \\ {}^{\circ}u_3^{(r)} \end{pmatrix} = \begin{pmatrix} p_r \\ 0 \\ 1 \end{pmatrix} \quad \textbf{where } (r = 1, 2)\textbf{, with } \quad p_r = \frac{-\Gamma_{13}}{\Gamma_{11}} \qquad \textbf{(6-22)}$$

$$U_3 + W_1 = 0$$
$$c_{13}U_1 + c_{33}W_3 = 0 \qquad \textbf{(6-23)}$$

$$\begin{bmatrix} 1+p_1q_1 & 1+p_2q_2 \\ c_{13}p_1 + c_{33}q_1 & c_{13}p_2 + c_{33}q_2 \end{bmatrix}\begin{pmatrix} A_1 \\ A_2 \end{pmatrix} = 0 \qquad \textbf{(6-24)}$$

The secular equation from boundary condition is

$$(1+p_1q_1)(c_{13}p_2 + c_{33}q_2) - (1+p_2q_2)(c_{13}p_1 + c_{33}q_1) = 0 \qquad \textbf{(6-25)}$$

Y direction $n_1 = 0$ and $n_2 = 1$

$$\begin{aligned} \Gamma_{11} &= c_{66} + c_{55}q_r^2 & \Gamma_{12} &= 0 \\ \Gamma_{22} &= c_{22} + c_{44}q_r^2 & \Gamma_{13} &= 0 \\ \Gamma_{33} &= c_{44} + c_{33}q_r^2 & \Gamma_{23} &= (c_{23} + c_{44})q_r \end{aligned} \qquad \textbf{(6-26)}$$

$$\begin{bmatrix} \Gamma_{22} - \zeta_{R-Y} & \Gamma_{23} \\ \Gamma_{23} & \Gamma_{33} - \zeta_{R-Y} \end{bmatrix}\begin{pmatrix} {}^{\circ}u_2 \\ {}^{\circ}u_3 \end{pmatrix} = 0 \qquad \textbf{(6-27)}$$

The secular equation from Christoffel equation is

$$\left(c_{22} + c_{44}q_r^2 - \zeta_{R-Y}\right)\left(c_{44} + c_{33}q_r^2 - \zeta_{R-Y}\right) - \left((c_{23} + c_{44})q_r\right)^2 = 0 \qquad \textbf{(6-28)}$$

$$\begin{pmatrix} {}^{\circ}u_1^{(r)} \\ {}^{\circ}u_2^{(r)} \\ {}^{\circ}u_3^{(r)} \end{pmatrix} = \begin{pmatrix} 0 \\ p_r \\ 1 \end{pmatrix} \quad \textbf{where } (r = 1,2)\textbf{, with} \quad p_r = \frac{-\Gamma_{23}}{\Gamma_{22}} \qquad \textbf{(6-29)}$$

$$U_3 + W_2 = 0$$
$$c_{23}U_2 + c_{33}W_3 = 0 \qquad \textbf{(6-30)}$$

$$\begin{bmatrix} 1+p_1q_1 & 1+p_2q_2 \\ c_{23}p_1 + c_{33}q_1 & c_{23}p_2 + c_{33}q_2 \end{bmatrix}\begin{pmatrix} A_1 \\ A_2 \end{pmatrix} = 0 \qquad \textbf{(6-31)}$$

The secular equation from boundary condition is

$$(1+p_1q_1)(c_{23}p_2 + c_{33}q_2) - (1+p_2q_2)(c_{23}p_1 + c_{33}q_1) = 0 \qquad \textbf{(6-32)}$$

Consider the surface wave propagating on **XZ-plane**

Z direction $n_1 = 0$ and $n_3 = 1$

$$\begin{aligned} \Gamma_{11} &= c_{66}q_r^2 + c_{55} \quad \Gamma_{12} = 0 \\ \Gamma_{22} &= c_{22}q_r^2 + c_{44} \quad \Gamma_{13} = 0 \\ \Gamma_{33} &= c_{44}q_r^2 + c_{33} \quad \Gamma_{23} = (c_{23} + c_{44})q_r \end{aligned} \tag{6-33}$$

$$\begin{bmatrix} \Gamma_{22} - \zeta_{R-Z} & \Gamma_{23} \\ \Gamma_{23} & \Gamma_{33} - \zeta_{R-Z} \end{bmatrix} \begin{pmatrix} {}^{\circ}u_2 \\ {}^{\circ}u_3 \end{pmatrix} = 0 \tag{6-34}$$

The secular equation from Christoffel equation is:

$$\left(c_{22}q_r^2 + c_{44} - \zeta_{R-Z}\right)\left(c_{44}q_r^2 + c_{33} - \zeta_{R-Z}\right) - \left(\left(c_{23} + c_{44}\right)q_r\right)^2 = 0 \tag{6-35}$$

$$\begin{pmatrix} {}^{\circ}u_1^{(r)} \\ {}^{\circ}u_2^{(r)} \\ {}^{\circ}u_3^{(r)} \end{pmatrix} = \begin{pmatrix} 0 \\ 1 \\ p_r \end{pmatrix} \quad \textbf{where } (r = 1, 2)\textbf{, with} \quad p_r = \frac{-\Gamma_{22}}{\Gamma_{23}} \tag{6-36}$$

$$\begin{aligned} c_{22}W_2 + c_{23}U_3 &= 0 \\ W_3 + U_2 &= 0 \end{aligned} \tag{6-37}$$

$$\begin{bmatrix} c_{22}q_1 + c_{23}p_1 & c_{22}q_2 + c_{23}p_2 \\ p_1q_1 + 1 & p_2q_2 + 1 \end{bmatrix} \begin{pmatrix} A_1 \\ A_2 \end{pmatrix} = 0 \tag{6-38}$$

The secular equation from boundary condition is:

$$\left(c_{22}q_1 + c_{23}p_1\right)\left(p_2q_2 + 1\right) - \left(c_{22}q_2 + c_{23}p_2\right)\left(p_1q_1 + 1\right) = 0 \tag{6-39}$$

6.3 Discussions

The velocity equations of bulk waves that propagate along X, Y and Z directions of orthorhombic solid are derived by solving the eigenvalues of the Christoffel tensor with given stiffness matrix and wave propagation direction. On each wave propagation direction, there exist

three eigenvalues, which correspond to the propagation velocities of one longitudinal bulk wave and two transverse bulk waves. Each eigenvalue has one corresponding eigenvector which represents the polarization direction of the wave. For wave propagating on the crystallographic axes, based on the definition of bulk waves, the polarization direction of longitudinal bulk wave is on the same direction of the wave propagation direction and the polarization direction of transverse wave is orthogonal to the propagation direction, whether a wave is longitudinal mode or transverse mode can be identified. The propagation velocity is in a function of material density and stiffness constants, and this relationship, which is also commonly referred as velocity equation, enables the calculation of propagation velocity of bulk wave on specific direction when the material has a given stiffness constants, or the inverse formula can be used to characterize the stiffness constants with measured velocities. However, the velocities of longitudinal and transverse waves propagating on X, Y and Z direction are not sufficient to solve all the stiffness constants of orthorhombic material, and the bulk wave propagating on other non-crystallographic directions are not practical for traditional bulk wave ultrasound transducers, ultrasound method is rarely used for material characterization of orthorhombic materials.

Based on the theoretical study of cubic and trigonal materials, it is possible and very useful to develop a more generalized procedure for deriving the mechanistic model for Rayleigh surface wave propagating along any direction within an anisotropic material. This process is expected to provide a guideline for the derivation for Christoffel tensor Γ_{il} and boundary condition tensor Λ_{ij} . Using this general process, the mechanistic model for Rayleigh wave propagating on crystallographic planes (i.e. XY-plane, XZ-plane and YZ-plane) are derived as presented in section 6.2.1. As the eigenvectors of the Christoffel equations in the three planes do not include zero term (shown in equation 6-4), which indicates that the particle in the Rayleigh wave has movement on

three directions and the polarization plane is inclined to sagittal plane. For the Rayleigh wave propagates on X, Y and Z directions, they are the special cases from the model developed for crystallographic planes, and therefore easily developed as being presented in section 6.2.2, the model is significantly simplified. Additionally, it is found that the particle polarization plane is parallel to the sagittal plane, which is similar with the propagation character of isotropic material and (100) direction of cubic material.

Based on the model development and theoretical study, it is feasible to characterize an orthorhombic solid with line-focus transducer by measuring longitudinal bulk wave and Rayleigh surface wave. In order to minimize the calculation complexity, the longitudinal bulk waves and Rayleigh waves on X, Y and Z direction, together with three other Raleigh waves from XY, XZ and YZ planes can be employed to solve the 9 independent stiffness constants based on the 9 wave propagation equations and corresponding velocity measurements. If a cubic shaped specimen with X-cut (or either Y or Z cut) is available, these 9 measurements can be achieved through 6 measurement using one sample. Compared to conventional approach, this provides a simplified and promising material characterization method for industrial applications.

Based on the model developed in sections 6.1 and 6.2, the wave propagation velocities can be predicted for a material with given stiffness constants. For Barium sodium niobate ($Ba_2NaNb_5O_{15}$), using the stiffness constants and density, velocities can be calculated. Given the stiffness ($10^{10}N/m^2$) and density (kg/m^3):

$$\begin{array}{lll} c_{11}=23.9 & c_{12}=10.4 & c_{13}=5 \\ c_{22}=24.7 & c_{23}=5.2 & c_{33}=13.5 \text{ and } \rho=5300 \text{ [1]} \\ c_{44}=6.5 & c_{55}=6.6 & c_{66}=7.6 \end{array}$$

The velocities (m/s) of the longitudinal waves propagating on X, Y and Z directions, Rayleigh wave on X, Y and Z directions and three Rayleigh waves propagating on XY, XZ and YZ planes which is 45 degree from the crystallographic axis are calculated and summarized below:

$$\begin{array}{ccc} V_{L-X}=6715 & V_{L-Y}=6827 & V_{L-Z}=5047 \\ V_{R-X}=3250 & V_{R-Y}=3230 & V_{R-Z}=3328 \\ V_{R-XY\,45}=2658 & V_{R-XZ\,45}=3372 & V_{R-YZ\,45}=3451 \end{array}$$

The calculated velocities can be validated experimentally in further research.

The model developed for orthorhombic materials can also be used for Tetragonal materials with 422, 4mm and 4/mmm structure which is a special case of orthorhombic material and have a stiffness matrix:

$$\left(c_{\alpha\beta}\right)=\left(c_{pqrs}\right)=\begin{pmatrix} c_{11} & c_{12} & c_{13} & 0 & 0 & 0 \\ c_{12} & c_{11} & c_{13} & 0 & 0 & 0 \\ c_{13} & c_{13} & c_{33} & 0 & 0 & 0 \\ 0 & 0 & 0 & c_{44} & 0 & 0 \\ 0 & 0 & 0 & 0 & c_{44} & 0 \\ 0 & 0 & 0 & 0 & 0 & c_{66} \end{pmatrix} \quad \textbf{(6-40)}$$

The stiffness $c_{22}=c_{11}$, $c_{23}=c_{13}$ and $c_{55}=c_{44}$ reduces the independent stiffness to six. Take single crystal Barium titanate ($BaTiO_3$) as example which belong to 4mm class and have stiffness constants ($10^{10}N/m^2$) and density (kg/m^3) given:

$$\begin{array}{ccc} c_{11}=27.5 & c_{12}=17.9 & c_{13}=15.2 \\ c_{33}=16.5 & c_{55}=5.43 & c_{66}=11.3 \end{array} \text{ and } \rho=6020 \text{ [1]}$$

The velocities (m/s) of the longitudinal waves propagating on X, Y and Z directions, Rayleigh wave on X, Y and Z directions are calculated and summarized below:

$$\begin{array}{ccc} V_{L-X}=6759 & V_{L-Y}=6759 & V_{L-Z}=5235 \\ V_{R-X}=2905 & V_{R-Y}=2905 & V_{R-Z}=2700 \end{array}$$

6.4 Summary

The mechanistic models for Rayleigh wave propagating on crystallographic axes and non-crystallographic axes on crystal plane are established based on the general derivation process summarized from the study in chapter 4 and 5. The models have the capability to characterize orthorhombic solid with the 9 independent stiffness constants by 6 velocity measurements on a single sample by line-focus ultrasound transducer. The particle polarization character is also investigated through the theoretical study without solving the wave equation. Since orthorhombic crystals are not easily accessible, the model developed are not validated. However, based on the numerical and experimental study from the previous two chapters, the model is expected to give good prediction on Rayleigh wave velocities with given stiffness constants, and the model can also be used for stiffness constants with reasonable accuracy by measuring longitudinal bulk wave and Rayleigh surface wave velocities with a single transducer.

7.0 Conclusion Remarks and Future Work

This dissertation presents the development and validation of a novel anisotropic material elastic stiffness constant characterization method based on the simultaneous measurement of Rayleigh surface wave velocity and longitudinal bulk wave velocity by using a lens-less line-focus PVDF piezoelectric transducer. Mechanistic mathematical models that analytically describe the relationship of Rayleigh surface wave and stiffness constants of cubic, trigonal and orthorhombic materials are developed through systematic theoretical analysis. The models are also validated through numerical and experimental studies.

Firstly, the line-focus ultrasound transducer and the corresponding ultrasound testing system were established and calibrated by using metal alloys which are typical isotropic materials with well-developed mathematical relationship between Rayleigh surface wave velocity, bulk wave velocities and elastic constants. In order to further apply the line-focus ultrasound transducer to characterize the stiffness constants of anisotropic materials, the mathematical mechanistic model must be developed.

Secondly, the mechanistic model for Rayleigh wave propagating in cubic and trigonal material is developed and validated. Based on the fundamental theory of acoustic wave in anisotropic solid, the propagating and particle movement of Rayleigh surface wave can be described using wave equation and stress-free boundary condition on the propagation plane. Therefore, the mechanistic model is developed based on wave equation and boundary condition. The model is first developed for anisotropic solid with cubic structure. Cubic material has a highly symmetric structure, and the number of independent stiffness constants is three, which is the simplest form among all anisotropic materials. The Rayleigh wave propagation directions within

an anisotropic material can be characterized as two categories: propagation on crystallographic planes, and propagation on non-crystallographic planes. The propagation on crystallographic planes has the special case when the wave propagates along crystallographic axes. Although the mathematical model of wave on crystallographic axes of cubic material is available from literature, the significance of the work in this dissertation is to develop the model from a more general point of view i.e. the wave propagating on crystallographic planes, which has rarely been found in literature. By proposing a more generalized form of the solution for wave equations, it is possible to conduct theoretical study on waves propagating on more directions of an anisotropic solid. In this dissertation, the model for (100), (110) and (111) directions of cubic material are specifically presented as examples for wave on crystallographic axes, special direction on non-crystallographic plane and regular direction on non-crystallographic plane. The model is validated by numerically calculating the Rayleigh wave velocities of single crystal Silicon, an easily accessible cubic crystal with fully characterized material property and using stiffness constants obtained from literature. The predicted velocity is compared with the velocities measured by using line-focus ultrasound transducer. The good agreement between the predicted velocities and the experiment velocities validates that the developed model accurately describes the relationship between a Rayleigh surface wave propagation velocity and the stiffness constants.

The experiment results also demonstrate the existence of pseudo-Rayleigh surface wave which travels faster than Rayleigh surface wave and some transverse bulk waves. In some measurement planes (i.e. [110] direction on (110) plane), instead of Rayleigh wave, the pseudo-Rayleigh wave is excited and captured during the measurement. The presence of pseudo-Rayleigh wave can also be well explained using the analytical model developed from this research. As one of the three decay constants is a real number, pseudo-Rayleigh wave penetrates deeper in to the

solid comparing to Rayleigh surface wave, which mathematically explains the physical phenomenon that pseudo-Rayleigh wave has a higher propagation velocity. This shows that the mechanistic model has the capability of solving for both regular Rayleigh wave and pseudo-Rayleigh wave which corresponds to the other set of the solution of the model.

From the theoretical study on cubic material, it is also found that the model that describes the relationship between stiffness constants and Rayleigh wave velocity is much more complicated than the velocity equation that relates stiffness constants and bulk waves. If the primary purpose is to characterize the stiffness constants, it is not always necessary to develop the model when Rayleigh surface wave propagates on non-crystallographic planes. For the propagation on crystallographic plane, the crystallographic coordinate system (X, Y, Z) and particle displacement coordinate system (x_1, x_2, x_3) coincide, so that c_{pqrs} equals to c'_{ijkl} without concerning about the rotation of axes. Therefore, the model development of Trigonal material focuses on two crystallographic planes XZ-plane and XY-plane, and then the model is obtained for the wave propagation on X, Y and Z crystallographic axes. Quartz as an example is used for model validation. The experiment results show the almost same Rayleigh wave velocities propagating on X, Y and Z directions irrespective of being measured from XY-plane (Z-cut), XZ-plane (Y-cut) or YZ-plane (X-cut). Additionally, the measured velocity well matches with the model prediction on Rayleigh wave. This verifies that these Rayleigh waves are in the regular Rayleigh mode.

More importantly, the application of the developed mechanistic model on stiffness constant characterization is studied and summarized. For cubic materials, two specific characterization approaches are proposed, and the stiffness constants characterized from both approaches are very close to the references from literature. Due to the lack of symmetry and the mirror planes in Trigonal structure, there are total eighteen stiffness constants six of which are independent, and

therefore this requires the measurement six velocities to make the model solvable. Benefit from the low symmetry, different analytical models are obtained from X, Y and Z directions. The models for Rayleigh surface waves together with the three longitudinal wave equations on the X, Y and Z direction, the stiffness constants can be solved. Using line-focus transducer can obtain the six independent velocity measurements from three testing of the three sample cuts. This measurement approach uses fewer transducers compared to traditional ultrasound method, and half of the sample type and cuts compared to resonate method. The results indicate that the three stiffness constants evaluated based on longitudinal velocity well agree with the ones from reference. Although two of other three stiffness that are calculated using the Rayleigh wave velocity exhibit greater deviation, it is still within a reasonable range. Considering the measurement simplicity of the new approach, it is still a promising method to characterize stiffness constants for industrial application where the efficiency and cost are also critical factors.

Finally, a generalized mechanistic model development process is developed, and is used to derive the model for Rayleigh wave propagating in orthorhombic materials which has 9 independent stiffness constants. The models for Rayleigh wave propagating on XY, YZ, and XZ plane are developed, based on which the special case when propagating on X, Y and Z directions are also obtained. For the purpose of stiffness constant characterization using line-focus ultrasound transducer, if longitudinal bulk waves and Rayleigh waves on X, Y and Z directions are used, and chose three directions from XY, YZ or XZ plane, the 9 independent stiffness constants can be characterized. If a sample is in cubic shaped edges on X, Y and Z direction, all the velocities can be measured from one sample and as few as six measurements.

Overall, the significance of this research work is to utilize the Rayleigh surface wave in supplemental with longitudinal bulk wave to characterize the stiffness constants of low symmetry

anisotropic solid. Taking the advantage of line-focus ultrasound transducer that can easily generate Rayleigh surface wave on different directions on a solid surface, the measurement is largely simplified by using fewer sample cuts, single transducer, and easy data process procedure. The finding of this dissertation demonstrates the capability of the line-focus ultrasound transducer and its promising wide application on stiffness constant characterization of anisotropic solids.

Appendix A General Christoffel Equation

This section presents the derivation of general Christoffel's equation that is valid for elastic waves in crystals regardless of crystal type and wave propagation direction.

The wave equation of solid with mass density ρ, stiffness constants c'_{ijkl} defined in coordinate x_k, and particle displacement $u_i = u_i\left(t, x_j\right)$ is given as

$$\rho \frac{\partial^2 u_i}{\partial t^2} = c'_{ijkl} \frac{\partial^2 u_l}{\partial x_j \partial x_k} \quad \textbf{(A 1)}$$

where c'_{ijkl} are obtained from c_{ijkl}, which is defined in the crystallographic reference frame *XYZ*, using the transformation matrix.

Assume the particle displacement can be expressed as a function of phase velocity V, wave number k, time t, propagation unit vector $\mathbf{l} = \left(l_1, l_2, l_3\right)$, and coordinate x_k:

$$u_l = {}^{\circ}u_l F(t, x_1, x_2, x_3) = {}^{\circ}u_l F\left(\left(ik\right)\left(Vt - l_j x_j\right)\right) \quad \textbf{(A 2)}$$

Substitute (A2) into (A1) on the left side:

$$\rho \frac{\partial^2 u_i}{\partial t^2} = \rho\left(ikV\right)^2 F''\,{}^{\circ}u_i \quad \textbf{(A 3)}$$

Similarly, on the right side of (A1), there is

$$c'_{ijkl} \frac{\partial^2 u_l}{\partial x_j \partial x_k} = c'_{ijkl}\, l_j l_k\, {}^{\circ}u_l \left(ik\right)^2 F'' \quad \textbf{(A 4)}$$

Therefore, the wave equation is transformed to Christoffel equation:

$$\rho V^2\, {}^{\circ}u_i = c'_{ijkl}\, l_j l_k\, {}^{\circ}u_l \quad \textbf{(A 5)}$$

(A5) can be also written as

$$\zeta \circ u_i = \Gamma_{il} \circ u_l \qquad \textbf{(A 6)}$$

where $\circ u_i$ is the wave polarization which is a constant independent of x_k and t, $\zeta = \rho V^2$ and $\Gamma_{il} = c'_{ijkl} l_j l_k$ is the Christoffel tensor, which has six components:

$$\begin{aligned}
\Gamma_{11} &= c_{11}l_1^2 + c_{66}l_2^2 + c_{55}l_3^2 + 2c_{16}l_1l_2 + 2c_{15}l_1l_3 + 2c_{56}l_2l_3 \\
\Gamma_{22} &= c_{66}l_1^2 + c_{22}l_2^2 + c_{44}l_3^2 + 2c_{26}l_1l_2 + 2c_{46}l_1l_3 + 2c_{24}l_2l_3 \\
\Gamma_{33} &= c_{55}l_1^2 + c_{44}l_2^2 + c_{33}l_3^2 + 2c_{45}l_1l_2 + 2c_{35}l_1l_3 + 2c_{34}l_2l_3 \\
\Gamma_{12} &= c_{16}l_1^2 + c_{26}l_2^2 + c_{45}l_3^2 + (c_{12} + c_{66})l_1l_2 + (c_{14} + c_{56})l_1l_3 + (c_{46} + c_{25})l_2l_3 \\
\Gamma_{13} &= c_{15}l_1^2 + c_{46}l_2^2 + c_{35}l_3^2 + (c_{14} + c_{56})l_1l_2 + (c_{13} + c_{55})l_1l_3 + (c_{36} + c_{45})l_2l_3 \\
\Gamma_{23} &= c_{56}l_1^2 + c_{24}l_2^2 + c_{34}l_3^2 + (c_{46} + c_{25})l_1l_2 + (c_{36} + c_{45})l_1l_3 + (c_{23} + c_{44})l_2l_3
\end{aligned} \qquad \textbf{(A 7)}$$

and $\Gamma_{21} = \Gamma_{12}$, $\Gamma_{31} = \Gamma_{13}$, and $\Gamma_{32} = \Gamma_{23}$.

Appendix B MATLAB Program

1. Simplicity Method to calculate Rayleigh velocity propagating on [111] direction on (110) plane of Silicon

```
syms rou a q

for vr=4.5:0.02:6
% vr=4.629;
rou=0.2329;
a=rou*vr^2;

%Original Stiffness Matrix
% const=10^10;
const=1;
c11=16.65*const;
c12=6.39*const;
c66=7.95*const;

%Rotated Stiffness
c11_3=(c11+c12)/2+c66;
c12_3=(c11+c12)/2-c66;
c13_3=c12;
c33_3=c11;
c44_3=c66;
c66_3=(c11-c12)/2;

angle=35.26;
%propagation direction
n1=cosd(angle);
n3=sind(angle);
% n1=1;
% n3=0;

%Christoffel Matrix
T11=c11_3*n1^2+c66_3*q^2+c44_3*n3^2; %Create T11_1, T11_2, T11_3,
Access by T11(1),T11(2),T11(3)
T22=c66_3*n1^2+c11_3*q^2+c44_3*n3^2;
T33=c44_3*n1^2+c44_3*q^2+c11_3*n3^2;
T12=(c12_3+c66_3)*n1*q;
T13=(c13_3+c44_3)*n1*n3;
T23=(c13_3+c44_3)*n3*q;

%Secular Equation for Governing Eqn
secular=(T11-a)*(T22-a)*(T33-a)+2*T12*T13*T23-(T22-a)*T13^2-(T11-
a)*T23^2-(T33-a)*T12^2;
```

```
%Solve q
qq=solve(secular,q);
qqq=vpa(qq);

% qimag=imag(qqq);
qb=qqq(1:3);
% qc=qimag<0;
% qb=qqq(qc); %qb must have 3 values

% s_qb=size(qb);% if size=2, continue to boundary condition
%
% if s_qb<3
%     bcsreal=100;
%     bcsimag=100;
% else

%New Christoffel matrix
mb11=c11_3*n1^2+c66_3*qb.^2+c44_3*n3^2; %Create T11_1, T11_2, T11_3,
Access by T11(1),T11(2),T11(3)
% mb22=c66_3*n1^2+c11_3*qb.^2+c44_3*n3^2;
mb33=c44_3*n1^2+c44_3*qb.^2+c11_3*n3^2;
mb12=(c12_3+c66_3)*n1*qb;
mb13=(c13_3+c44_3)*n1*n3;
mb23=(c13_3+c44_3)*n3*qb;

%eigen vector
p=(mb12.*(mb33-a)-mb13.*mb23)./(mb23.*(mb11-a)-mb12.*mb23);
s=((mb11-a).*(mb33-a)-mb13^2)./(mb12.*mb13-mb23.*(mb11-a));


b11=c12_3*n1*p(1)+c11_3*qb(1)*s(1)+c13_3*n3;
b12=c12_3*n1*p(2)+c11_3*qb(2)*s(2)+c13_3*n3;
b13=c12_3*n1*p(3)+c11_3*qb(3)*s(3)+c13_3*n3;
b21=n3*s(1)+qb(1);
b22=n3*s(2)+qb(2);
b23=n3*s(3)+qb(3);
b31=p(1)*qb(1)+n1*s(1);
b32=p(2)*qb(2)+n1*s(2);
b33=p(3)*qb(3)+n1*s(3);

bcsecular=b11*b22*b33+b31*b12*b23+b21*b32*b13-b13*b22*b31-b33*b21*b12-
b11*b32*b23;
bcabs=abs(bcsecular);
% bcsreal=real(bcsecular);
% bcsimag=imag(bcsecular);

% end
hold on
plot(vr,bcabs,'*')
% plot(vr,bcsreal,'*')
% axis([0 10 -50 50])
% plot(vr,bcsimag,'o')
```

```
% axis([0 10 -50 50])
end
hold off
```

2. Simplicity Method to calculate Rayleigh velocity propagating on Y-direction of Trigonal material -Quartz

```
syms rou a q vr

for vr=2.5:0.05:4
% vr=3.1;
rou=0.2648;
a=rou*vr^2;

%Original Stiffness Matrix
% const=10^10;
const=1;

c11=8.67*const; %stiffness when const=10^10 N/m2
c12=0.7*const;
c13=1.19*const;
c14=-1.79*const;
c33=10.72*const;
c44=5.79*const;
c66=(c11-c12)/2;


%Christoffel Matrix
T11=c11+c44*q^2-2*c14*q; %Create T11_1, T11_2, T11_3, Access by
T11(1),T11(2),T11(3)
T22=c44+c33*q^2;
T12=-c14+(c13+c44)*q;


%Secular Equation for Governing Eqn
secular=(T11-a)*(T22-a)-T12^2;

%Solve q
qq=solve(secular,q);
qqq=vpa(qq);

qimag=imag(qqq);
% qb=qqq(1:2);
qc=qimag<0;
qb=qqq(qc); %qb must have 3 values

%New Christoffel matrix
mb11=c11+c44*qb.^2-2*c14*qb;
mb22=c44+c33*qb.^2;
```

```
mb12=-c14+(c13+c44)*qb;

%eigen vector
s=-mb12./(mb11-a);

%Boundary condition
b11=-c14*s(1)+c44*(1+s(1)*qb(1));
b12=-c14*s(2)+c44*(1+s(2)*qb(2));
b21=c13*s(1)+c33*qb(1);
b22=c13*s(2)+c33*qb(2);

bc_secular=b11*b22-b12*b21;
bc_abs=abs(bc_secular);
% bcsreal=real(bcsecular);
% bcsimag=imag(bcsecular);

% end
hold on
plot(vr,bc_abs,'*')
% plot(vr,bcsreal,'*')
% axis([0 10 -50 50])
% plot(vr,bcsimag,'o')
% axis([0 10 -50 50])
end
hold off
```

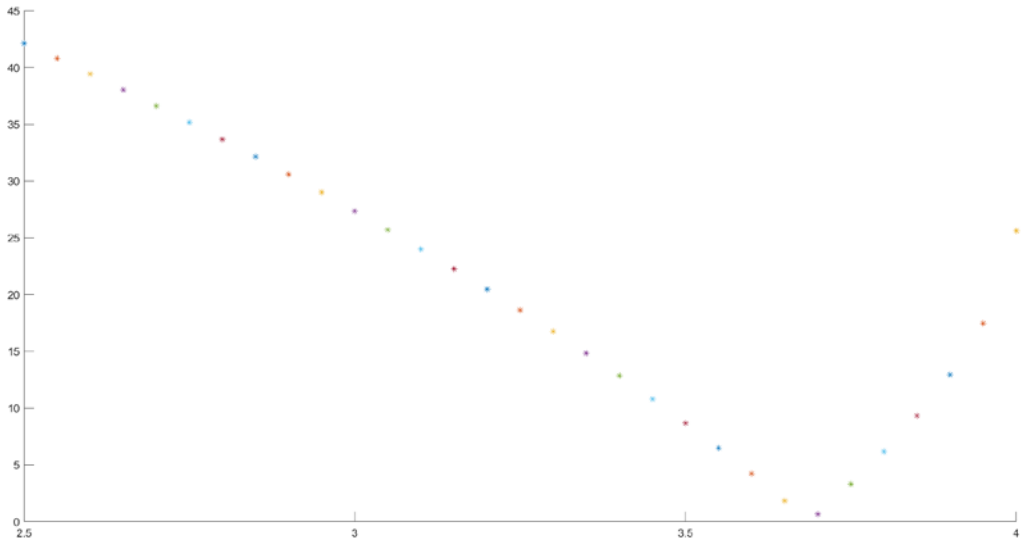

3. Simplicity Method to calculate Rayleigh surface wave velocity propagating on Z direction of Trigonal material – Quartz

```
syms rou a q vr

for vr=2.5:0.05:4
% vr=3.1;
rou=0.2648;
a=rou*vr^2;

%Origional Stiffness Matrix
% const=10^10;
const=1;

c11=8.67*const; %stiffness when const=10^10 N/m2
c12=0.7*const;
c13=1.19*const;
c14=-1.79*const;
c33=10.72*const;
c44=5.79*const;
c66=(c11-c12)/2;


%Christoffel Matrix
T11=c11*q^2+c44-2*c14*q; %Create T11_1, T11_2, T11_3, Access by
T11(1),T11(2),T11(3)
T22=c44*q^2+c33;
T12=-c14*q^2+(c13+c44)*q;


%Secular Equation for Governing Eqn
secular=(T11-a)*(T22-a)-T12^2;

%Solve q
qq=solve(secular,q);
qqq=vpa(qq);

qimag=imag(qqq);
% qb=qqq(1:2);
qc=qimag<0;
qb=qqq(qc); %qb must have 3 values

%New Christoffel matrix
mb11=c11*qb.^2+c44-2*c14*qb;
mb22=c44*qb.^2+c33;
mb12=-c14*qb.^2+(c13+c44)*qb;

%eigen vector
s=-mb12./(mb11-a);

%Boundary condition
```

```
b11=c11*s(1)*qb(1)-c14*qb(1)-c14*s(1)+c13;
b12=c11*s(2)*qb(2)-c14*qb(2)-c14*s(2)+c13;
b21=-c14*s(1)*qb(1)+c44*(qb(1)+s(1));
b22=-c14*s(2)*qb(2)+c44*(qb(2)+s(2));

bc_secular=b11*b22-b12*b21;
bc_abs=abs(bc_secular);
% bcsreal=real(bcsecular);
% bcsimag=imag(bcsecular);

% end
hold on
plot(vr,bc_abs,'*')
% plot(vr,bcsreal,'*')
% axis([0 10 -50 50])
% plot(vr,bcsimag,'o')
% axis([0 10 -50 50])
end
hold off
```

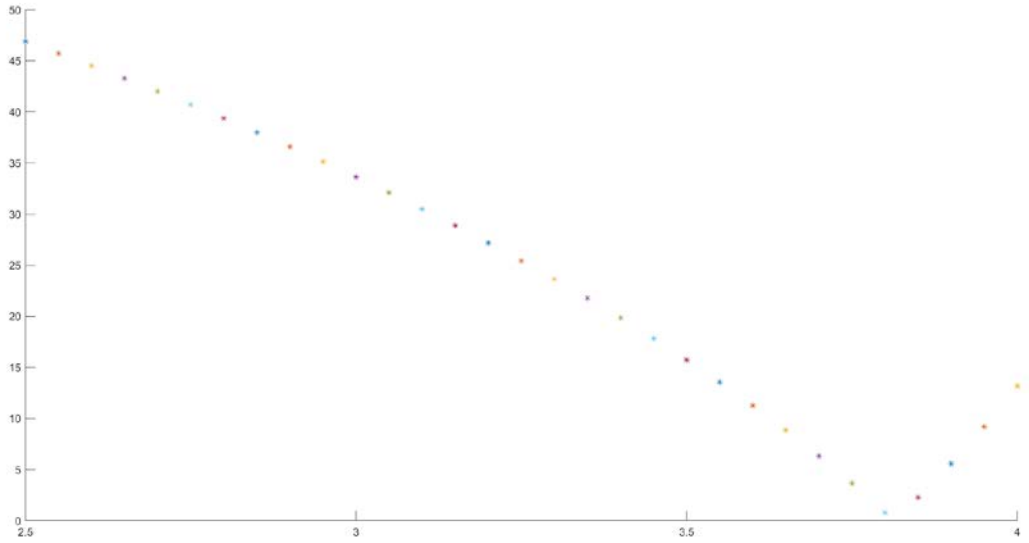

Appendix C Experimental V(z,t) and Z(t) plots of Quartz

As the experimental measurement of longitudinal bulk wave and Rayleigh surface wave of quartz is similar with metal alloys and silicon, selected V(z,t) curves and Z(t) plots measured from X, Y and Z directions are presented in this appendix as supplemental materials for the experimental longitudinal bulk wave and Rayleigh surface wave velocities used in main content in Chapter 5.

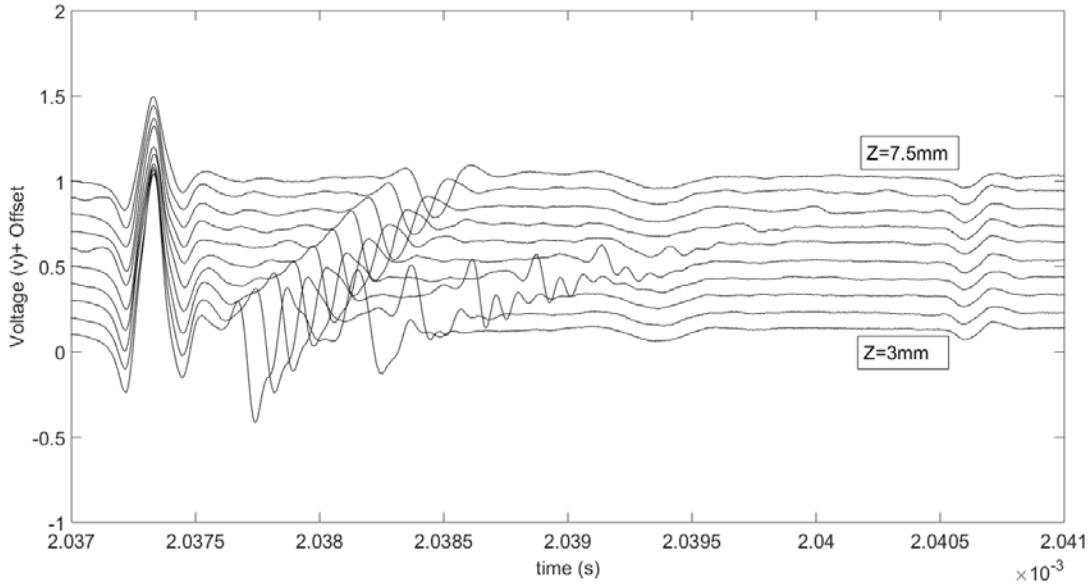

Figure C-7-1 V(z,t) plot from selected z ranges of Rayleigh wave propagating on X direction from Y-cut sample

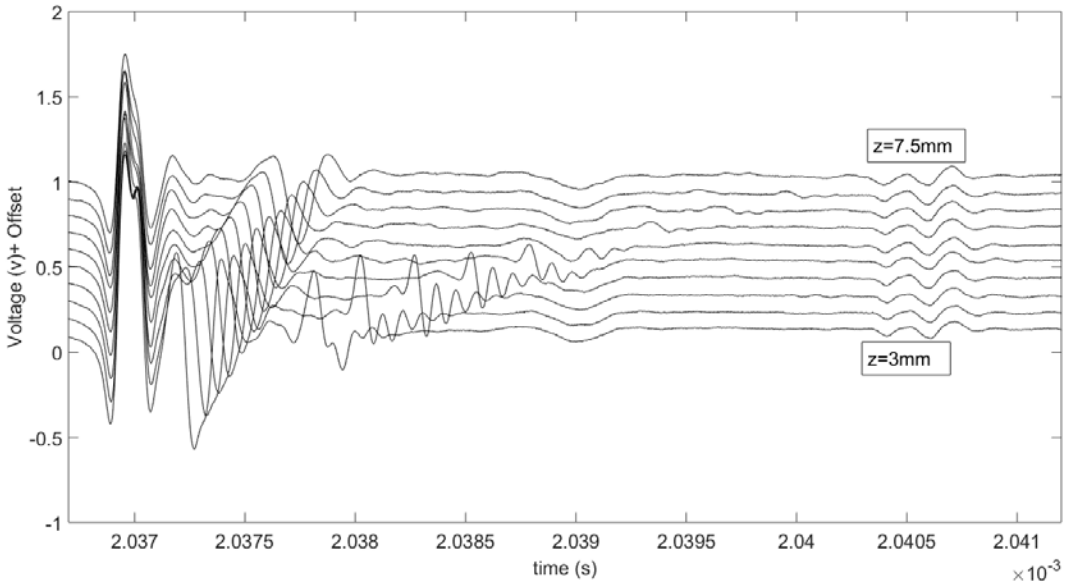

Figure C-7-2 V(z,t) plot from selected z ranges of Rayleigh wave propagating on Y direction from X-cut sample

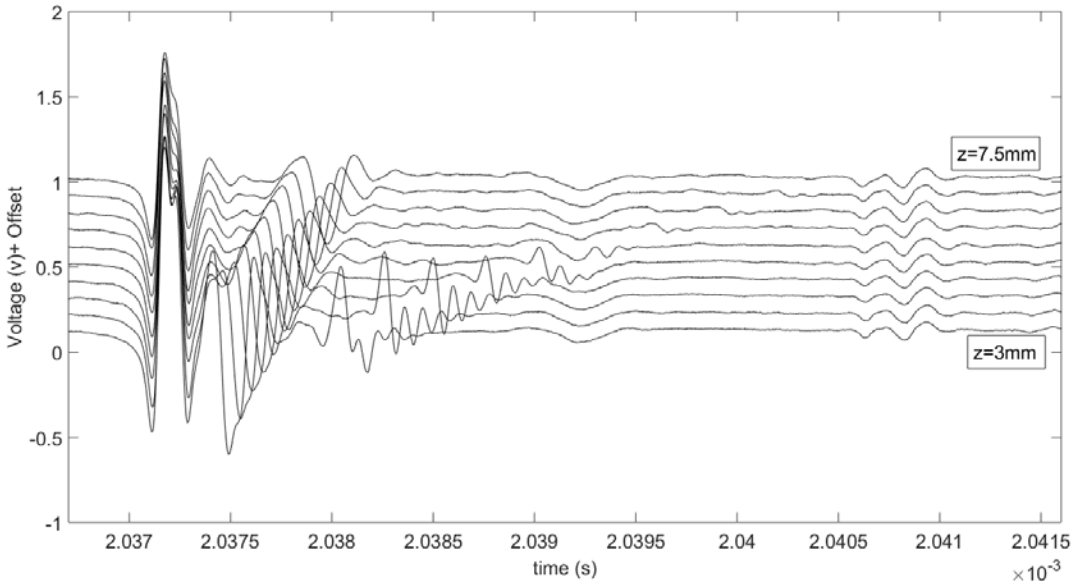

Figure C-7-3 V(z,t) plot from selected z ranges of Rayleigh wave propagating on Z direction from X-cut sample

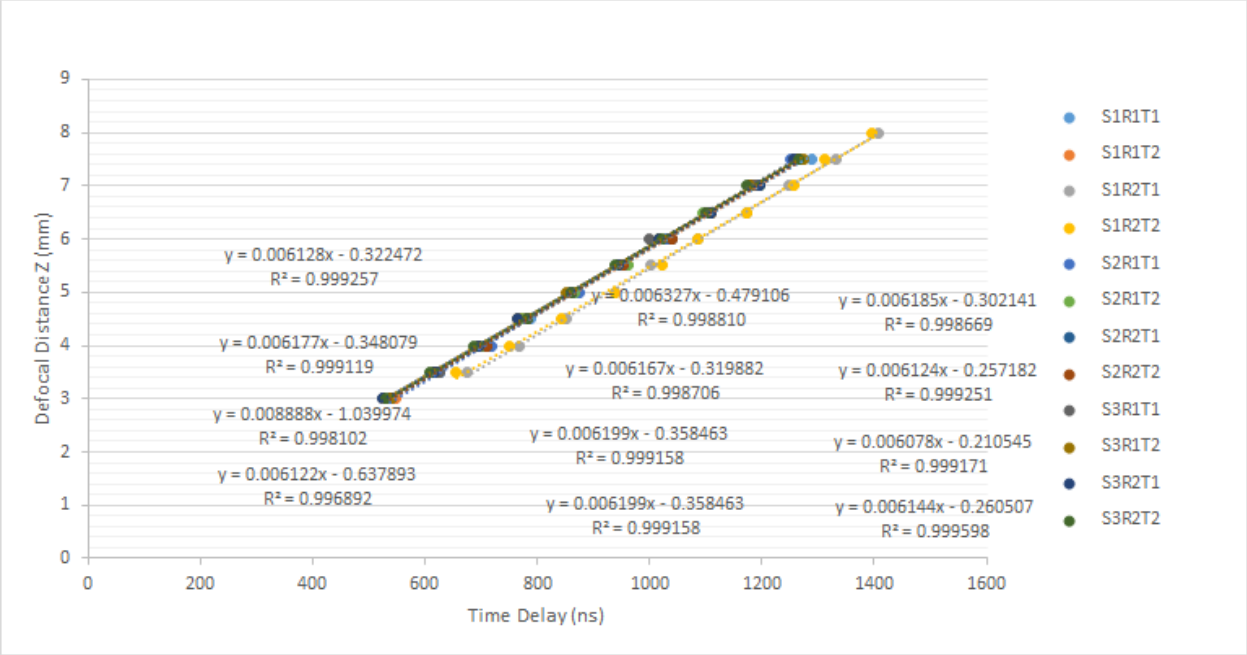

Figure C-7-4 Z(t) plots of X direction Rayleigh waves measured from Y-cut sample

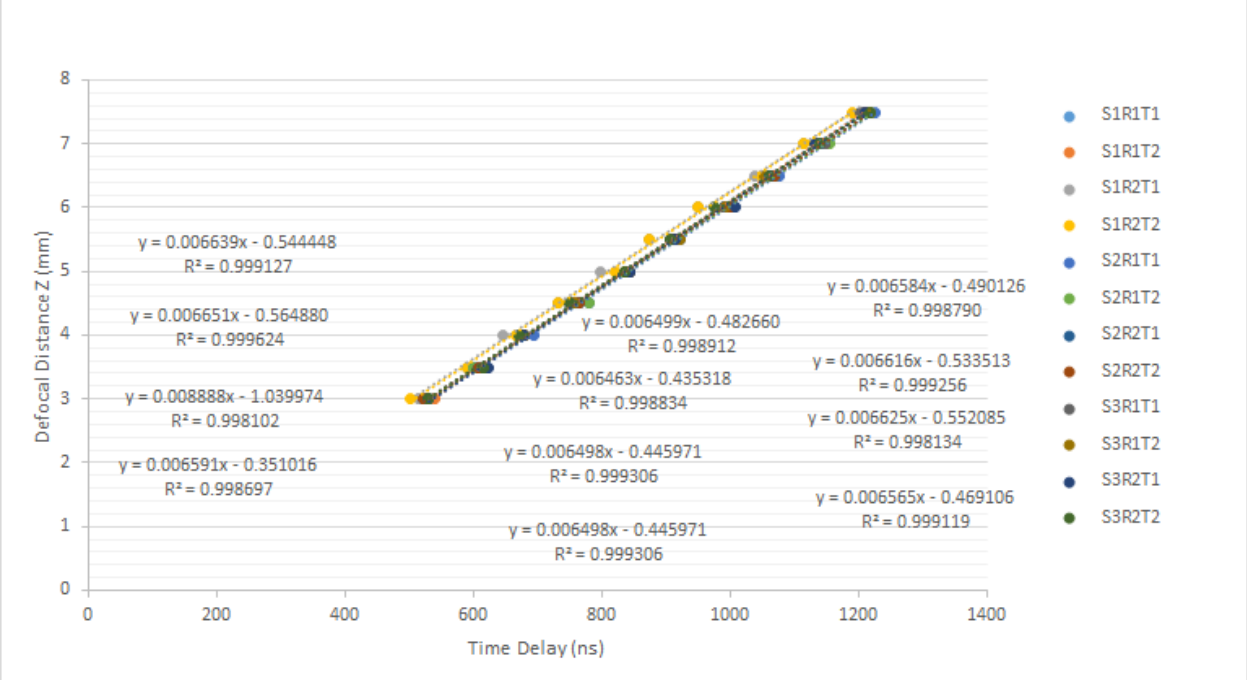

Figure C-7-5 Z(t) plots of Y direction Rayleigh waves measured from X-cut sample

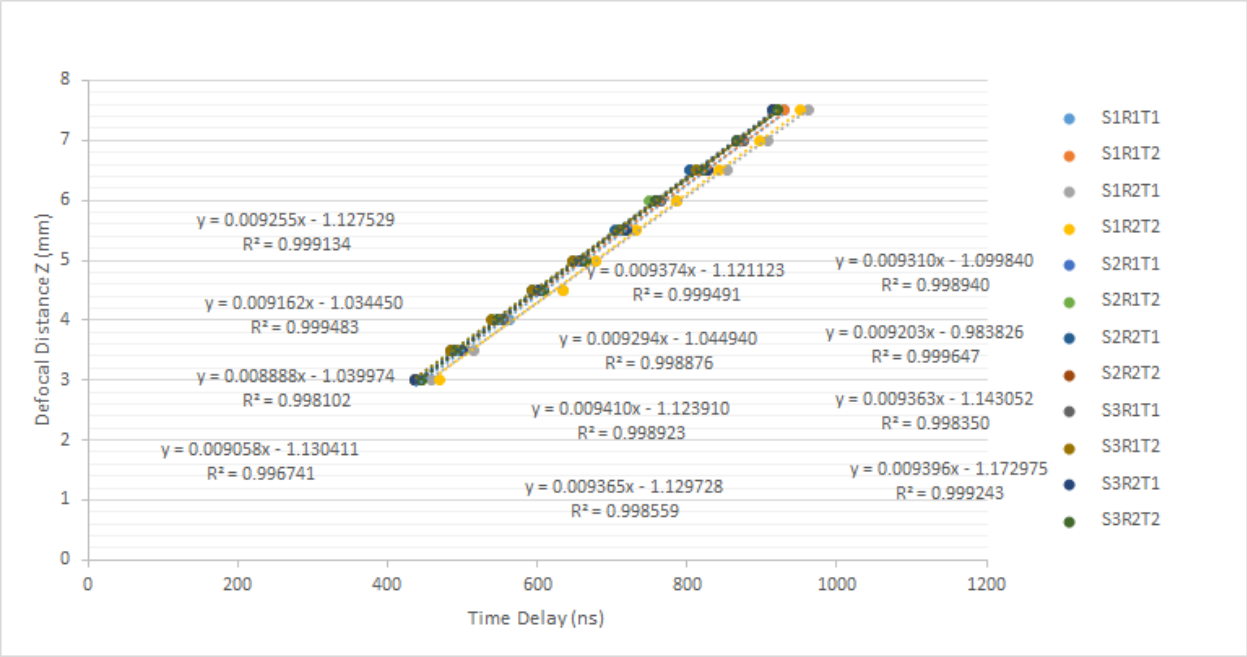

Figure C-7-6 Z(t) plots of Z direction Rayleigh waves measured from X-cut sample

Bibliography

[1] D. Royer and E. Dieulesaint, "Elastic Waves in Solids, Free and Guided Propagation, vol. 1," ed: Springer-Verlag, 2000.

[2] R. Bechmann, "Elastic and Piezoelectric Constants of Alpha-Quartz," *Physical Review,* vol. 110, no. 5, pp. 1060-1061, 1958. doi:DOI 10.1103/PhysRev.110.1060

[3] J. J. Hall, "Electronic effects in the elastic constants of n-type silicon," *Physical Review,* vol. 161, no. 3, p. 756, 1967. doi:10.1103/PhysRev.161.756

[4] L. Pagnotta, "Recent progress in identification methods for the elastic characterization of materials," *International Journal of mechanics,* vol. 2, no. 4, pp. 129-140, 2008.

[5] *ISO 18437 : Mechanical vibration and shock — Characterization of the dynamic mechanical properties of visco-elastic materials,* 2008.

[6] *ASTM E1876: Standard Test Method for Dynamic Young's Modulus, Shear Modulus, and Poisson's Ratio by Impulse Excitation of Vibration*, 2015.

[7] H. Zu, Q. Lin, H. Wu, Y. Zheng, and Q.-M. Wang, "Characterization of the Dielectric, Piezoelectric, and Elastic Coefficients of Ca 3 TaGa 3 Si 2 O 14 Single Crystals up to 800° C," *IEEE transactions on ultrasonics, ferroelectrics, and frequency control,* vol. 63, no. 5, pp. 764-777, 2016.

[8] R. Hearmon, "The elastic constants of piezoelectric crystals," *British Journal of Applied Physics,* vol. 3, no. 4, p. 120, 1952.

[9] R. Zhang, B. Jiang, and W. Cao, "Elastic, piezoelectric, and dielectric properties of multidomain 0.67 Pb (Mg 1/3 Nb 2/3) O 3–0.33 PbTiO 3 single crystals," *Journal of Applied Physics,* vol. 90, no. 7, pp. 3471-3475, 2001.

[10] T. Mihara and M. Obata, "Elastic constant measurement by using line-focus-beam acoustic microscope," Experimental *Mechanics,* vol. 32, no. 1, pp. 30-33, 1992.

[11] D. Xiang, N. Hsu, and G. Blessing, "Materials characterization by a time-resolved and polarization-sensitive ultrasonic technique," in *Review of Progress in Quantitative Nondestructive Evaluation*: Springer, 1996, pp. 1431-1438. doi:10.1007/978-1-4613-0383-1_187

[12] K. Yamanaka, "Surface Acoustic-Wave Measurements Using an Impulsive Converging Beam," *Journal of Applied Physics,* vol. 54, no. 8, pp. 4323-4329, 1983. doi:10.1063/1.332667

[13] J.-I. Kushibiki and N. Chubachi, "Material characterization by line-focus-beam acoustic microscope," IEEE *transactions on sonics and ultrasonics,* vol. 32, no. 2, pp. 189-212, 1985. doi:10.1109/T-Su.1985.31586

[14] Y. Lu, C. He, G. Song, B. Wu, C.-H. Chung, and Y.-C. Lee, "Fabrication of broadband poly (vinylidene difluoride-trifluroethylene) line-focus ultrasonic transducers for surface acoustic wave measurements of anisotropy of a (100) silicon wafer," *Ultrasonics,* vol. 54, no. 1, pp. 296-304, Jan 2014. doi:10.1016/j.ultras.2013.07.006

[15] C.-H. Chung and Y.-C. Lee, "Fabrication of poly (vinylidene fluoride-trifluoroethylene) ultrasound focusing transducers and measurements of elastic constants of thin plates," *NDT & E International,* vol. 43, no. 2, pp. 96-105, Mar 2010. doi:10.1016/j.ndteint.2009.09.004

[16] J. Kushibiki, H. Takahashi, T. Kobayashi, and N. Chubachi, "Characterization of LiNbO3 crystals by line‐focus‐beam acoustic microscopy," *Applied physics letters,* vol. 58, no. 23, pp. 2622-2624, 1991. doi:10.1063/1.104813

[17] Y.-C. Lee, J. O. Kim, and J. D. Achenbach, "Acoustic microscopy measurement of elastic constants and mass density," *IEEE transactions on ultrasonics, ferroelectrics, and frequency control,* vol. 42, no. 2, pp. 253-264, Mar 1995. doi:10.1109/58.365239

[18] A. H. Nayfeh, "Elastic wave reflection from liquid-anisotropic substrate interfaces," *Wave motion,* vol. 14, no. 1, pp. 55-67, 1991.

[19] J. O. Kim and J. D. Achenbach, "Line focus acoustic microscopy to measure anisotropic acoustic properties of thin films," *Thin Solid Films,* vol. 214, no. 1, pp. 25-34, 1992.

[20] T. Mihara and M. Obata, "Elastic-constant measurement by using line-focus-beam acoustic microscope," Experimental *Mechanics,* vol. 32, no. 1, pp. 30-33, Mar 1992. doi:10.1007/Bf02317981

[21] T.-T. Wu and J.-F. Chai, "Propagation of surface waves in anisotropic solids: theoretical calculation and experiment," *Ultrasonics,* vol. 32, no. 1, pp. 21-29, 1994.

[22] J. W. Strutt, "On waves propagated along the plane surface of an elastic solid," *Proceedings of the London Mathematical Society,* vol. 17, no. 1, p. 4, 1885.

[23] H. Lamb, "On a Peculiarity of the Wave‐System due to the Free Vibrations of a Nucleus in an Extended Medium," *Proceedings of the London Mathematical Society,* vol. 1, no. 1, pp. 208-213, 1900.

[24] G. Farnell, "Properties of elastic surface waves," *Physical acoustics,* vol. 6, pp. 109-166, 1970.

[25] R. D. Weglein and R. G. Wilson, "Characteristic material signatures by acoustic microscopy," *Electronics Letters,* vol. 14, no. 12, pp. 352-354, 1978. doi:10.1049/el:19780238

[26] C. T. Schröder and W. R. Scott Jr, "On the complex conjugate roots of the Rayleigh equation: The leaky surface wave," *The Journal of the Acoustical Society of America,* vol. 110, no. 6, pp. 2867-2877, 2001.

[27] W. P. Mason, *Physical* Acoustics*: Principles and Methods*. Elsevier, 2012.

[28] D. Royer and E. Dieulesaint, "Elastic Waves in Solids I: Free and Guided Propagation, translated by DP Morgan," Springer-*Verlag, New York,* 2000.

[29] F. I. Fedorov, *Theory of elastic waves in crystals*. Springer Science & Business Media, 2013.

[30] Novotest. (2018). *BASICS OF ACOUSTICS: Types of waves & Laws of propagation of acoustic waves* – acoustic *field*. Available: http://novotest.biz/basics-of-acoustics-1-4-types-of-waves-and-laws-of-propagation-of-acoustic-waves-acoustic-field/

[31] L. Rayleigh, "On waves propagated along the plane surface of an elastic solid," *Proceedings of the London Mathematical Society*, vol. 1, no. 1, pp. 4-11, 1885. doi:10.1112/plms/s1-17.1.4

[32] H. Lamb, "On the propagation of tremors over the surface of an elastic solid," *Proceedings of the Royal Society of London,* vol. 72, no. 477-486, pp. 128-130, 1904. doi:10.1098/rspl.1903.0029

[33] D. Xiang, N. Hsu, and G. Blessing, "The design, construction and application of a large aperture lens-less line-focus PVDF transducer," *Ultrasonics,* vol. 34, no. 6, pp. 641-647, Aug 1996. doi:10.1016/0041-624x(96)00058-3

[34] R. Weglein, "A model for predicting acoustic material signatures," *Applied Physics Letters,* vol. 34, no. 3, pp. 179-181, 1979.

[35] EOS, "EOS Aluminium AlSi10Mg Datasheet," 2014, Available: https://cdn0.scrvt.com/eos/public/8837de942d78d3b3/4e099c3a857fdddca4be9d59fbb1cd74/EOS_Aluminium_AlSi10Mg_en.pdf

[36] EOS, "EOS NickelAlloy IN718 Datasheet," 2014, Available: http://ip-saas-eos-cms.s3.amazonaws.com/public/4528b4a1bf688496/ff974161c2057e6df56db5b67f0f5595/EOS_NickelAlloy_IN718_en.pdf

[37] EOS, "EOS Titanium Ti64 Datasheet," 2014, Available: https://cdn.eos.info/a4eeb73865d54434/5926811b3739/Ti-Ti64_9011-0014_9011-0039_M290_Material_data_sheet_11-17_en.pdf

[38] ExOneCompany, "X1 Material Data Stainless Steel 316L " 2014, Available: https://www.exone.com/ExOne/media/Materials-Binders/Data%20Sheets/Metal/PSC_X1_MaterialData_316L_062519.pdf

[39] ExOneCompany, "X1 Material Data AlloyIN625," 2014, Available: http://ip-saas-eos-cms.s3.amazonaws.com/public/d1327facdca0e32a/373a60ec4f5c891b7dbcdf572e37d3b0/EOS_NickelAlloy_IN625_en.pdf

[40] B. A. Auld, *Acoustic fields and* w*aves in solids*. Wiley, 1973.

[41] EngineeringToolBox, "Young's Modulus - Tensile and Yield Strength for common Materials," 2003, Available: https://www.engineeringtoolbox.com/young-modulus-d_417.html

[42] J. Kushibiki, T. Kobayashi, H. Ishiji, and N. Chubachi, "Elastic properties of 5 ‐ mol% MgO doped LiNbO3 crystals measured by line focus beam acoustic microscopy," *Applied physics letters,* vol. 61, no. 18, pp. 2164-2166, 1992. doi:10.1063/1.108282

[43] T. Lim and G. Farnell, "Character of pseudo surface waves on anisotropic crystals," *The Journal of the Acoustical Society of America,* vol. 45, no. 4, pp. 845-851, 1969.

[44] A. C. Akhavan. (2005-2016). Available: http://www.quartzpage.de/gen_struct.html

[45] W. P. Mason and H. Baerwald, "Piezoelectric crystals and their applications to ultrasonics," *Physics Today*, vol. 4, p. 23, 1951.

[46] C. Campbell, *Surface* acoustic *wave devices and their signal processing applications*. Elsevier, 2012.